Monitoring urban resilience using fine-resolution satellite nighttime light imagery: A cross-sectoral analysis of global cities

Nikolaos Tziokas, BSc, MSc

Lancaster Environment Centre, Lancaster University

This thesis is submitted in fulfilment of the regulations for the degree of

Doctor of Philosophy

February 2026

To my family

Abstract

Urban resilience—the capacity of cities and their constituent sectors to absorb, adapt to, and recover from disruptive shocks—has become a central concern for sustainable urban development, particularly in response to the COVID-19 pandemic and the unprecedented lockdown measures implemented worldwide. Despite growing interest, empirical assessment of urban resilience remains challenging due to the complexity of urban systems, the heterogeneity of sectoral responses, and the limited availability of high-frequency, spatially detailed socioeconomic data suitable for global comparative analysis. This PhD thesis advances a satellite-based framework for assessing sector-level urban resilience using time-series nighttime light (NTL) imagery as a proxy for human and economic activity. Although NTL data provide consistent global coverage and high temporal frequency, their application to fine-scale urban analysis is constrained by coarse spatial resolution and blooming effects. To address these limitations, the thesis adapts and extends a hybrid geostatistical downscaling approach—Random Forest Area-to-Point Kriging (RFATPK)—to nighttime light data, explicitly accounting for spatial heterogeneity and the point spread function to enhance spatial detail and mitigate blooming.

Validation against independent high-resolution nighttime imagery demonstrates that the downscaled NTL products outperform conventional coarse-resolution data, yielding on average a 17% improvement in socioeconomic representation and substantially enhanced spatial coherence. The refined NTL data exhibit stronger associations with independent indicators, including Gross National Income and development indices. Building on these advances, the thesis introduces a structured resilience framework for assessing urban resilience based on sector-specific NTL trajectories before, during, and after COVID-19 lockdowns, applied to 98 city–sector combinations across 48 global cities. The contribution of this research is both methodological and conceptual. Methodologically, it introduces a consistent and globally scalable approach for measuring sectoral urban economic resilience using satellite nighttime lights, overcoming key limitations of conventional economic statistics in capturing dynamic, intra-urban recovery processes. Conceptually, it demonstrates that economic essentiality acts as a primary organizing dimension of resilience outcomes: sectors linked to essential provisioning disproportionately exhibit resilient or fully recovered trajectories, whereas non-essential commercial and retail activities experience sustained decline, particularly in European cities. These findings reframe urban resilience as an outcome of economic structure and functional organization, rather than an inherent or uniformly distributed property of cities, with clear implications for urban policy and resilience planning.

Declaration for authorship

This thesis has not been submitted to this or any other university in support of an application for another degree. Except as noted, it is the product of my own effort and does not contain any results of work completed in partnership. My supervisors, Dr. Ce Zhang (University of Bristol) and Professor Peter M. Atkinson (Lancaster University), discussed many of the concepts in this thesis.

The following peer-reviewed journal publications contain excerpts from this thesis that were published as part of the project results for the three-year PhD program (2021–2025).

1) Nikolaos Tziokas, Ce Zhang *, Garyfallos C. Drolias, Peter M. Atkinson *, 2023, Downscaling satellite nighttime lights imagery to support within-city applications using a spatially non-stationary model. *International Journal of Applied Earth Observation and Geoinformation*, 122: 103395. https://doi.org/10.1016/j.jag.2023.103395.
2) Nikolaos Tziokas, Ce Zhang *, Alexandros Tziokas, Qunming Wang, Peter M. Atkinson *, 2024, Downscaling Satellite Nighttime Light Imagery While Addressing the Blooming Effect. *IEEE Journal of Selected Topics in Applied Earth Observations and Remote Sensing*, PP(99):1-18. 10.1109/JSTARS.2024.3429244.
3) Nikolaos Tziokas, Ce Zhang *, Alexandros Tziokas, Peter M. Atkinson *, 2026, Uneven urban resilience across economic sectors drawn from satellite nighttime lights. *Nature Cities* (*under-review*).

As the primary author, I certify that the publications are all my own work. Together with my two supervisors, Dr. Ce Zhang, and Professor Peter M. Atkinson, I developed the concepts. I wrote all of the articles and planned and carried out the experiments. Both supervisors have signed below to approve the submission and publication of these research papers.

Sincerely yours.

Signed:

Ce Zhang –

Peter M. Atkinson –

Acknowledgements

Looking back over the past three years, I have come to realize that pursuing a PhD is a journey full of obstacles, uncertainty, and moments of self-doubt, but also one of substantial learning and personal growth. It took time to find my own way of dealing with these challenges, and I certainly did not do so alone. I am deeply grateful to the many individuals who supported me throughout this journey and made the completion of this PhD possible.

First and foremost, I would like to express my sincere gratitude to my supervisors, Dr. Ce Zhang and Professor Peter M. Atkinson, for their invaluable guidance, constructive criticism, and continuous support from the very beginning of my PhD until its completion. Working with Professor Atkinson and Dr. Zhang over the past years has been an exceptional experience. Their extensive expertise, intellectual rigor, passion for research, and strong work ethic have been a constant source of motivation. Without their patience, encouragement, and clear direction, this PhD would not have been completed. I consider myself extremely fortunate to have had such outstanding mentors. Through your guidance, I developed into an independent researcher capable of producing high-quality journal articles with strong practical relevance. I am particularly grateful for the thoughtful and timely feedback you consistently provided. Collaborating with you has been a true pleasure, and I sincerely hope that our collaboration will continue in the future.

This PhD journey was far from straightforward, and several periods were particularly challenging. One of the most demanding phases was the long path toward my first publication, which took nearly two years—from April 2021 to August 2023—to reach acceptance. This experience required persistence and resilience and taught me the importance of trusting the research process, even when progress feels slow. Another major challenge arose during the work on my third paper, where the scale of the data required me to rethink my analytical approach. To manage large volumes of data efficiently, I learned Bash scripting and developed automated workflows for data processing and analysis. Although demanding, this process significantly strengthened my technical skills and improved my ability to conduct scalable and reproducible research.

I would also like to sincerely thank all co-authors and collaborators who contributed to my research in different ways. Your expertise and insights greatly improved the quality of my work. I am equally grateful to my colleagues and peers for creating a stimulating and supportive academic environment. The discussions, feedback, and shared experiences made this journey both intellectually rewarding and enjoyable.

Lastly, I would like to express my deepest gratitude to my family for their unconditional love, patience, and unwavering support throughout this entire journey. Your belief in me gave me the strength to persevere during difficult moments. This PhD is dedicated to you.

Nikolaos Tziokas

Lancaster, February 2026

List of abbreviations

Machine Learning (ML)
Random Forest (RF)
Area-to-Point Kriging (ATPK)
Random Forest Area-to-Point Kriging (RFAPTK)
Area-to-Point Regression Kriging (ATPRK)
Sustainable Development Goals (SDG)
Human Development Index (HDI)
Geographically Weighted Regression (GWR)
Suomi National Polar-orbiting Partnership (SNPP)
Deep Learning (DL)
Random Forest (RF)
Nighttime Lights (NTL)
Visible Infrared Imaging Radiometer Suite (VIIRS)
Day/Night Band (DNB)
Gross Impact (GI)
Net Impact (NI)
Urban Recovery (UR)
Gross Domestic Product (GDP)
Gross National Income (GNI)
Gross Value Added (GVA)
Night Light Development Index (NLDI)
Point Spread Function (PSF)
Defense Meteorological Satellite Program Operational Linescan System (DMSP-OLS)
Coronavirus disease 2019 (COVID-19)
Land Surface Temperature (LST)
Global Human Settlement (GHS)
Average Global Building Height (AGBH)

126 Ensemble Machine Learning (EML)
127 Root Mean Square Error (RMSE)
128 Mean Square Error (MSE)
129 Correlation Coefficient (CC)
130 Sum of Lights (SOL)
131 Metropolitan Statistical Area (MSA)
132 Los Angeles (LA)
133 OpenStreetMap (OSM)
134 Google Earth Engine (GEE)
135 Seasonal and Trend Decomposition (STL)
136 High-End Computing (HEC)
137 Synthetic Aperture Radar (SAR)
138 Points of Interest (POIs)
139 Viewing Angle (VA)
140 The Enhanced Built-up and Bareness Index (EBBI)
141 The Built-up Area Extraction Index (BAEI)
142 The Built-up Index (BUI)
143 The New Built-up Index (NBI)
144 The Normalized Built-up Area Index (NBAI)
145 The Band Ratio for Built-up Area (BRBA)
146 The Normalized Difference Built-up Index (NDBI)
147 The Modified Built-up Area Index (MBAI)
148 The Dry Built-up Index (DBI)
149 The Green Normalized Difference Vegetation Index (GNDVI)
150 The Normalized Difference Vegetation Index (NDVI)
151 The Enhanced Vegetation Index (EVI)
152 Modified Normalized Difference Water Index (MNDWI)
153 Normalized Difference Concrete Condition Index (NDCCI)

Built-up Land Features Extraction Index (BLFEI)
World Settlement Footprint (WSF)
Global Impervious Surface Area (GISA)
Global Artificial Impervious Area (GAIA)
Human Footprint (HFP)
Land Cover (LC)
Land Use (LU)
Downscaling (DS)
Fine-resolution (FR)
Coarse-resolution (CR)
out-of-bag (OOB)
Copernicus Land Monitoring Service (CLMS)

Table of contents

List of figures

List of tables

Chapter 1 Introduction

1.1 Project Background

Policymakers and urban planners require detailed, real-time insights into urban dynamics to effectively mitigate the impact of disruptive events, such as social shocks, and to track progress towards Sustainable Development Goal 11 (SDG 11) - Sustainable cities and communities (Leal Filho et al., 2024). The COVID-19 pandemic and its unprecedented global lockdowns in 2020 triggered rapid and significant shifts in urban activity, highlighting the need for analytical frameworks that can provide timely, sector-specific insights. As urban disruptions become more frequent and complex, traditional approaches to urban analytics struggle to meet this growing demand. The challenge stems from the historical dependence on conventional data sources, such as census and large-scale surveys, which are often static, time-intensive to collect and prone to inaccuracies with aggregation (Ten et al., 2024). In contrast, the increasing availability of remote sensing technologies - particularly nighttime light (NTL) data - offers a promising alternative. NTL data provides a high-frequency, spatially explicit proxy for human activity and economic output, enabling real-time monitoring of urban resilience. By leveraging NTL data, researchers can monitor dynamic urban processes such as nighttime mobility patterns or critical infrastructure fluctuations, facilitating more responsive strategies for resilience assessment.

1.2 Real-world demands from policymakers and urban planners

Rapid urbanization has transformed cities into highly interconnected centers of economic production, social interaction, and infrastructure provision. While this concentration has driven growth, it has simultaneously increased cities’ exposure to systemic shocks, including natural hazards, economic crises, climate-related extremes, and public health emergencies (Ribeiro and Pena Jardim Gonçalves, 2019). As a result, urban resilience—the capacity of cities and their constituent sectors to absorb disturbances, adapt to changing conditions, and recover while maintaining essential functions—has emerged as a central concern in both academic research and policy practice (Y. Zhang et al., 2024a).

Advancement toward the SDGs relies on timely, spatially disaggregated data that encapsulate intra-urban heterogeneity. However, many countries continue to face substantial data deficits. Official statistics and household surveys are frequently sporadic and coarse-grained (Jean et al., 2016; Watmough et al., 2025); see Section 2.2 for a comprehensive discussion of these deficiencies, which limits their utility for surveilling intra-urban inequalities and sectoral vulnerabilities. These constraints impede the capacity of policymakers to discern early signs of stress, deploy interventions effectively, and assess progress toward resilience-oriented SDG targets.

In acknowledgment of these challenges, the United Nations formally solicited a “Data Revolution for Sustainable Development” in 2014, promoting the synthesis of novel data sources with traditional statistical systems to bridge persistent temporal and spatial data gaps (IEAG, 2014). Subsequent discourse has bolstered this position, contending that progress toward the SDGs necessitates not merely additional data, but fundamentally distinct data ecosystems—ones competent in resolving rapid change, spatial heterogeneity, and cross-sectoral interactions in urban environments (Watmough and Marcinko, 2024). Within this context, Earth Observation (EO) has been increasingly situated as a cornerstone of future SDG monitoring and resilience assessment frameworks and contributes pivotally to achieving the SDGs (Stokes and Seto, 2019; Watmough et al., 2025).

Contemporary studies establish that EO data can substantially boost urban resilience analysis by provisioning fine-resolution information that supplements conventional statistics, particularly in contexts where official data are deficient or lagged (Anderson et al., 2017; Chrysoulakis et al., 2023; Zhao and Yu, 2025). By underpinning the monitoring of land use change, urban expansion, energy systems, and environmental conditions, EO contributes directly to multiple SDGs while facilitating integrated evaluations of urban sustainability and resilience. Importantly, EO data are not perceived as surrogates for official statistics, but rather as synergistic elements that fortify the evidence base for policy-relevant decision-making in rapidly evolving urban systems.

In the emerging “EO + statistics” paradigm, nighttime lights (NTL) are salient indicators for urban activity and can help ameliorate critical information gaps (Chang et al., 2025; Gong et al., 2025; R. Liu et al., 2024; Y. Zhang et al., 2024a). Extracted from satellite observations of anthropogenic illumination, NTL data are highly related to electricity consumption (Lu et al., 2025), economic activity (Wu et al., 2025a), population presence (Lei et al., 2024), infrastructure utilization (Paris and Rienow, 2025) and other variables. Two commonly employed metrics—**NTL extent**, delineating the spatial footprint of illuminated areas, and **NTL intensity**, quantifying radiance magnitude—provide synergistic insights into urban dynamics at multiple spatial scales (Mokhtari et al., 2025). NTL provide uniform temporal coverage and near real-time signals of urban change, rendering them invaluable for tracing disruption and recovery, though they necessitate spatial enhancement for city-level analysis.

VIIRS delivers daily global coverage with superior radiometric fidelity and mitigated saturation, optimizing its applicability for urban monitoring (Stokes and Román, 2022). Rectifying these shortcomings is imperative if EO-derived NTL indicators are to realize their potential within SDG-aligned urban resilience frameworks, driving the methodological emphasis of this thesis on downscaling approaches and accuracy enhancement techniques. To fill these identified data gaps into actionable insights for urban resilience, it is requisite to investigate data sources that are both spatially disaggregated and temporally frequent. Earth Observation, and in particular nighttime light imagery, offers a robust avenue to augment traditional statistics and resolve these deficiencies.

Urban form, connectivity, and functional relationships demonstrate pronounced scale dependency, with both observed patterns and statistical associations fluctuating as spatial resolution changes. Relationships discerned at coarser scales may diminish or invert at finer scales, confounding the transferability and interpretation of indicators across resolutions. Concurrently, contemporary urban change increasingly arises through city- and within-city-scale processes such as renewal, infill, and placemaking, where key determinants of resilience—local service accessibility, small-scale economic activity, and infrastructure performance—operate at spatial grains finer than those captured by most native nighttime lights products. Consequently, the selection of analytical resolution represents a theoretical determination rather than a purely technical one: it must correspond with the spatial scale of the underlying urban processes (Guo et al., 2024). This scale inconsistency between sensors and processes necessitates the deployment of downscaling and morphology-aware aggregation approaches to ensure that NTL-derived indicators encapsulate city-level disruption and recovery in a conceptually valid manner. This scale mismatch instigates the RFATPK downscaling approach developed in Section 1.4, which aims to increase sensor spatial resolution with within-city level resilience analysis.

1.3 Broad context and academic requirements

While Section 1.2 established the policy and planning demand for improved urban resilience monitoring, this section focuses on the technical suitability of Earth Observation (EO) data for resilience estimation. Effective resilience analysis requires temporally frequent, spatially explicit, and comparable data to detect abrupt disruptions and gradual recovery processes (Kapucu et al., 2024). Many conventional socio-economic datasets fail to meet these requirements due to reporting delays, inconsistent methodologies, and spatial aggregation, particularly at sub-city scales.

Satellite-based observations are acquired using standardized sensor specifications and data reduction workflows, facilitating cross-city and cross-national comparison that is rarely feasible with administrative or survey-based data (Y. Zhang et al., 2024a). Moreover, EO data are intrinsically geospatial, permitting resilience to be scrutinized as a geographically heterogeneous phenomenon rather than as an aggregate urban outcome. These attributes render EO particularly advantageous for characterizing urban systems in which vulnerability, upheaval, and recuperation are asymmetrically dispersed across cities and sectors.

A broad spectrum of EO-derived indicators has been leveraged for resilience-related research. Optical and radar imagery have been deployed to quantify physical damage to infrastructure (Kopiika et al., 2025) and to map flood extent (Popandopulo et al., 2023). Thermal data underpin investigations of urban heat exposure and energy demand (Du et al., 2025), while multispectral indices record vegetation loss or recovery in the wake of shocks (H. Xu et al., 2024).

Night-time lights (NTL) data present a synergistic advantage by explicitly recording changes in anthropogenic activity. Because artificial illumination is intimately correlated with electricity consumption, commercial operations, and population presence (Nighttime light remote sensing for urban applications), NTL observations respond rapidly to disturbances that impair urban functionality (Qiang et al., 2020). Contractions in NTL intensity have been registered following earthquakes (Gong et al., 2025), conflicts (Li et al., 2013), and extreme weather events (Hu et al., 2024), while subsequent amplifications have been used to delineate the pace and spatial disparity of rebound (Ma et al., 2023; Qiang et al., 2020; Wu et al., 2025a).

Applied applications of NTL in resilience research primarily add value by facilitating the decomposition of shock response and restoration processes within cities; instead of conceptualizing urban resilience as a single outcome, these studies exploit spatial variance in NTL signals to examine how distinct components (e.g., economic sectors or population) of the urban system behave over time, establishing a foundation for diagnosing uneven recovery dynamics across functional zones (Huang et al., 2024). In this way, NTL augments other EO-derived indicators by underpinning evaluations of socio-economic vitality at spatial and temporal scales that are challenging to obtain with conventional datasets.

Frequently utilized sources include DMSP-OLS, NPP-VIIRS DNB, EROS-B, Luojia-1, and Jilin-series sensors; however, no single sensor currently yields both the fine spatial and high temporal resolution optimal for resolving intra-city-level human dynamics (Liu et al., 2022; W. Xu et al., 2024). Limitations on satellite deployment and sensor design therefore necessitate methodological approaches that fuse multiple data sources and implement spatial refinement to harmonize NTL with the scales at which urban processes operate. Additionally, sensor-related effects such as saturation and blooming can skew radiance values in densely lit urban cores (Wu et al., 2021; Zheng et al., 2020), introducing ambiguity into resilience estimates based on raw NTL data.

Mitigating these deficiencies is imperative if NTL data are to be used as robust inputs for granular urban resilience analysis. Accordingly, this thesis concentrates on enhancing the spatial fidelity and accuracy of NTL imagery through downscaling techniques and rectification for sensor artefacts. These technical progressions constitute the groundwork for the empirical analysis presented in Chapters 3 and 4 and enable the application of refined NTL indicators to urban resilience quantification in Chapter 5.

1.4 Research Objectives and Key Concepts

1.4.1 Motivation: From City-Level to Sector-Level Urban Resilience

Urban resilience is progressively conceptualized as a multifaceted and spatially non-uniform phenomenon (Datola, 2023; Gu et al., 2025; Kapucu et al., 2024), mirroring the uneven distribution of exposure, susceptibility, and adaptive potential within cities. While numerous existing resilience evaluations function at the county or country level, such methodologies threaten to mask critical intra-urban disparities in how perturbations are absorbed and how restoration evolves across discrete urban domains.

Urban agglomerations consist of functionally discrete precincts (e.g., commercial, industrial, retail) that often manifest divergent reactions to the identical stressor. Observational data from contemporary emergencies, including the COVID-19 pandemic, substantiates that these segments often demonstrate bifurcated disruption and rebound trajectories, underpinned by variances workforce density (Lu and Zhang, 2025), and policy susceptibility (Dascher-Preising and Greiner, 2023). City-level resilience indices consequently yield constrained visibility into these segment-particular mechanics.

A disaggregated sectoral perspective facilitates a more sophisticated comprehension of urban resilience by decomposing urban responses geographically and functionally. This approach underpins the detection of uneven restoration patterns within cities and permits resilience to be evaluated not merely as a cumulative result, but as a dynamic that fluctuates across urban components. Such resolution is especially pivotal for guiding precision policy measures aimed at bolstering the most impacted constituents of the urban system.

1.4.2 NTL Data and Its Analytical Challenges

While nighttime light data yield unique temporal responsiveness to urban shocks and recovery, their direct employment in sector-level resilience analysis remains analytically hampered due to problems elucidated in subchapter 1.3—namely, coarse spatial resolution and the blooming effect. Accordingly, methodological advances is requisite to reconcile NTL data with the spatial and sectoral demands of resilience quantification. This thesis addresses that imperative by formulating and deploying techniques that increase the spatial resolution of NTL imagery. The ensuing analytical framework facilitates the sector-level resilience evaluation performed in Chapters 3–5.

1.4.3 Advanced Downscaling with RFATPK

This thesis applies Random Forest Area-to-Point Kriging (RFATPK), a hybrid approach that combines Random Forest prediction with area-to-point Kriging to enhance NTL spatial detail and reduce blooming artefacts. The method does not "correct" the data in the traditional sense but enhances spatial detail and interpretability, producing finer-resolution NTL surfaces suitable for sector-level applications. By generating these high-resolution representations of urban lighting patterns, RFATPK allows for more precise quantification of resilience and enables meaningful comparison across sectors.

1.4.4 Research Objectives and Questions

The overarching aim of this PhD thesis is to assess **sector-level urban resilience** to COVID-19 lockdowns using fine-resolution NTL imagery, providing actionable insights for urban planning and policy. The study is structured around three specific objectives and corresponding research questions:

1. **Adapt and apply RFATPK to downscale NTL imagery**
   Research Question 1: *Can a geostatistical downscaling method originally developed for daytime imagery be effectively applied to NTL while maintaining spatial accuracy and reliability?*

2. **Mitigate the blooming effect in NTL imagery during downscaling**
   Research Question 2: *Can RFATPK be optimized to reduce the blooming effect in NTL, improving its suitability for socioeconomic and resilience analysis?*

3. **Leverage fine-resolution NTL to evaluate sector-level urban resilience under a global shock**
   Research Question 3: *Why do some economic sectors continue to prosper while others decline in response to disruptive events?*

1.5 Thesis structure

Papers that have already been published or are in the process of being published constitute this paper-based thesis (Chapters 3 - 5):

Chapter 1: Introduction
This chapter introduces the thesis, outlining the practical need for urban resilience monitoring by

policymakers and urban planners. It emphasizes both the benefits and limitations of using nighttime light (NTL)-based assessments.

Chapter 2: Literature Review
This chapter reviews traditional methods for assessing urban resilience and the application of satellite-derived NTL data in urban studies. It discusses the limitations of existing approaches and identifies future research directions, particularly for global-scale, sector-level analysis.

Chapter 3: Downscaling Nighttime Light Data Using a Geostatistical Approach
This chapter presents a geostatistical solution for downscaling NTL imagery. It demonstrates the superiority of the proposed method over existing techniques and establishes that the downscaled NTL data serve as a more accurate proxy for socioeconomic phenomena.

Chapter 4: Mitigating the Blooming Effect in Downscaled Nighttime Light Data
This chapter extends the geostatistical approach by focusing on reducing the blooming effect in NTL imagery. The results show that mitigating the blooming effect significantly increases prediction accuracy, making fine-resolution NTL data a more reliable proxy for socioeconomic activities.

Chapter 5: Assessing Urban Resilience Using Fine-Resolution Nighttime Light Data
This chapter applies the fine-resolution NTL data produced through the previous two chapters to assess urban resilience at the sector level across multiple global cities, providing insights into resilience patterns and sectoral differences.

Chapter 6: Discussions and Conclusions
The final chapter synthesizes key findings from Chapters 3–5, answers the research questions posed in Chapter 1, and reflects on the broader implications of the study. It concludes with recommendations for future research and policy applications.

Chapter 2 Literature review

As hubs of social and economic activity, cities are highly susceptible to unexpected shocks that can disrupt the lives of people. These disruptions, whether triggered by natural disasters, financial crises or pandemics, are often amplified by excessive resource consumption, inadequate infrastructure, poor urban planning and inefficient public services (Kapucu et al., 2024). While no city is immune to these challenges, strengthening urban resilience is essential for mitigating risks and ensuring sustainable urban development (Sajjad et al., 2021).

In recent years, there has been growing recognition of the need for comprehensive urban resilience assessments, particularly in response to the disruptions caused by the COVID-19 pandemic. As a result, both academic research and policy initiatives have increasingly focused on developing effective resilience evaluation strategies (Büyüközkan et al., 2022; Chen and Chen, 2025; Datola, 2023). However, the concept of urban resilience has been inconsistently defined and interpreted across literature, making it hard to translate theoretical frameworks into actionable insights. Scholars argue that most pandemic-related studies remain largely theoretical, with limited empirical investigation, due in part to the multifaceted nature of resilience, which encompasses diverse dimensions such as urban planning, supply chain management, the economic impact of disasters (Ribeiro and Gonçalves, 2019). A major limitation of existing research is the lack of a comprehensive metric capable of capturing the dynamic and sector-specific nature of urban resilience. Current approaches often rely on coarse spatial and temporal resolution data, making it difficult to assess resilience at the sectoral-level, and at even more granular levels. To address these gaps, there is an urgent need for fine-resolution data that can capture socioeconomic activity across different urban sectors, enabling more accurate and sector-specific resilience assessments.

2.1 Traditional measures of urban resilience

In contemporary urban discourse, urban resilience (refer to the working definition of urban resilience in Section 1.2) has emerged as a pivotal analytical concept for deciphering how cities and regions react to, withstand, and recuperate from shocks such as economic crises, natural disasters, and public health emergencies. Consequently, a substantial empirical literature has coalesced around the quantification of urban resilience, precipitating a diverse array of conceptual frameworks and quantitative indicators (Ma et al., 2022; Sharifi, 2019; Y. Zhang et al., 2024b).

Traditional empirical methodologies for assessing urban resilience rely predominantly on socioeconomic, demographic, institutional, and infrastructure-related metrics, typically extracted from official statistics, administrative records, and surveys (Y. Zhang et al., 2024b). In many studies, resilience is operationalized through composite indices that synthesize multiple variables intended to encapsulate exposure, susceptibility, adaptive capacity, and recuperation potential. For example, in a global evaluation of COVID-19 impacts, vulnerability and resilience indices were formulated using indicators drawn from the World Development Indicators, World Governance Indicators, and United Nations Development Programme datasets, including measures of income, health competency, governance caliber, and demographic composition (Diop et al., 2021). These composite indices were then utilized to categorize nations into vulnerability–resilience taxonomies, offering a comparative depiction of economic resilience across regions during the pandemic.

At sub-national and regional scales, traditional resilience assessments frequently prioritize economic composition and labor market performance. Studies of regional economic resilience often quantify robustness through fluctuations in employment, income per capita, unemployment rates, population dynamics, and migration motifs before and after economic shocks. For instance, analysis of non-metropolitan regions in Slovakia operationalized economic resilience using a Regional Development Index integrating demographic ageing, net migration, income per capita, and registered unemployment. Spatial regression models were then deployed to scrutinize how industrial diversity, sectoral makeup, firm size topology, and geographic accessibility modulated post-crisis restoration pathways (Ženka et al., 2021). This approach reflects a broader thematic strand of literature in which resilience is inferred from the capacity of local or regional economies to withstand contractions and re-establish growth following macroeconomic disruptions.

Another prominent corpus of work centers on business recuperation and firm-level responses to extreme events. Following major disasters, resilience is often quantified through establishment reopening rates, business longevity, and spatial motifs of economic reactivation. In the wake of Hurricane Katrina, for example, business resilience in New Orleans was assessed using longitudinal data on establishment reopening decisions compiled through repeated telephone and street surveys. Spatial econometric models were applied to capture interdependence between neighboring firms, elucidating how local clustering effects shape restoration dynamics (LeSage et al., 2011). Such studies conceptualize resilience primarily as the velocity and magnitude of economic reanimation within impacted urban areas.

Beyond economic indicators, traditional resilience research has also integrated social and health-related dimensions, particularly in the context of public health shocks. Survey-based studies have been extensively utilized to assess how urban populations cope with and adapt to crises. During the COVID-19 pandemic, cross-sectional telephone surveys were employed in Bangkok to examine the correlation between urban green space utilization and mental health well-being. Using standardized well-being metrics (e.g., WHO-5 scores) alongside socioeconomic and behavioral variables, these studies captured individual-level resilience outcomes related to psychological well-being, highlighting the role of urban amenities in mitigating crisis impacts (Arifwidodo and Chandrasiri, 2023).

In parallel, qualitative and mixed-methods approaches have contributed to traditional resilience quantification by documenting practitioner perspectives and institutional reactions. Interview-based studies in Sub-Saharan African cities have explored how resilience is perceived and operationalized by urban planners and infrastructure managers (Amegavi et al., 2024). These studies often reveal a dominant focus on functional and outcome-oriented measures of resilience, particularly pertaining to physical infrastructure performance and service continuity. Similarly, post-disaster assessments of water infrastructure resilience following the 2021 Texas winter storm relied on semi-structured interviews with utility operators to evaluate resilience across economic, governance, infrastructure, environmental, and social dimensions over sequential restoration phases (Tiedmann et al., 2023).

Collectively, this literature substantiates that traditional measures of urban resilience are grounded in observable socioeconomic outcomes, institutional attributes, infrastructure performance, and survey-based indicators, often analyzed through composite indices, regression models, and longitudinal comparisons. These approaches have been instrumental in advancing empirical understanding of how cities and regions respond to shocks and recuperate over time.

2.2 Issues with the traditional assessments of urban resilience

Traditional approaches to measuring urban resilience face persistent and well-documented limitations related to data cost, temporal frequency, coverage, institutional capacity, and methodological consistency, which collectively undermine the robustness, comparability, and policy relevance of resilience assessments (Xu and Qiang, 2021). A fundamental constraint is the financial and logistical burden of core data sources, such as population censuses and large-scale household surveys, which are conducted infrequently—typically on decennial or quinquennial cycles (Jerven, 2017; Watmough et al., 2025). Consequently, resilience analysis based on these datasets rely on static or outdated baselines, limiting their ability to capture the timing, magnitude, and recovery dynamics of shocks, particularly in rapidly evolving urban crisis contexts.

Coverage gaps further compromise traditional resilience metrics. In many low- and middle-income countries, statistical systems lack comprehensive sub-national and intra-urban data, while household surveys frequently exclude marginalized groups such as informal settlers and migrant populations, despite their heightened vulnerability to shocks (Jerven, 2017). Incomplete vital registration systems similarly constrain access to reliable health and mortality data during crises, introducing systematic biases that obscure spatial inequalities and underestimate localized vulnerability.

These challenges are intensified by institutional and capacity constraints within national statistical offices. Chronic underinvestment has resulted in fragmented datasets, inconsistent methodologies, and weak quality control, particularly in resource-constrained settings (Jerven, 2017, 2013). Expanding data demands associated with global policy frameworks, such as the Sustainable Development Goals, have further strained statistical systems, sometimes prioritizing indicator availability over analytical reliability, thereby weakening their utility for urban resilience analysis.

Methodological inconsistencies and limited transparency in administrative and economic statistics further impede longitudinal and cross-country comparisons. Variations in accounting practices, sectoral classifications, and price adjustments—along with frequent rebasing of national accounts—introduce structural breaks that complicate the interpretation of recovery and growth trajectories (Jerven, 2013). Political and behavioral incentives may also distort reported outcomes when funding, legitimacy, or performance evaluation is linked to administrative data, reducing their reliability during crisis periods (Jean et al., 2016).

While qualitative and survey-based methods provide valuable insights into social and institutional dimensions of resilience, they are costly, time-intensive, difficult to scale, and often infeasible during disasters, limiting their usefulness for continuous monitoring (Zhang et al., 2024b). Moreover, the typically coarse spatial resolution of traditional datasets masks intra-urban heterogeneity, despite cities exhibiting pronounced variation in exposure, vulnerability, and recovery capacity across neighborhoods and sectors (Watmough et al., 2025).

Collectively, these limitations have motivated increasing interest in alternative data sources capable of providing high-frequency, spatially explicit insights into urban dynamics. Remotely sensed nighttime light (NTL) imagery has emerged as a particularly promising Earth Observation–derived approach for monitoring short-term disruption, recovery, and sector-specific resilience at fine spatial scales (Xu and Qiang, 2021). Unlike EO-for-poverty approaches that emphasize long-term socioeconomic conditions, NTL is well suited to capturing transient, sector-specific urban functional changes, making it a valuable tool for operationalizing urban resilience analysis.

2.3 An overview of satellite nighttime lights in urban studies and alternative EO-based socioeconomic approaches

In recent decades, remotely sensed nighttime light (NTL) imagery has attained global stature as a mechanism for recording motifs of anthropogenic illumination that are intimately linked with human presence, economic vitality, and infrastructure utilization (Elvidge et al., 1997; Stokes et al., 2021). Due to its pronounced correlations with socioeconomic metrics and its capacity to resolve intra-urban fluctuations in activity levels, NTL has been extensively employed to spatialize variables such as population distribution, economic productivity, and energy utilization (Li et al., 2016).

Since the initial digital archiving of NTL data through the Defense Meteorological Satellite Program’s Operational Linescan System (DMSP-OLS) in 1992 (Elvidge et al., 1997), and more recently through the VIIRS Day/Night Band (DNB), the utility of NTL imagery in urban studies has augmented significantly. Over the past three decades, NTL data have been leveraged to delineate urbanization processes (Kyba et al., 2017), quantify socioeconomic parameters such as GDP and electricity consumption (Chen and Nordhaus, 2011), evaluate environmental externalities including CO_2 emissions (Li et al., 2015), and capture temporal shifts in human activity linked with disasters, armed conflict, and holidays (Li et al., 2013; Román and Stokes, 2015). More recently, NTL imagery has been increasingly deployed to monitor perturbations in urban systems during exogenous shocks, including the COVID-19 pandemic, underscoring its sensitivity to ephemeral changes in economic and social activity.

Despite its growing prominence, NTL is not the exclusive Earth Observation (EO) data source that has been utilized to infer socioeconomic conditions. In parallel, a rapidly proliferating body of literature has centered on the use of EO data to estimate poverty and deprivation, an emerging domain often designated as “EO for poverty” (Watmough et al., 2019; Watmough and Marcinko, 2021). This research trajectory has gained substantial momentum due to persistent gaps in the availability, frequency, and spatial fidelity of traditional poverty data derived from household surveys and censuses, particularly in low- and middle-income nations. EO-based poverty studies commonly synthesize daytime optical imagery, land cover data, infrastructure proxies, vegetation indices, and, in some instances, NTL, utilizing statistical and machine learning models to predict poverty indicators or asset-based wealth indices (Chi et al., 2022; Jean et al., 2016; Steele et al., 2017).

The pertinence of EO-for-poverty methodologies to urban resilience analysis is evident. Poverty and deprivation are intricately coupled with susceptibility, adaptive capacity, and long-term restoration potential, and shocks such as the COVID-19 pandemic have been demonstrated to negate decades of progress in poverty alleviation (Egger et al., 2021; Yonzan et al., 2022). Watmough and Marcinko (2025) emphasize that EO data can play a vital role in enhancing the temporal frequency and spatial granularity of socioeconomic information, thereby supporting policy reactions to rapidly evolving shocks.

However, while EO-for-poverty approaches are highly significant for comprehending long-term socioeconomic conditions, they are not optimally configured for the specific mandates of this thesis. As elucidated by Watmough and Marcinko (2021), poverty is a multidimensional and context-dependent phenomenon that cannot be resolved using EO data exclusively, and many EO-based poverty models rely on cross-sectional survey data, complex feature engineering, or generalized machine-learning frameworks that are not calibrated for high-frequency temporal monitoring. These approaches are typically better aligned with quantifying structural or stock-based facets of deprivation rather than resolving acute perturbations, rapid contractions in activity, or recovery trajectories following sudden shocks. Moreover, EO-for-poverty models often require voluminous ground-truth data and local contextual information, circumscribing their utility for consistent, global, near-real-time analysis across diverse urban centers.

In contrast, NTL imagery presents a distinctive advantage for resilience analysis in urban settings by provisioning consistent global coverage, high temporal frequency, and direct responsiveness to fluctuations in human and economic activity. The VIIRS-DNB sensor, for example, captures nighttime brightness emissions from commercial zones, residential lighting, streetlights, and vehicular traffic, enabling the detection of abrupt shifts associated with lockdowns, mobility constraints, and incremental reopenings (Stokes and Román, 2022). These attributes render NTL particularly suitable for monitoring shock response and restoration dynamics, which are central to the operationalization of urban resilience formulated in this dissertation.

Nonetheless, the application of NTL data is not without constraints. As previously articulated in sub-chapter 1.3, a pivotal challenge is the blooming or overglow effect, a radiometric artifact whereby light from intense sources disperses into contiguous pixels, exaggerating illuminated extents and masking local spatial variability. This distortion impedes the use of native-resolution NTL data for fine-scale urban and sector-level analysis. Rectifying this limitation necessitates methodological progressions capable of enhancing spatial detail while preserving the underlying signature of human activity.

For these reasons, this thesis adopts nighttime light imagery as its primary EO data source, supplemented by advanced spatial downscaling techniques, to assess sector-specific urban resilience to COVID-19 lockdown policies. This selection reflects a deliberate methodological determination informed by the broader EO-for-poverty literature, rather than a pre-established preference. While EO-based poverty mapping provides critical insights into long-term vulnerability and development outcomes, NTL data—when rigorously processed—offer a more robust proxy for resolving the temporal dynamics, sectoral heterogeneity, and spatial granularity requisite to analyze urban resilience in the context of an acute global shock.

2.4 NTL-based assessment of urban resilience

An extensive body of research has been devoted to investigating the role of NTL in the urban resilience of natural and social shocks, with numerous studies utilizing NTL as a proxy to examine responses to weather-related extreme events. For example, Mård et al. (2018) used annual NTL data to quantify changes in human settlement patterns in response to flood events, reporting a correlation coefficient of 0.69 between increases in settlement distance from rivers and normalized flood fatalities, and 0.39 with economic flood losses, demonstrating the quantitative sensitivity of NTL to socio-environmental resilience processes. Similarly, Qiang et al. (2020) applied inter-calibrated DMSP-OLS NTL data to estimate GDP across 179 counties affected by Hurricane Katrina. They reported a strong linear relationship between NTL-derived metrics and GDP ($R^2 = 0.92$), although multivariate regression of resilience metrics (instant disturbance, recovery rate, and accumulated loss) explained only a modest proportion of the variance (adjusted $R^2 \sim 0.27$–0.40), highlighting both the utility and the limitations of NTL as a proxy for economic resilience. Xu and Qiang (2021) applied moonlight-adjusted SNPP-VIIRS daily imagery to Hurricane Sandy (2012), measuring NTL disturbance and recovery across 66 Core-Based Statistical Areas, and observed a V-shaped recovery pattern in 82.1% of regions; 56.4% fully recovered or exceeded pre-disaster radiance levels, while 25.6% did not recover by the end of the observation period. Regression results further revealed statistically significant relationships between NTL changes and wind speed, distance to the hurricane track, and social media activity, indicating that NTL captures both physical damage and human response dynamics. Jia et al., (2023) demonstrated the utility of NTL for quantifying disaster impact and recovery following Hurricane Maria (2017) in Puerto Rico. Using angularly normalized VIIRS daily NTL data, they reported a Pearson correlation of 0.929 between NTL radiance and power supply. Across eight regions, average power outages reached 78.01%, with the most severely affected regions experiencing losses exceeding 88%, and recovery trajectories varying substantially across space. The authors further showed that NTL-derived indicators could be used to estimate GDP losses in the service and industrial sectors, highlighting the dual infrastructural and economic relevance of NTL. In China's North–South Seismic Belt, Liu et al. (2024) applied NTL data to validate a multidimensional urban resilience assessment framework encompassing social, economic, infrastructural, and ecological dimensions. They reported that the mean urban resilience index increased by ~115% in 2021, accompanied by a reduction in regional disparity (coefficient of variation from 0.823 to 0.751) and an increase in spatial autocorrelation (Moran's I from 0.2017 to 0.4476). Temporal shifts in the total nighttime light index during historical earthquake events were consistent with calculated resilience trajectories, supporting the validity of NTL as an indirect resilience indicator. Assessed resilience to floods has been studied by Zhang et al. (2022), who analyzed 42 subdistricts in Jakarta by integrating Sentinel-1A SAR imagery with NTL-derived GDP indicators. Their regression analysis showed that elevation ($\beta = 0.3784$) and slope ($\beta = 0.1079$) positively influenced recovery, whereas population density ($\beta = -0.1774$) exerted a negative effect, illustrating how NTL complements high-resolution remote sensing data in explaining spatial variability in urban flood resilience. Apart from the extensive research that has been done to measure urban resilience to natural disasters, researchers utilized nighttime lights satellite sensor data for monitoring resilience to social shocks.

The NTL dataset has been employed to assess various dimensions of social shocks. Roshan et al. (2024) utilized NTL to highlight the effectiveness of NTL during the Ukrainian war to inform future urban planning and resilience strategies in conflict zones, observing a 27.2% reduction in nighttime light intensity across major affected cities, consistent with declines in socio-economic activity. Du et al. (2023), demonstrated that improvements in digital inclusive finance can enhance economic resilience; for this purpose, they utilized NTL alongside other socioeconomic variables and developed an empirical model that explained more than 60% of regional economic resilience variability. Rowe et al. (2022) examined NTL dynamics during the COVID-19 pandemic across 42 countries, showing that government policy stringency exerted a large and statistically significant influence on NTL reductions (β ~ 4.0–4.7, $p < 0.001$), with marginal R^2 values up to 0.6 and conditional R^2 values up to 0.980, indicating substantial explanatory power. Recently, a global pandemic (COVID-19) shocked the world and lockdown measures were implemented almost in every country.

2.5 NTL-based assessment of urban resilience to COVID-19 lockdowns

It is becoming increasingly evident that outbreaks of diseases, as well as other long-lasting disasters, are occurring with higher frequency in densely populated areas and interconnected cities (Elmqvist et al., 2019; Menoni et al., 2024), with the 2020s global COVID-19 pandemic being one such event. Considerable research has been undertaken using NTL illumination to evaluate the repercussions of pandemic lockdowns. Studies have looked at city-scale lockdowns and activity changes to monitor NTL dynamics through time, as evidenced by analyzes of Middle Eastern metropolitan areas and worldwide (Stokes and Román, 2022; Xu et al., 2021). These studies focused mainly on the immediate impact of the lockdowns at the city level. While few studies have performed subnational-level research (Y. Liu et al., 2023), country-scale evaluations, such as those conducted in mainland US, have examined larger effects and the connection between NTL and economic metrics like GDP (Lin and Rybnikova, 2023).

NTL data have been used to assess lockdown impacts and economic resilience in regional studies, including those carried out in the province of Hubei and the Xinjiang area (Jiang and Liu, 2024; Z. Wang et al., 2024) with an emphasis on dynamic evaluation of the lockdown period. These coarse level analyzes, while offering insights into the impacts of the lockdown on countries and cities, fail to capture intra-urban variations. Furthermore, pixel-scale analysis has been conducted to provide a thorough grasp of urban resilience and particularly recovery trends (Ma et al., 2023). The aforementioned study focused solely on the recovery period. A study by Li et al. (2024), focused on Beijing, is illustrative of much research that has concentrated primarily on the economic recovery phase following the pandemic. Huang et al. (2024) analyzed resilience during the course of the COVD-19 pandemic for urban commercial districts in a specific city, but this study concentrated exclusively on a single sector.

In conclusion, the above studies employed NTL to shed light on how the pandemic has impacted urban activity and economic dynamics at various scales by examining both the immediate effects and the recovery stages and assessing resilience using a range of indicators. Nevertheless, the following has not yet been fully explored by current research: 1) the resilience of different sectors on a global scale; 2) studies concentrating on more than one aspect of urban resilience (such as urban recovery or the immediate impact) and 3) studies focused on the within-city level; finer spatial resolution data are needed for this scale of analysis due to the current NTL data's coarse spatial resolution. Sharpening the current NTL data is crucial since researchers have stated that data with approximately 100 m spatial resolution should be used for city-scale applications (Elvidge et al., 2007).

2.6 Downscaling in remote sensing

In the study of global urban resilience, spatial scale is critical. It is imperative to note that widespread economic shocks of the magnitude associated with a pandemic transpire on a global scale; nevertheless, the multifaceted and heterogeneous repercussions, in conjunction with the disparate resilience dynamics-particularly the discrete responses manifested within urban centers-manifest themselves through meticulous, sector-specific analysis. The aggregation of statistical and social data at the sector scale poses significant challenges, particularly during periods of economic downturn. The temporal proximity to the occurrence of a shock makes it particularly difficult to obtain a comprehensive and clear image of the impact and recovery patterns of the sectors (Cheng et al., 2024). Earth observed NTL data, on the other hand do not suffer from the above issues. Yet, the spatial resolution of NTL data hinders their ability to quantify resilience accurately at the scale of individual cities. Thus, increasing their spatial resolution is essential.

Downscaling is the process of increasing spatial resolution. In remote sensing, downscaling refers to the technique of reducing the pixel size of remotely sensed images (Atkinson, 2013). This objective has been achieved using a variety of approaches, which amounts to an implicit presumption that the downscaled images' information richness will increase (Atkinson, 2013). A variety of techniques exist for downscaling both continua and categories; the specific technique to employ depends on the anticipated type of variable. The latter, referred to as super-resolution mapping (and sub-pixel mapping), has its own research system and is commonly used to produce land use or cover maps. The former is more commonly utilized and it has the potential to produce categorical rasters, post-downscaling, through classification.

There are several methods developed for downscaling continuous data and these can be divided into the following categories: (1) techniques for machine learning, (2) general statistics, (3) wavelet-based, (4) fractal-based, (5) process-based and (6) hybrid methods, as well as (7) spatial statistical analysis (Jin et al., 2018b). One significant advantage of spatial statistical methods - more specifically, geostatistical-based methods - is that they preserve the spectral properties of the observed coarse imagery. This means that the downscaled image will perfectly reproduce the original coarse resolution imagery when it is upscaled to the original coarse spatial resolution, a term called perfect coherence (Wang et al., 2016a). By utilizing the spatial autocorrelation among geographical data, spatial statistical analysis has advanced in downscaling continuous variables, especially in terms of spatial interpolation.

Area-to-point Kriging (ATPK) interpolation is an alternative to general spatial interpolation for addressing the modifiable areal unit problem, when the support (the region that defines each observation) before and after downscaling differs (Atkinson, 2013). Yoo and Kyriakidis improved ATPK by considering the inequality constraints in spatial interpolation (Kyriakidis and Yoo, 2005) while Goovaerts, proposed ATP Poisson Kriging as a means of eliminating noise caused by the small number problem (Goovaerts, 2006). To downscale with several variables, Pardo-Igúzquiza et al. (2006) proposed downscaling coKriging for image sharpening applications. Atkinson et al. (2008) then applied this technique and showed that it could be utilized to downscale continua in remote sensing images. Yet, coKriging is computationally intensive (Wang et al., 2016a). As a result, the ATP regression Kriging (ATPRK) approach was created. Because it incorporates regression kriging and ATPK, it considers both the correlated variables and the change-of-support issue throughout the downscaling process. Furthermore, it has been shown that ATPRK can downscale irregular geographic units (Liu et al., 2008). However, comparable studies that focus on NTL remote sensing imaging are few.

2.6.1 Downscaling NTL

The majority of the methods used today to fuse remote sensing images were developed for fusing optical daytime images (K. Li et al., 2024). In contrast, NTL data captures the spatial distributions of residential and commercial sectors in cities and towns, as well as nighttime road network lighting, and as a consequence, they are dark in areas outside of cities, including rural regions, and even within city limits, such as parks. This results in a significantly higher prevalence of black pixels (i.e., pixels with 0 values, which reduces the accuracy of some statistically based fusion methods (Li et al., 2024). Furthermore, NTL data have coarser spatial resolution than daytime optical remote sensing images, and they are deteriorated by background noise. These limitations are compounded by the number of studies conducted on this subject being limited.

Zhang et al. (2024) utilized geographically weighted regression (GWR) and neural networks to downscale VIIRS data. Multiscale GWR and GWR combined with ATPK were used to sharpen NTL data with other variables (Liu et al., 2022; Ye et al., 2021). When compared to Luojia NTL data, their results demonstrated greater accuracy than alternative approaches and functioned as a more accurate proxy for socioeconomic problems. As the aforementioned examples illustrate, these methods may be divided into two families: (1) deep learning-based (DL) methods and (2) geostatistical-based methods. The main drawback of DL-based methods is that the accuracy of the results is greatly impacted by the quantity and representativeness of the training data, which can be a time-consuming process (Guo et al., 2024). In comparison with DL methodologies, machine learning (ML) techniques, particularly the random forest (RF), exhibit a significantly reduced computational burden. For regression tasks, its main advantages include (1) the flexibility to add or remove variables according to user preferences and the availability of data; (2) the ability to include continuous and categorical predictors; (4) the minimal risk of overfitting; (3) the comparatively small number of model parameters (hyperparameters) the user must specify; and (5) the automatic generation of a variable importance score which assesses each predictor's contribution to the final model (Hutengs and Vohland, 2016). Consequently, the integration of sophisticated machine learning with a geostatistical approach constitutes an uncharted domain within the realm of remote sensing. However, this amalgamation presents a viable methodology for enhancing the spatial resolution of NTL in the context of urban research.

2.7 Summary of NTL-based urban resilience assessment to COVID-19 lockdowns

This section presents a synopsis of the NTL-based urban resilience assessment methods that have been formulated in response to the lockdowns imposed by the pandemic, with the objective of methodically integrating the extant literature on the subject. The aim and breadth of the studies differed. While some have focused on the recovery phase in one or a small number of cities, others have focused on certain industries within a single city. Global-scale research has mostly concentrated on city-level evaluations of the effects of lockdowns, frequently restricted to the first few months of the pandemic. With emphasis on dynamic assessment of the lockdown period, research has investigated GDP implications and economic resilience. While some studies have examined the whole recovery cycle in specific cities, others have concentrated on the immediate effects of the entire lockdown period worldwide. Subsequent studies that examined a single sector within a specific city investigated resilience within that sector. Studies conducted at the city level monitored NTL dynamics over time, showing changes in human activity and the effects of lockdowns. At a few metropolitan agglomerations, other research shed light on the broader impacts and relationships between NTL and economic measures like GDP. A thorough grasp of urban resilience throughout the recovery phase was made possible by some research.

Despite the above, significant gaps still exist. For example, to date, there has been no comprehensive, global evaluation of urban resilience at the sector level. Previous studies have concentrated mostly on fragmented methodologies, ignoring the complex interactions of distinct industries, such as the retail, airport and industrial sectors, to lockdowns generated by the COVID-19 pandemic. Furthermore, the coarse spatial resolution of the NTL data utilized in these studies constrained their ability to identify localized impacts and prevented a comprehensive examination of resilience specific to any given sector. Given the known heterogeneity across sectors in terms of economic activity, labor structures, reliance on supply networks and consumer demand, it is anticipated that these sectors will experience disruptions and recover at different rates. For these reasons, it is imperative to examine urban resilience at the sector level. For example, although different levels of damage and recovery trajectories may be anticipated in retail, airports and industrial regions; they may be hidden in evaluations conducted at the city or national level. A more thorough knowledge of how disturbances spread through various urban functions and how their recovery dynamics develop may be possible by measuring resilience at a more detailed level. This research aims to fill these research gaps and offer insights that are essential for focused urban planning and policy interventions by examining several sectors. The research also analyzes multiple cities from a comparative viewpoint and includes intra-urban differences in resilience.

Chapter 3 Downscaling satellite nighttime lights imagery to support within-city applications using a spatially non-stationary model[1]

---

[1] This chapter is based on the published paper: Tziokas, N., Zhang, C., Drolias, G.C., Atkinson, P.M., 2023, Downscaling satellite nighttime lights imagery to support within-city applications using a spatially non-stationary model. JAG International Journal of Applied Earth Observation and Geoinformation, 122:103395. 10.1016/j.jag.2023.103395

Abstract

For mapping and monitoring socioeconomic activities in cities, nighttime lights (NTL) satellite sensor images are used widely, measuring the light intensity during the night. However, the main challenge to mapping human activities in cities using such NTL satellite sensor images is their coarse spatial resolution. To address this drawback, spatial downscaling of satellite nighttime lights images is a plausible solution. However, common approaches for spatial downscaling employ spatially stationary models that may not be optimal where the data are spatially heterogeneous. In this research, a geostatistical model termed Random Forest area-to-point regression Kriging (RFATPK) was employed to disaggregate coarse spatial scale VIIRS NTL images (450 m) to a fine spatial scale (100 m). The RF predicts at a coarse resolution from fine spatial resolution variables, such as a Population raster. ATPK then downscales the coarse residuals from the RF prediction. In numerical experiments, RFATPK was compared with three benchmark techniques, including the simple Allocation of pixel values from the coarse resolution NTL data, Machine Learning with Splines and Geographically Weighted Regression. The downscaled results were validated using fine resolution Luojia satellite sensor imagery. RFATPK produced more accurate disaggregated images than the three benchmark approaches, with mean root mean square errors (RMSE) for the year 2018 of 13.89 and 6.74 nWcm^{-2}sr^{-1}, for Mumbai and New Delhi, respectively. Also, the property of perfect coherence, measured by the Correlation Coefficient, was preserved consistently when applying RFATPK and was almost 1 for all years. The applicability of the disaggregated NTL data to monitor socioeconomic activities at the within-city scale against the reference NTL was illustrated by utilizing them as a proxy for the Gross National Income (GNI) *per capita* and the Night Light Development Index. The GNI estimation from the downscaled NTL outperformed the coarse resolution NTL when examining their coefficients of determination, with R^2 of 0.7 and 0.5 for the GNI estimation using the fine and coarse resolution NTL data, respectively. For the Night Light Development Index (NLDI), the results of the index were compared by measuring their correlation with the Human Development Index (HDI). The NLDI from the downscaled NTL outperformed the coarse resolution NTL when measuring the correlation with the HDI, with Pearson's correlation coefficients of -0.48 and -0.35 for the NLDI using the fine and coarse resolution NTL data, respectively, for New Delhi. The outcomes indicate that RFATPK provides more accurate predictions than the three benchmark techniques and the downscaled NTL data are more suitable for fine scale socioeconomic applications, as demonstrated by the NLDI and GNI. This research, thus, shows that the RFATPK solution for NTL disaggregation can facilitate data enhancement for fine-scale sub-national applications in social sciences and can be generalized worldwide by including other cities as well as other applications.

Keywords: satellite nighttime lights, downscaling, random forest regression, area-to-point Kriging, spatial non-stationarity, socioeconomic applications

3.1 Introduction

Human development is a crucial factor to consider when assessing a nation's degree of development since it gives inhabitants equal chances and fair choices, extends their lives, and improves their living conditions, health care, and education (Wang et al., 2021). In September 2016, the world committed to implementing the 2030 Agenda for Sustainable Development. The

Sustainable Development Goals (SDGs), according to Reid et al. (2017), strike a balance between the economic, social, and environmental dimensions of sustainable development. Despite decades of tremendous progress in eradicating poverty and fostering wealth, a sizable segment of the world's poorest population still encounters difficulties to maintain an acceptable standard of living in emerging nations, particularly Asia, Africa, and Latin America and the Caribbean. It appears that regional and national differences have led to the unequal reduction of severe poverty in these areas (Georgeson et al., 2016; Omar and Inaba, 2020). To achieve the goals of SDGs, we need better ways to collect and interpret information about many aspects of human development in a timely, accurate and appropriate manner.

The traditional approach to examining human growth and well-being is based mostly on survey data, which includes information on income, consumption, health, education, and housing. These surveys are usually carried out every three to five years, but collecting survey data is expensive and tedious process. Between surveys, detailed socioeconomic data are still needed (Watmough et al., 2013). Moreover, countries in war or extreme poverty may even lack these survey data for years (Zhao et al., 2019). In addition, fewer than two census surveys in many developing nations, such as African nations, were carried out in the decade leading up to 2000, limiting the construction of nationally representative human development metrics (Jean et al., 2016). Additionally, several nations, like India, have suspended measures like unemployment (Dasgupta, 2022). Another limitation of these censuses is that population sizes between censuses are projected, frequently with linear yearly growth rates, despite the fact that censuses are expensive and may only be undertaken at sporadic intervals when resources are scarce. Despite the high levels of uncertainty in the estimates, they are utilized to evaluate, for example, the dangers to public health and need for health services. Additionally, censuses are unable to reflect accurately intra-annual changes in a nation's socioeconomic conditions since they are not designed to do so (Bharti and Tatem, 2018).

Using new passively gathered data sources, such as information from satellite sensors, provides an alternate method of monitoring socioeconomic processes. Such data can help address the challenge of scaling up (i.e., increasing the temporal resolution of) traditional data collection efforts which are generally very limited in frequency due to financial cost (Jean et al., 2016). Early studies used satellite "nightlights" data to demonstrate that areas with more economic output tended to emit more artificial light (Head et al., 2017). Nighttime lights images, such as the Day-Night Band (DNB), from the Visible Infrared Imaging Radiometer Suite (VIIRS) is a valuable source of satellite imagery. The VIIRS is onboard the Suomi National Polar-orbiting Partnership (SNPP) satellite. The ability for researchers to track socioeconomic activity is made possible by the worldwide coverage and coarse spatial resolution of these data, which have pixels that are less than one square kilometer in size. Additionally, nighttime lighting is consistently assessed across nations with extremely diverse institutional capacity and is not prone to manipulation for political reasons (Zhang and Gibson, 2022). When compared to commercial fine-resolution images like EROS-B or JL1-3B, NTL products (like VIIRS DNB images) are available for free and have a considerably larger swath (Levin et al., 2014). The NPP-VIIRS NTL has a spatial resolution of 15 arc seconds (or approximately 500 m at the Equator), which has the potential to support several practical applications like mapping at the country level, detecting military conflicts and assessing poverty (Levin et al., 2020; Gibson et al., 2021).

NTL has achieved extensive research and applications in socioeconomic fields. The so-called Night Light Development Index (NLDI), proposed by Elvidge et al. (2012) from nighttime satellite sensor images and population density, evaluates disparities in the local population's geographical distribution of night light. Using deep learning techniques, Bruederle and Hodler (2018) demonstrated that NTL data are a suitable proxy for wealth and human development in 29 African countries. Similar to the previous study, Yeh et al. (2020) estimated the wealthiness of 20,000 African villages using a combination of NTL data and daylight satellite sensor optical data, and found that their technique could account for 70% of the variation in ground-measured village wealth. Gosh et al. (2013) provided examples of numerous ways to gauge one's level of wellbeing. Elvidge et al. (2011) used NTL satellite sensor imagery and population data to estimate the number of people worldwide who have (or do not have) access to electricity. This is done because a lack of electricity is a sign of poverty and is associated with conditions that are detrimental for health and wellbeing, including the inability to refrigerate food, have access to clean water, and have adequate sanitary facilities. NTL and artificial neural networks were utilized by Jasiński (2019) to gauge electricity usage at the Nomenclature of territorial units for statistics (NUTS) 2 level.

Mapping and monitoring complex urban socioeconomic processes, particularly those that take place within cities, can be challenging with NTL images since they often have a coarse spatial resolution (Levin et al., 2020; Ye et al., 2021). According to Elvidge et al. (2007), the coarsest acceptable spatial resolution of a satellite sensor image should exceed 100 m to research socioeconomic issues at the city scale. Moreover, it can be important to track human development over time to determine if it is improving or developing. For example, a finer spatial resolution is typically needed than the 450 m pixel size of VIIRS to accurately quantify development growth rates at the scale of individual cities. These problems significantly hinder NTL applications, especially at the city-scale. Enhancing the spatial resolutions of NTL satellite sensor imagery products is increasingly urgent because the majority of the world's population, after 2007, is concentrated in urban areas (Marlier et al., 2016).

In remote sensing, spatial downscaling can be categorized in two classes based on their output prediction, namely downscaling continua and sub-pixel mapping (SPM) (Wang et al., 2020). Whereas the first class predicts continua (e.g., in units of reflectance, brightness, etc.), the latter class, also known as super resolution mapping in the remote sensing literature, predicts categories (i.e., land cover class labels) (Wang et al., 2020). Downscaling continua can create categorical products by classification and is more often used. Generally, the methods for disaggregating continua can be classified into the following classes: general statistical, spatial statistical, machine learning, process-based, wavelet-based techniques, fractal techniques and hybrid methods (Park et al., 2019). Spatial statistical analysis has advanced the downscaling of raster images (i.e., satellite remote sensing images), notably in terms of spatial interpolation, by taking advantage of the spatial autocorrelation among geographical data. Area-to-point (ATP) interpolation, as opposed to generic spatial interpolation, can address the problem of changeable areal units, when the supports before, and during, downscaling are different (Kerry et al., 2012; Wang et al., 2016a). By making sure, for instance, that the total of the downscaled forecasts within each region equals the initial aggregated count, ATP Kriging (ATPK) assures the coherence of predictions (Kyriakidis and Yoo, 2005). Yoo and Kyriakidis (2006) expanded on ATPK by taking the inequality limitations in spatial interpolation into account. ATP interpolation emphasizes utilizing the information offered by correlated variables since it can help in exploring the spatial variation of response variables at a higher spatial resolution.

Wang et al., (2016b) further extended ATPK by introducing a regression term and they named the method area-to-point regression Kriging (ATPRK). ATPRK is a geostatistical technique used frequently for downscaling day-time satellite sensor images. For example, Wang et al. (2015) used ATPRK to downscale MODIS data and further employed it to downscale Landsat satellite sensor images and Worldview-2 images (Wang et al., 2016a). Using multispectral satellite sensor imagery, Zhang et al. (2021) developed object-based ATPRK to disaggregate IKONOS images. Wang et al. (2017) implemented a spatio-temporal fusion method by combining MODIS and Landsat data, downscaling 500 m MODIS data into 250 m as an initial step. Jin et al. (2018b) utilized Geographically Weighted Area-to-Point Regression Kriging (GWATPRK), a spatially non-stationary method, to create a 1 km Surface Soil Moisture product. Xu et al. (2020) downscaled ASTER thermal images using Random Forest ATPK. The majority of the above research, as stated in the examples, aimed to downscale day-time satellite sensor data. However, the remote sensing of nighttime lights has the potential to capture human socioeconomic activities and/or track human development compared to day-time satellite sensor data, which is critical in modelling complex urban environments for certain applications (Elvidge et al., 2017) and downscaling is potentially useful in this context. Thus, there exists a gap in the literature. However, the spatial pattern of NTL is diverse. For example, the light intensity differs depending on the land use (Ye et al., 2021), and the spatial pattern of NTL intensity varies from geographic region-to-region, even within the same area (e.g., city).

Earth-observed variables also may exhibit spatial heterogeneity in addition to spatial autocorrelation (Jin et al., 2018b). For such spatially diverse variables, the global model used in ATPRK may be unable to adequately capture local characteristics in the multivariate data. In essence, the global ATPRK model assumes that the process under inquiry is constant across space. Where the data exhibit spatial heterogeneity a more flexible model is needed; one that permits spatial non-stationarity in some model parameters.

Wang et al. (2016a) extended the ATPRK by incorporating and adaptive window for the regression part in order to account for the data's spatial heterogeneity. An ordinary linear regression model was fitted using a coarse target variable and covariates within a local window, that is, a global regression model within the constricted region. On the other hand, Random Forest regression (RF) is a well-known non-stationary regression technique that takes into account non-linear correlations between variables and has been frequently utilized for spatial analysis, either alone or in combination (Xu et al., 2020; Tang et al., 2021). Xu et al. (2020) proposed RF area-to-point regression Kriging (RFATPK) for downscaling ASTER land surface temperature data. Cheng et al., (2022) utilized a RF and ATPK to estimate monthly population distribution in China. However, only a few related studies exist focusing on downscaling satellite nighttime lights images, mainly for impervious surface identification (Ye et al., 2021). To the authors' knowledge, there hasn't been any prior research that specifically addresses NTL continua for socioeconomic applications.

To account for the issue of local heterogeneity and multivariate non-linearity, this research proposes the combination of RF and ATPK for disaggregating NTL using fine-spatial-resolution predictors (e.g., WorldPop products). The suggested RFATPK technique captures the spatially non-linear correlations between the dependent and auxiliary variables while preserving the benefits of ATPRK. The advantages of the proposed algorithm are: (1) RF can process high-dimensional data. (2) Overfitted phenomena do not easily occur, because the final estimation is made through the average prediction of the decision trees. (3) For a large number of remote sensing images and/or observations, training a RF model is fast and efficient. (4) RF is immune to statistical assumptions compared to the original ATPRK. (5) Another advantage is its ability to capture complex and non-linear relationships between predictors and the response variable (Brokamp et al., 2017). By downscaling NTL satellite sensor images from the VIIRS sensor from 450 m to 100 m, two practical socioeconomic applications were executed to test this approach. The applications involved the Gross National Income (GNI) and Night Light Development Index (NLDI) for New Delhi and Mumbai, two megacities of the developing world. Disaggregated NTL data at this spatial resolution have the potential to be utilized for monitoring such human development indicators at the city-scale. The research's contributions are, thus, two-fold.

1. The geostatistical approach, ATPRK, combined with a spatially non-stationary model, was applied to downscale NTL images for the first time. To show that RFATPK is superior than the three previous well-known downscaling methodologies, a benchmark comparison between the three approaches and RFATPK was performed.
2. The spatial downscaled NTL data were further applied to estimate the GNI as well as to measure light inequality at the within-city scale by comparing them with equivalents using the coarse spatial resolution NTL.

The remainder of this research paper is organized as follows. The research areas and the data used are described in Section 3.2. The suggested downscaling technique is described in Section 3.3. We give the results in Section 3.4. We expand on the suggested downscaling approach in Section 3.5 before presenting our conclusions in Part 3.6.

3.2 Study areas and data

3.2.1 Study area

New Delhi and Mumbai were chosen as the areas under investigation to manifest the utility of the technique (Figure 3-1). New Delhi is India's capital and a densely populated metropolis (~10,400 people per km^2) with a population of about 16 million people and it is a key international hub on the Asian sub-continent. The city has experienced rapid urbanization and industrialization, with 93% of the population residing in urban areas compared to the national average of 31.16%. There are 675 slum clusters in New Delhi (Figure 3-1) (Bhanarkar et al., 2018; Malik et al., 2022). The Mumbai Metropolitan Region, including Mumbai and its surrounding suburban area, is known as India's economic engine as it accounts for over 6.16% of India's GDP, providing 10% of industrial jobs. More than 20 million people live in this territory today and this amount is predicted to increase by 10.36 million by the end of 2036. Mumbai, like New Delhi, has a large number of slums, with an estimated number of 67 (Nijman, 2010; Vinayak et al., 2021).

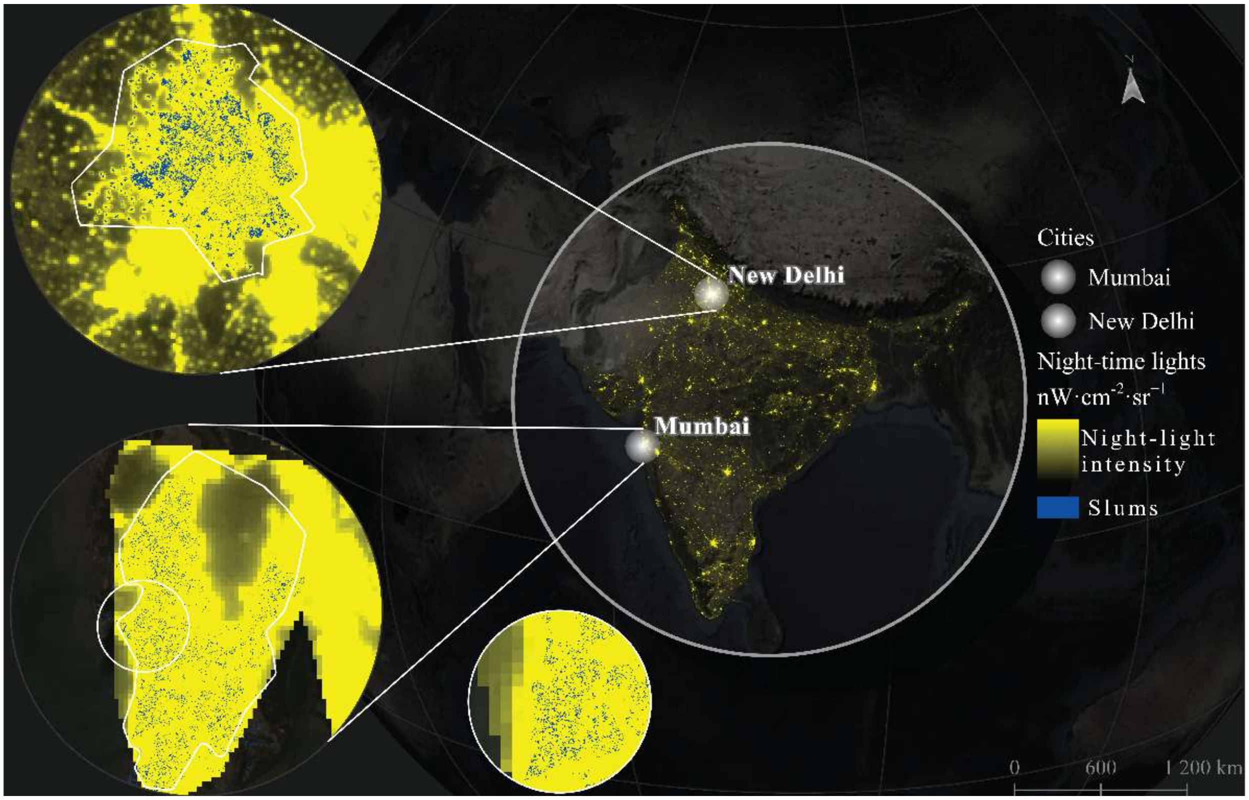

Figure 3-1: Location and maps of the two cities of New Delhi and Mumbai.

3.2.2 Datasets

Remote sensing nighttime lights images, population count, Landsat's 8 thermal band and the global human settlement layer data were used. A summary of these follows below:

Table 3-1: Spatial datasets used in nighttime lights mapping and downscaling for Mumbai and New Delhi.

Dataset	Spatial resolution (m)	Year	Data source
Version 2.1 VIIRS DNB (mean)	450	2013 - 2020	(Elvidge et al., 2021) (accessed 10/01/2023).
WorldPop count (contstrained)	100	2013 - 2020	(Tatem, 2017) (accessed 10/01/2023)
Median Landsat 8 (TIRS)	100	2013 - 2020	Google Earth Engine (Gorelick et al., 2017)
Global Human Settlement (GHS)	100, 10	2015, 2018	(Pesaresi et al., 2024) (accessed 10/01/2023)
Luojia	120	2018	http://59.175.109.173:8888/index_en.html (accessed 10/01/2023)

3.3 Methodology

The Methodology is organized as follows: (1) Firstly, a brief introduction of the ATPRK is given. (2) A detailed explanation of the proposed RFATPK and its parts (i.e., RF regression and ATPK) follows. Additionally, a description of the benchmark methods is given and lastly the two socioeconomic applications. Figure 3-2 summarizes the methodology as a series of successive steps designed to meet the research objectives. The first part includes selection of the Inputs (the target variable and the covariates), namely the NTL data, WorldPop product, the LST band from Landsat 8 and the GHS and AGBH layers, respectively. Then, the data were regressed utilizing RF regression, and the predictions were separated from the residuals. In the third part, the residuals from the RF model were downscaled using ATPK. Finally, the prediction was added to the downscaled residuals and the NTL raster layer at 100 m spatial resolution was produced.

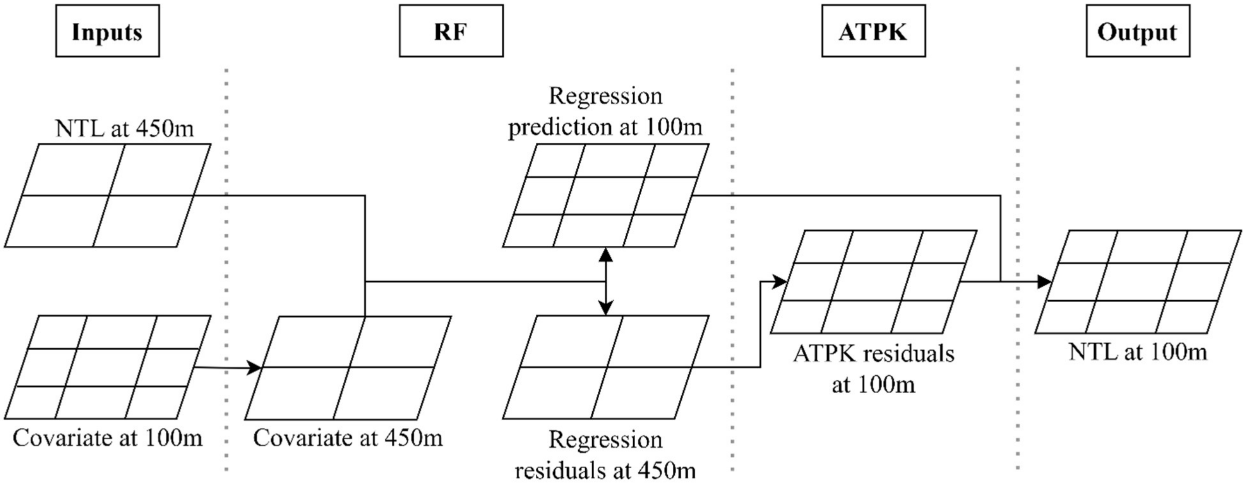

Figure 3-2: Flowchart of RFATPK. The first part includes the Inputs as the target variable and the covariate. In the second part, the input data are regressed using Random Forest regression. The third part involves ATPK-based downscaling of the residuals. Finally, the prediction is added to the downscaled residuals and the NTL raster layer is produced at 100 m spatial resolution.

3.3.1 Downscaling

ATPRK is a spatial downscaling method that applies a regression model to coarse spatial resolution data and subsequently applies ATPK to enhance the spatial resolution of the residuals (Wang et al., 2016a). The regression component alone is insufficient for disaggregation because it does not utilize fully the spectral characteristics in the observed low-resolution data. As an addition to the regression step, ATPK-based residual downscaling is utilized to account for the spectral characteristics of the coarse data. The ATPK component is a sharpening method that predicts values on a smaller pixel (i.e., support) than the original, coarse scale, data (Kyriakidis, 2004; Kyriakidis and Yoo, 2005; Atkinson, 2013). It varies from conventional Kriging in that it takes into account the observation's spatial support, and it accounts for the size of support, spatial correlation and the point spread function (PSF) of the sensor, instead of treating each observation as a centroid. Moreover, a crucial advantage of ATPK is, the so-called, property of perfect coherence (Kyriakidis, 2004; Kyriakidis and Yoo, 2005): that is, it can maintain accurately the spectral features of the nominal coarse data.

The regression model in ATPRK has two parts, the prediction and the residuals. The residuals can be extracted as follows:

$$e(S_i) = z(S_i) - [\beta_0 + \sum_{k=1}^{K} \beta_k * h_k(S_i)] \tag{1}$$

where $e(S_i)$ are the coarse residuals, β_0 and β_k are coefficients of the linear regression, $z(S_i)$ is the target random variables of coarse pixel S_i and $h_k(S_i)$ is the aggregated fine pixel within the coarse one.

The coarse residuals are downscaled using ATPK. The residual of a fine-resolution pixel s_j is estimated as a linear fusion of $e(S_l)$ ($l = 1, \ldots, L$) in L nearest coarse pixels, via ATPK:

$$e(s_j) = \sum_{l=1}^{L} \lambda_{jl}\, e(S_l) \tag{2}$$

where λ_{jl} represents the weights for the prediction at fine scale that honor the sum-to-one constraint $\sum_{l=1}^{L} \lambda_{jl} = 1$. The weights can be calculated by lessening the error variance of the prediction. The analogous Kriging matrix is depicted in Equation 6:

$$\begin{bmatrix} \gamma_{11}^{SS} & \gamma_{1L}^{SS} & 1 \\ \vdots & \ddots & \vdots \\ \gamma_{L1}^{SS} & \gamma_{LL}^{SS} & 1 \\ 1 & 1 & 0 \end{bmatrix} \begin{bmatrix} \lambda_{1j} \\ \vdots \\ \lambda_{jL} \\ \mu_j \end{bmatrix} = \begin{bmatrix} \gamma_{1j}^{Ss} \\ \vdots \\ \gamma_{Lj}^{Ss} \\ 1 \end{bmatrix} \tag{3}$$

where γ_{ij}^{SS} is the block-to-block (i.e., area-to-area) variogram among coarse pixels S_i and S_j, C_{jj}^{ss} is the point-to-point covariance between fine spatial resolution pixels s_j and s_j, γ_{lj}^{Ss} is the ATP variogram between high resolution pixel s_j and coarse resolution pixel S_l and the μ_j are Lagrange multipliers. The covariance can be produced from the variogram.

The error variance δ of the ATPK prediction for the s_j at fine-resolution can be calculated as follows:

$$\delta_{ATPK}(s_j) = C_{jj}^{ss} - \sum_{l-1}^{L} \lambda_{jl} * C_{lj}^{Ss} - \mu_j \tag{4}$$

is C_{lj}^{Ss} the area-to-point covariance between coarse spatial resolution pixels S_l and fine spatial resolution pixels s_j.

The generation of the point support variogram is considered the most crucial step in area-to-point Kriging method, for which Wang et al., (2016b) provides the necessary details, including an explanation of how to employ a deconvolution process. The target fine pixel and the original coarse pixel can be used as point and area supports, respectively, in the ATPRK prediction, which can be described as follows:

$$z(s_j) = \hat{\beta}_0 + \sum_{k=1}^{K} \hat{\beta}_k * h_k(s_j) + \sum_{l=1}^{L} \lambda_{jl} * [z(S_l) - (\hat{\beta}_0 + \sum_{k=1}^{K} \hat{\beta}_k * h_k(S_l)] \tag{5}$$

3.3.2 Random Forest area-to-point Kriging

In the presence of spatial variability in a region, the global regression approach in the original ATPRK implementation is unsuitable for characterizing this variability. A non-stationary model is more appropriate when the association between the target and variable and the covariates varies geographically (Jin et al., 2018b, 2018a). The global regression residuals, on the other hand, may not meet stationarity criteria (such as second-order stationarity), making Kriging interpolation hard to implement (Jin et al., 2018b). Moreover, to account for the spatial variability in the correlation between the variables, RF regression generates local coefficients (Jin et al., 2018b; Pereira et al., 2018).

RFATPK is proposed in this research to increase downscaling accuracy by taking into account spatial non-stationarity. The trend and residuals are likewise included in RFATPK, with the trend being fitted utilizing the RF approach (Equation 2). To predict the spatial trend at fine scale, RFATPK first fits the RF regression model between the response variable and the covariates at the coarse spatial resolution. The regression residuals are then disaggregated at the desired pixel size using ATPK (Xu et al., 2020; Cheng et al., 2022). After the regression using RF, the model's errors (i.e., residuals) are expected to be less heterogeneous and assure the requirements for semivariogram estimation (i.e., sufficiently large and homogeneous areas) (Jin et al., 2018b). In this research, a deconvolution procedure was utilized to implement the ATPK predictions and the spherical model was fitted to the experimental variograms (Goovaerts, 2008). This algorithm for enforcing ATPK requires inversion of a large matrix, which is computationally expensive. For the downscaling process the R (R Core Team, 2025) software and the package *atakrig* (Hu and Huang, 2020) were utilized.

To generate the downscaled 100 m NTL, the RFATPK disaggregating approach of combining the RF (Breiman, 2001) and ATPK (Kyriakidis, 2004) methods was developed. The spatial non-stationarity of the regression's residuals was taken into account by the RFATPK, as well as the nonlinear association between NTL and the covariates.

Suppose $Z_C^l(x_i)$ are the pixel values (i.e., gray value) of pixel C located at x_i (i = 1, . . ., M, where M is the number of pixels) in coarse image l (l = 1, . . ., B, where B represents the amount of images) and $Z_F(x_j)$ is the value of pixel F centered at x_j (j = 1, . . ., MG^2, where G is the zoom factor between the coarse and fine bands) in the stack layers. The letters F and C represent the fine and coarse pixels, respectively. The goal of sharpening is to predict response variables $Z_F^l(x)$ for all fine pixels in all B coarse images. RFATPK consists of two steps: RF regression and residual downscaling using ATPK. Assume $\hat{Z}_{F1}^l(x)$ and $\hat{Z}_{F2}^l(x)$ are predictions of the RF regression and ATPK parts, the RFATPK forecast is:

$$\hat{Z}_F^l(x) = \hat{Z}_{F1}^l + \hat{Z}_{F2}^l \tag{6}$$

3.3.2.1 Random Forest Regression modelling for the trend prediction

The RF is a non-parametric machine learning (ML) method for regression tasks (Breiman, 2001), which has been applied to fields such as, population mapping and properties relating to the soil (Cheng et al., 2022; Takoutsing & Heuvelink, 2022). Based on bagging method of the training data, the RF constructs an ensemble or forest of individual and non-correlated trees, saves the best randomly chosen variable combination for each node of each tree, and then uses an average of the individual trees' predictions to make the final prediction (Cheng et al., 2022).

Since they offer more useful higher spatial resolution and richer textural information than the response low resolution variable, the covariate(s) in RFATPK (e.g., the Population raster) are utilized to detrend the $Z_F^l(x)$ and are crucial in sharpening. The regression stage aims to fully use the fine spatial resolution textural and geographic information in the given data by characterizing the correlation between each coarse response image and the fine predictors.

A fine-scale predictor (e.g., Population raster) Z_F is initially aggregated to Z_C to match the pixel size of the coarse response image (Wang et al., 2016a). The relationship between Z_C and each coarse band l is then established by RF regression.

The generic equation of the RFATPK involves two parts, the trend component and the residuals component, and can be written as:

$$Z_C^l(x) = f(B(x_i|\theta) + R(x) \tag{7}$$

Where f is a RF model, $B(x_i)$ represents the predictors at location x_i, θ constitutes the model's parameters and $R(x)$ are the residuals, or model error. The RF-based nonlinear regression model (θ) in Equation 7 can receive the fine resolution predictors directly, based on the scale-invariance assumption. The NTL spatial trend can then be produced at a downscaled 100 m spatial resolution. Due to the availability of the predictors at the fine spatial scale, the RF regression prediction at a location x at the fine spatial scale, that is, $\hat{Z}_{F1}^l(x_0)$, is calculated as:

$$\hat{Z}_{F1}^l(x_0) = f(B(x_i|\theta) \tag{8}$$

It is crucial, when using RF, to fine-tune the model parameters (Takoutsing and Heuvelink, 2022).

3.3.2.1.1 Default Random Forest regression model parameters at the coarse spatial scale

First, we used R's (R Core Team, 2025) *caret* (Kuhn, 2008) package to conduct RF regression using all the covariates and the default model settings. 500 trees, a node size value of 5 and a third of the total number of covariates (*mtry*) were included in the default model parameters. The entire study region was considered in this step.

3.3.2.1.2 Model calibration and fitting

The study region was divided initially into two sets, the training and a test set. The splitting of the two sets was conducted based on a stratified random sampling. This is an efficient sampling method because it captures the variability of multiple inputs of auxiliary information in the feature space (Getis and Ord, 1992). At the 450 m, the training and test samples for Mumbai were 1617 and 450, respectively, while for New Delhi there were 5852 and 450. For the 2025 m scale, the splitting sets for Mumbai were 79 and 20, while for New Delhi there were 285 and 72 for the training and test set, respectively. The RF model was then calibrated using the training data and its performance was assessed using the test set. We applied the model to the entire region if the R^2 difference between the training and test sets was minimal. Two user-defined arguments (the number of trees (*ntree*) and the number of variables chosen at each split (*mtry*) were used to calibrate the RF model (Probst and Boulesteix, 2018). For the *ntree* parameter, we investigated a range starting at 500 and increasing to 9000 with a step of 500. The default setting for *mtry* was the third the total number of covariates, rounded down. With the help of the R (R Core Team, 2025) package *ranger* (Wright and Ziegler, 2017), we fitted a final RF model for each annual NTL image using all of the pixel data, the predictors and the chosen fine-tuned arguments for the *ntree* and *mtry*.

3.3.2.3 Spatial prediction at the fine spatial scale

The average of all measurements embedded in one of the end nodes of the tree serves as the forecast of a single decision tree of RF for a new site x_0. By branching through the tree depending on the covariate values at x_0, the end node may be located.

The RF prediction can be calculated by taking the mean of all tree forecasts. Because it is a weighted linear combination of the measurements, it can be represented as:

$$\hat{Z}_{F1}^{l}(x_0) = \sum_{i=1}^{n} w_i * y_i \tag{9}$$

where $\hat{Z}_{F1}^{l}(x_0)$ stands for the prediction, n, w_i and y_i are the number of measurements, the weights and the NTL measurements, respectively. Note that the weights are obtained from the variables at the observed and predicted location, even though this isn't stated explicitly in Equation 1. (Takoutsing and Heuvelink, 2022).

3.3.3 Benchmark methods

In this research, the proposed approach was compared to three benchmark methods, namely GWR, Machine Learning with Splines and the Allocation of raster values. The benchmark methods are described below.

Prior to GWR, simple linear regression models were, thereafter, fitted to reveal the model's R^2 and AIC (Middya and Roy, 2021; Wang et al., 2015). The covariates that contributed to the linear model with the largest R^2 were also used for GWR. The GWR model, can be represented as follows:

$$z(s_j) = \hat{\beta}_0(s_j) + \sum_{k=1}^{K} \hat{\beta}_k(s_j) * h_k S_j \tag{10}$$

where, $\hat{\beta}_0(\cdot)$ and $\hat{\beta}_k(\cdot)$ represents the estimated GWR coefficients with spatial locations centered at fine pixel s_j and coarse pixel S_j, respectively.

For GWR's kernel a Gaussian function was selected and the width of the kernel was determent using an adaptive spatial kernel function (Chen et al., 2015). The Gaussian function describes the relationship between the weight W_{ij} and distance from center d_{ij} and is a continuous monotonically decreasing function. The Gaussian function is used widely:

$$W_{ij} = exp\,(-\,d_{ij}^2/b^2) \tag{11}$$

where b and d_{ij} are the kernel bandwidth and the distance between two locations i and j, respectively. According to Chen et al. (2015) the regression results are sensitive to parameter b which can, thus, be obtained by cross-validation.

Machine Learning with Splines (ML with Splines), in order to predict the dependent variable, the algorithm tries many ensembles of six and giving one ensemble as an output, weights them differently and evaluates the fit. Six algorithms are included in this approach, namely: 1) boosted regression trees, 2) generalized additive model, 3) multivariate adaptive regression splines, 4) neural networks, 5) RF, 6) support vector machines. The algorithm interpolates noisy multivariate data through ensemble machine learning (EML). Additionally, using thin-plate-smoothing splines, the residuals of the final model are interpolated from the full training dataset. In the final ensemble model, this produces a continuous error surface that is used to eliminate the majority of the remaining errors (Bullock et al., 2020). The R (R Core Team, 2025) package *MACHISPLIN* (Brown, 2023) was utilized.

With the allocation-based method, a new fine spatial resolution raster (i.e., 100 m pixel size) is created with null cell values, but with the same spatial reference system as the coarse resolution raster and then the two rasters are properly overlaid. Then, the pixels of the newly created empty raster are given a value corresponding to the pixel value of the overlaid coarse spatial resolution raster. This approach, thus, represents the "do nothing" or "null" baseline and all other methods of allocation should improve on this baseline if they add any useful information.

3.3.4 Two socioeconomic criteria

The use of NTL as a proxy to various socioeconomic indexes is a major application. Therefore, the application of downscaled imagery to proxy the Gross National Income *per capita* and the Night Light Development Index (NLDI) is meaningful to illustrate the necessity of downscaling.

Payments go toward a country's Gross National Income (GNI), which is comprised of the GDP plus net revenues from employee compensation and foreign property income. The money that foreign migrants send to their home nations is known as remittances (Ghosh et al., 2009). To measure the association between the GNI and the NTL at the city scale, we sum all the lit pixels of the NTL, where "lit pixel" means a radiance value equal to or greater than 1 $\text{nWcm}^{-2}\text{sr}^{-1}$. Then we computed two linear regression models, one using the coarse resolution NTL as explanatory variable and one linear model using the disaggregated NTL and compared their R^2 values (Gibson and Boe-Gibson, 2021). The dependent variable in both cases was the GNI and it was measured in 1000 US dollars.

The NLDI varies from 0 to 1, representing perfect equality and inequality, respectively. The two geo-referenced gridded layer inputs to the NLDI were the population count raster and the NTL image.

The brightness (NTL's pixel value) and population count were associated in tables created using crosstabulation. In order to compute the NLDI, the two rasters were stacked and the joint distribution of brightness and population count in cell was calculated. To measure equality in the geographic distribution of lights, the Gini index was computed based on the statistical distribution (i.e., the table containing the pixel values of NTL and Population, sorted by the NTL) according to the formula:

$$R = 1 - \frac{2\sum_{i=1}^{n-1} Q_i}{n-1}, 0 \leq R \leq 1 \tag{12}$$

where R and n represents the NLDI and the number of raster images, respectively, $Q_i = \sum_{j=1}^{i} x_j / \sum_{j=1}^{n} x_j$ is the number of lights corresponding to the raster with the proportion P_i of population count in which x_j is the value of light intensity class. Moreover, $P_i = \sum_{j=1}^{i} x_j / n$.

3.4 Results

The experiments were conducted in the two mega-cities each month between 2013 and 2020. To evaluate the results of downscaling, due to a lack of validation data at 100 m for each year, we upscaled the NTL observations to 2025 m spatial resolution and used the original NTL data at 450 m spatial resolution as the reference (Ge et al., 2019). In the downscaling stage, the coarse 2025 m NTL data were disaggregated to the initial finer spatial scale (450 m) and were validated using the raw NTL data.

Lastly, the sharpening was conducted to the 450 m data to predict NTL at the 100 m. For the year 2018 the downscaled results were compared against Luojia as an extra validation step. Additionally, because the variogram can reflect the benefits of downscaling prediction, it can be used as an assessment metric when there is no reference data available at the fine spatial resolution. Thus, here, the downscaling predictions at 100 m spatial resolution were also evaluated using the variogram (Wang et al., 2020).

3.4.1 Comparison with other downscaling methods

3.4.1.1 Downscaling prediction (2025 m to 450 m)

To validate the proposed approach, the predicted NTL images were compared against the predictions of three benchmark methods, and the results were illustrated in Figure 3-3 and Figure 3-4 for Mumbai and New Delhi, respectively. It can be shown that RFATPK and GWR-based downscaling achieved good agreement with the original NTL product when comparing the spatial patterns of the downscaling results with the Reference image. Although local detailed variance may be seen, the RFATPK prediction shows it more clearly. In comparison, the blocky artifacts are highly noticeable and Machine Learning with Splines and Allocation-based downscaling failed to maintain the patterns in NTL. For the instance of Machine Learning using Splines, over-fitting issues can be used to explain this outcome. Since the raw NTL coarse reference data are known perfectly in the experiment, preservation of the original patterns is the desired target.

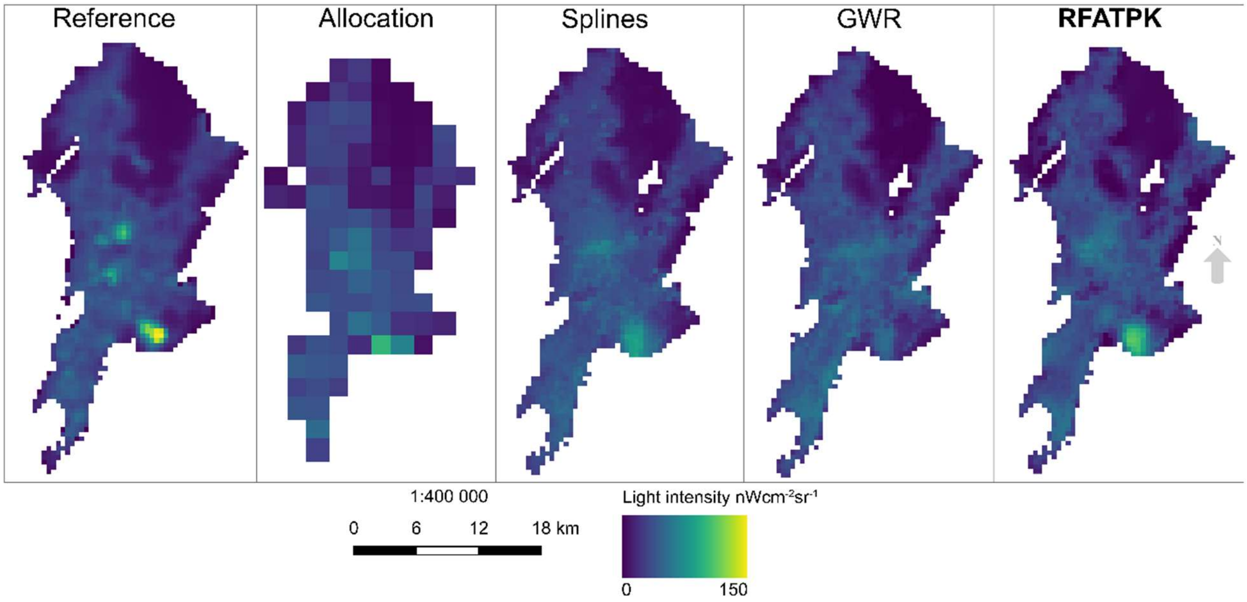

Figure 3-3: Downscaling results of NTL at 450 m for Mumbai, 2018. From left to right, the Reference NTL, Allocation-based downscaled NTL, Machine Learning with Splines-based downscaled NTL, GWR-based and RFATPK-based downscaled NTL. **Bold** shows our proposed method.

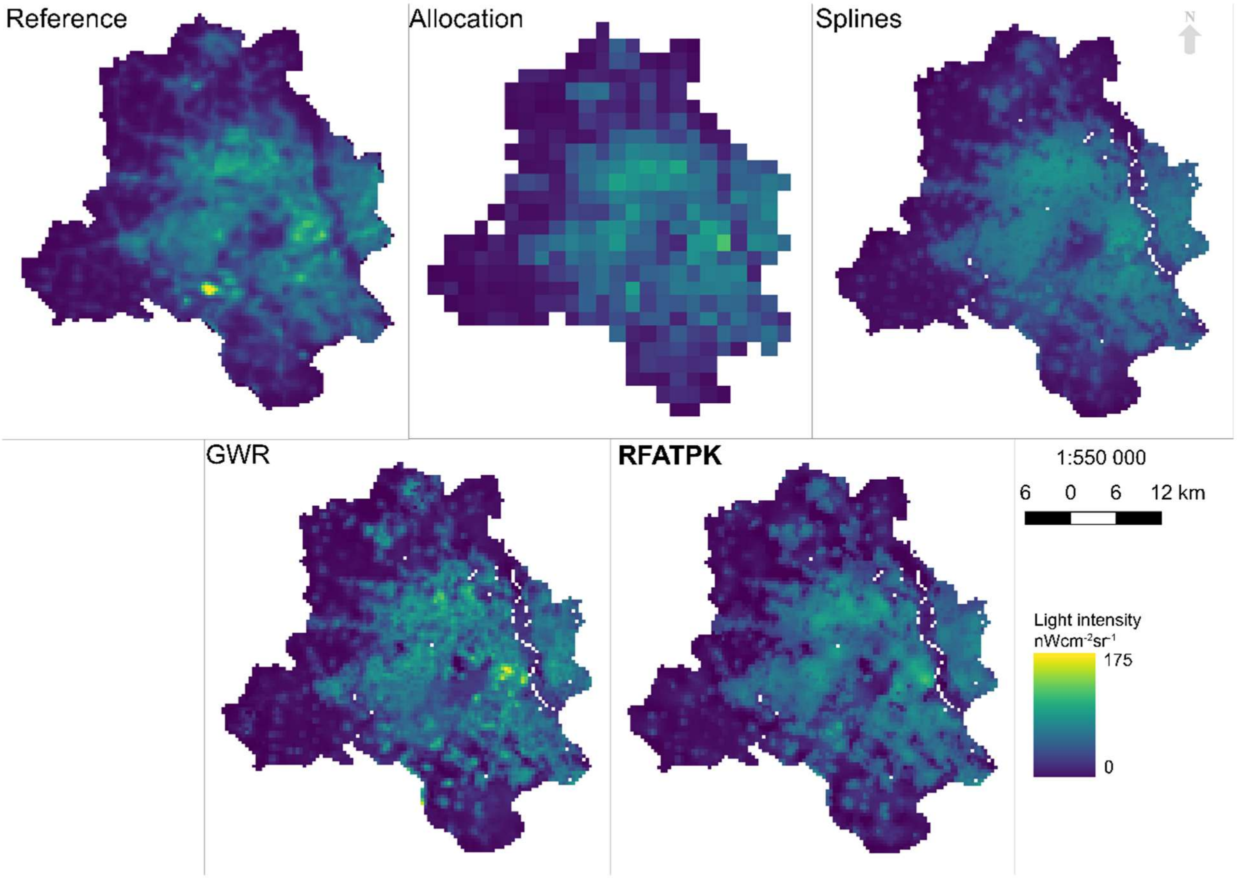

Figure 3-4: Downscaling results of NTL at 450 m for New Delhi, 2018. From left to right, the Reference NTL, Allocation-based downscaled NTL, Machine Learning with Splines-based downscaled NTL, GWR-based and RFATPK-based downscaled NTL. **Bold** shows our proposed method.

Table 3-2 and Table 3-3 provide a quantitative comparison of the downscaling methods using three indices: Root Mean Square Error (RMSE), Mean Square Error (MSE) and Correlation Coefficient (CC). RFATPK demonstrated improved performance over the three benchmark methods across all three indices. This is due to the fact that the scenes under study are highly developed metropolitan environments with a variety of impervious surfaces (such as buildings, roads, and vegetation), which are better suited to being well described by a spatially non-stationary model. Machine Learning with Splines yielded greater accuracy compared to GWR and Allocation-based downscaling. The least accuracy resulted in GWR-based downscaling, in terms of all three indices.

Table 3-2: Performance metrics (Root Mean Squared Error (RMSE), Mean Squared Error (MSE), Correlation Coefficient (CC)) for quantitative comparison of downscaling approaches at 450 m resolution in Mumbai, using original NTL data as reference. **Bold** values indicate the best-performing method for each metric.

		2013	2014	2015	2016	2017	2018	2019	2020
RMSE	Allocation	10.1172	14.2775	10.9951	11.7604	11.8663	12.9181	15.5305	16.1761
	ML with splines	10.3092	16.5331	10.5267	11.0395	11.3876	12.1660	15.4108	15.8129
	GWR	11.3387	17.8948	11.9249	12.9232	13.3665	14.0287	17.8138	17.9765
	RFATPK	**1.7165**	**2.7673**	**2.0354**	**2.1364**	**2.7848**	**2.4980**	**4.1899**	**3.4906**
MSE	Allocation	102.3590	203.8480	120.8930	138.3070	140.8100	166.8770	241.1980	261.6680
	ML with splines	106.2790	273.3430	110.8110	121.8700	129.6780	148.0130	237.4940	250.0490
	GWR	128.5670	320.2240	142.2050	167.0090	178.6640	196.8040	317.3320	323.1570
	RFATPK	**2.9464**	**7.6583**	**4.1429**	**4.5645**	**7.7555**	**6.2403**	**17.556**	**12.1843**
CC	Allocation	0.8187	0.7839	0.7893	0.7918	0.7817	0.7818	0.7610	0.7254
	ML with splines	0.8041	0.6724	0.8005	0.8116	0.7911	0.8002	0.7515	0.7224
	GWR	0.7566	0.5985	0.7342	0.7295	0.6961	0.7224	0.6470	0.6181
	RFATPK	**0.9950**	**0.9923**	**0.9932**	**0.9935**	**0.9887**	**0.9923**	**0.9838**	**0.9884**

Table 3-3: Performance metrics (Root Mean Squared Error (RMSE), Mean Squared Error (MSE), Correlation Coefficient (CC)) for quantitative comparison of downscaling approaches at 450 m resolution in New Delhi, using original NTL data as reference. **Bold** values indicate the best-performing method for each metric.

		2013	2014	2015	2016	2017	2018	2019	2020
RMSE	Allocation	9.4589	9.0099	9.1661	8.1967	8.5255	8.3571	8.4641	7.5097
	ML with splines	9.0594	9.1414	8.0654	7.8573	7.7100	7.5779	8.5324	6.5307
	GWR	9.8107	10.057	10.7049	8.9059	9.6294	8.9825	9.3896	8.5971
	RFATPK	**2.5113**	**2.2719**	**2.5727**	**2.1916**	**2.3779**	**2.1511**	**1.8615**	**2.0369**
MSE	Allocation	89.4710	81.1797	84.0189	67.1861	72.6850	69.8423	71.6414	56.3963
	ML with splines	82.0733	83.5664	65.0510	61.7373	59.4446	57.4259	72.8033	42.6505
	GWR	96.2505	101.1540	114.5960	79.3157	92.7269	80.6858	88.1650	73.9109
	RFATPK	**6.3068**	**5.1617**	**6.6191**	**4.8033**	**5.6546**	**4.6276**	**3.4655**	**4.1491**
CC	Allocation	0.9157	0.9234	0.9189	0.9165	0.9094	0.9068	0.8953	0.9091
	ML with splines	0.9233	0.9214	0.9381	0.9241	0.9270	0.9245	0.8941	0.9325
	GWR	0.9095	0.9041	0.8882	0.9014	0.8832	0.8922	0.8702	0.8799
	RFATPK	**0.9943**	**0.9953**	**0.9938**	**0.9943**	**0.9932**	**0.9941**	**0.9952**	**0.9936**

3.4.1.2 Downscaling prediction (450 m to 100 m)

To facilitate visual comparison, three zoomed sub-areas selected randomly and their corresponding results are shown in Figure 3-5 and Figure 3-6 for Mumbai and New Delhi, respectively. The sub-areas include landscapes with a mix of dense and less dense urban structures. The disaggregating findings demonstrate that RFATPK renders those landscapes well. Due to poor prediction, the GWR approach distorts the borders, whereas Machine Learning with Splines excessively smooths the boundaries. When it comes to preserving spectral characteristics and recovering both dense and less dense textures, RFATPK performs satisfactorily.

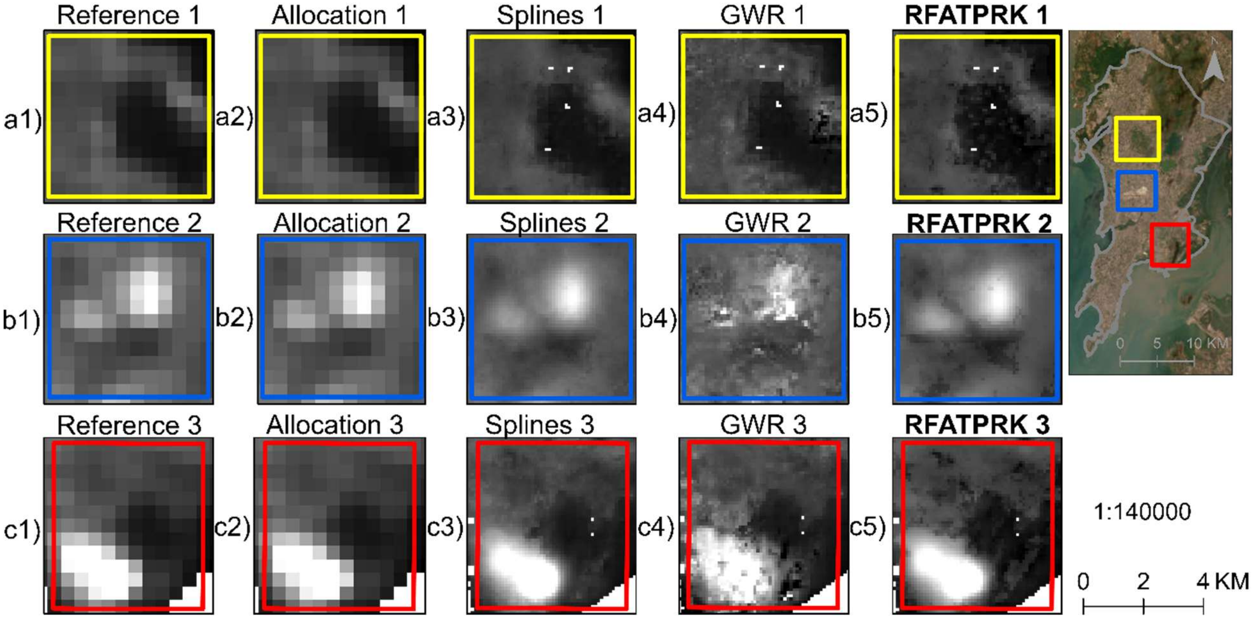

Figure 3-5: Downscaling visual results (100 m) in three sub-areas for Mumbai, 2018. From left to right: Raw NTL, Allocation-based, Machine Learning with Splines, GWR, **RFATPK**. Each column illustrates one of the three selected random areas. **Bold** shows the proposed method.

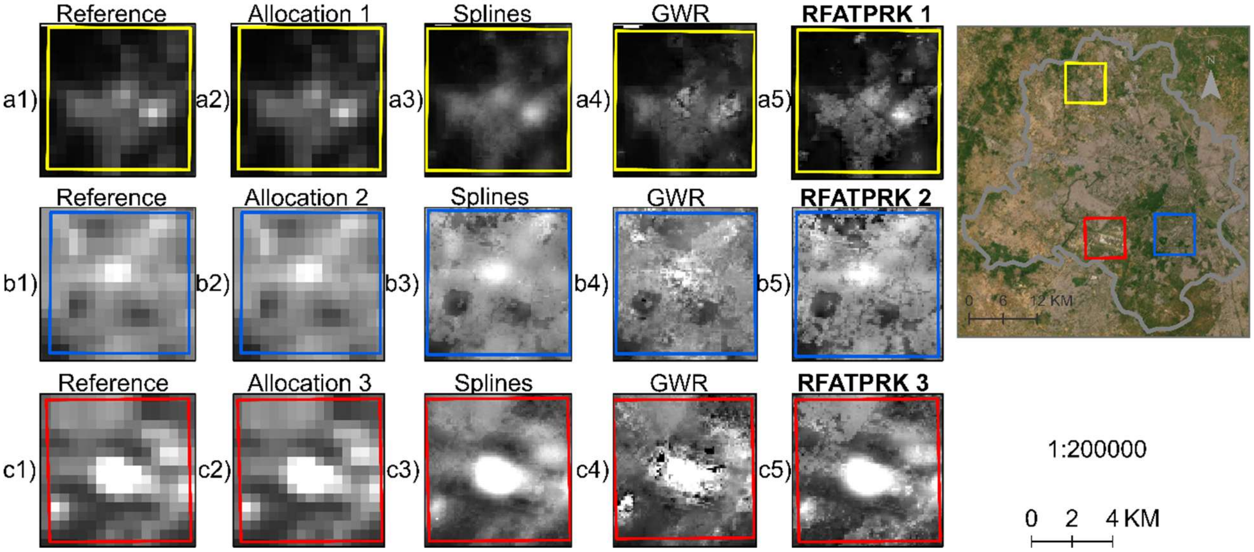

Figure 3-6: Downscaling visual results (100 m) in three sub-areas for New Delhi, 2018. From left to right: Raw NTL, Allocation-based, Machine Learning with Splines, GWR, **RFATPK**. Each column illustrates one of the three selected random areas. **Bold** shows the proposed method.

The variograms were compared for the different downscaling methods. Due to large volume of images produced regarding the comparison of the variograms for all the years, a single example for the year 2018 is shown for every region. Variograms were computed directly from the downscaled NTL images at 100 m resolution, as this approach allows direct comparison of the spatial variance introduced by each method. Larger semivariance values indicate greater reconstructed spatial variability, whereas smaller values reflect less reconstructed spatial variability. Compared to the other approaches, the Allocation-based downscaling method's variogram exhibited the highest semivariance (Figure 3-7). The GWR-based downscaling approach in Figure 3-8 provided the highest semivariance, while the Machine Learning with Splines-based downscaling method produced the lowest semivariance.

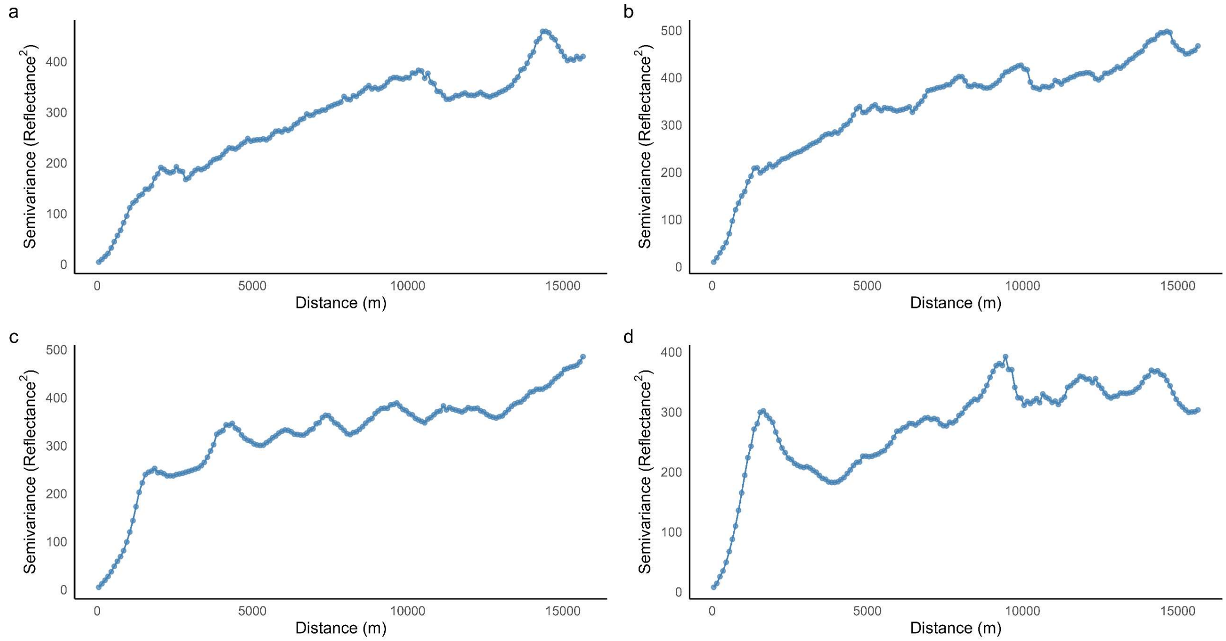

Figure 3-7: Variograms of the downscaling methods for Mumbai, 2018. a) Allocation-based prediction, b) Machine Learning with Splines-based prediction, c) GWR-based prediction and d) **RFATPK**-based prediction.

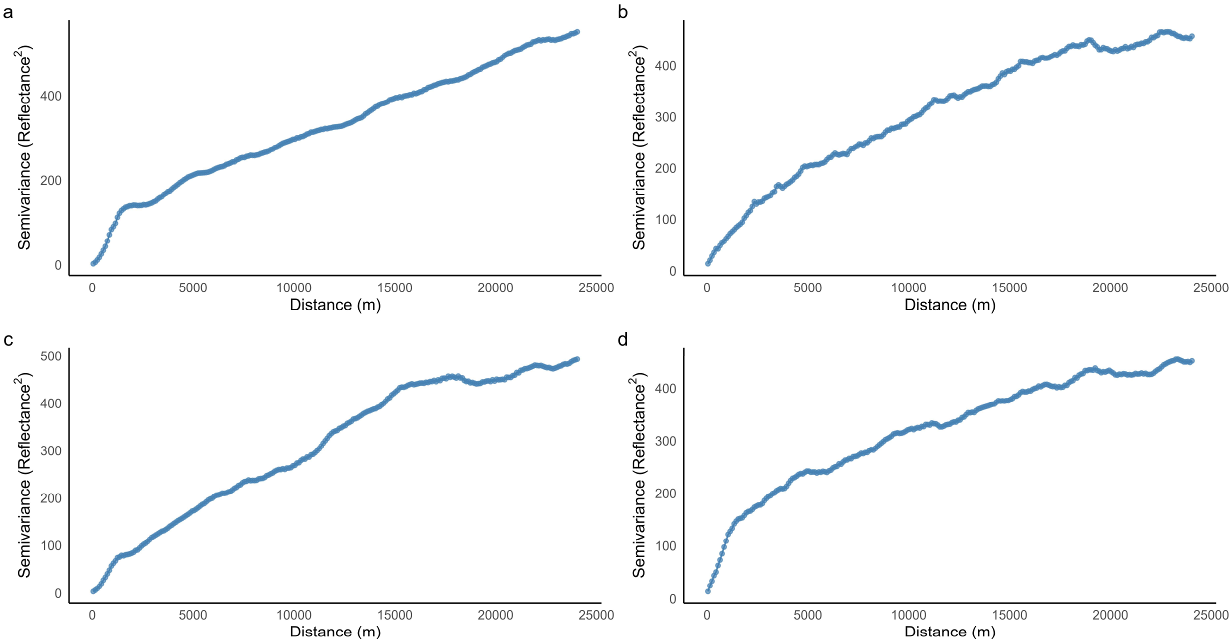

Figure 3-8: Variograms of the downscaling methods for New Delhi, 2018. a) Allocation-based prediction, b) Machine Learning with Splines-based prediction, c) GWR-based prediction and d) **RFATPK**-based prediction.

In comparison to GWR and Machine Learning with Splines, the suggested RFATPK generated the best visual outcome among the three downscaling techniques and also had the attribute of perfect coherence (Table 3-4). Allocation-based downscaling also preserves the property of perfect coherence, but no new information is added and there is, consequently, no spatial variability in the NTL intensity within the fine resolution pixels.

Table 3-4: Measurement of perfect coherence, of the four downscaling methods for Mumbai and New Delhi for all years under investigation. **Bold** shows the largest results in terms of coherence.

		2013	2014	2015	2016	2017	2018	2019	2020
Mumbai	Allocation	**0.9957**	0.9907	**0.9958**	**0.9958**	0.9950	**0.9954**	**0.9949**	0.9927
	ML with splines	0.9916	0.9869	0.9919	0.9917	0.9922	0.9925	0.9921	0.9897
	GWR	0.9756	0.9582	0.9797	0.9798	0.9784	0.9731	0.9744	0.9636
	RFATPK	0.9950	**0.9923**	0.9932	0.9935	**0.9987**	0.9923	0.9938	**0.9984**
New Delhi	Allocation	**0.9980**	**0.9994**	**0.9980**	**0.9979**	**0.9978**	**0.9979**	**0.9978**	**0.9979**
	ML with splines	0.9967	0.9967	0.9949	0.9964	0.9954	0.9948	0.9966	0.9946
	GWR	0.9943	0.9947	0.9877	0.9931	0.9857	0.9879	0.9856	0.9872
	RFATPK	0.9943	0.9953	0.9938	0.9943	0.9932	0.9941	0.9952	0.9936

According to Table 3-4, the property of perfect coherence was achieved in all years for both regions only for the RFATPK and Allocation-based methods. RFATPK had the highest Correlation Coefficient (CC) index for the years 2014, 2017 and 2020, while the Allocation-based method produced the maximum for the rest of the years, for Mumbai. For New Delhi, the Allocation method had the highest CC value for all years. In summary, the proposed method was the only one to achieve perfect coherence consistently throughout the years across all regions, despite the fact ML with Splines had higher values of CC for New Delhi compared to RFATPK. ML with Splines was inconsistent in achieving perfect coherence across the regions and for all years as can be seen for the year 2014 for Mumbai.

Table 3-5 and Table 3-6 show the quantitative comparison of each method with the Luojia used as a reference.

Table 3-5: Quantitative comparison of the downscaling approaches at 100 m for Mumbai, 2018 (reference is the Luojia). **Bold** shows the best results.

		Allocation	ML with splines	GWR	**RFATPK**
Mean	RMSE	13.9105	16.8635	15.7574	**13.8938**
	MSE	196.1515	286.4333	248.6675	**193.2563**
	PCC	0.6056	0.5274	0.5408	**0.6757**
StD	RMSE	1.8192	1.6027	0.6798	**0.5219**
	MSE	50.9233	54.305	21.4063	**14.7106**
	CC	0.0893	0.1044	0.0660	**0.0204**

Table 3-6: Quantitative comparison of the downscaling approaches at 100 m for New Delhi, 2018 (reference is the Luojia). **Bold** shows the best results.

		Allocation	ML with splines	GWR	**RFATPK**
Mean	RMSE	7.4432	7.7110	8.5856	**6.7488**
	MSE	55.4679	59.4932	73.7905	**45.8890**
	PCC	0.9268	0.9225	0.9062	**0.9392**
StD	RMSE	0.2868	**0.2044**	0.3108	0.6541
	MSE	4.2883	3.1429	5.4010	8.8968
	CC	0.0045	0.0048	**0.0045**	0.0068

It can be seen in Table 3-5 and Table 3-6 that the proposed method produced the smallest mean RMSE and mean MSE in each of the 50 iterations (2000 random samples in each iteration) as well as the largest mean correlation coefficient with Loujia. More specifically, the RFATPK method, for Mumbai, produced the smallest average RMSE of 13.8938 nWcm^{-2}sr^{-1}, while the other methods produced larger RMSEs, with the Machine Learning with Splines being the largest. The same is true for MSE, where RFATPK produced the smallest average MSE compared to the other three methods. Finally, the correlation coefficient was the largest for RFATPK, at 0.6757 for Mumbai. For New Delhi, again RFATPK produced the most precise predictions compared to the other approaches with mean RMSE, MSE and CC of 6.7488 nWcm^{-2}sr^{-1}, 45.8890 nWcm^{-2}sr^{-1} and 0.9392, respectively. Considering that the LouJia1-01 imagery is an external (unseen) validation dataset produced with different sensing characteristics than the NTL imagery and that the prediction is made at a four point fine-fold finer spatial resolution than the original data, this result can be considered promising for a range of applications.

3.4.2 Night Light Development Index

The index was calculated utilizing the coarse-resolution nighttime lights data ($NLDI_{coarse}$) and the disaggregated NTL ($NLDI_{fine}$). To validate the results, the values of the Human Development Index for New Delhi for the years 2013 to 2019 were acquired from the Global Data Lab website (https://globaldatalab.org/) (accessed 05/02/2023). The relationship between the NLDI and HDI is well established in literature. Hence, this index was selected for validation (Elvidge et al., 2012). Using the $NLDI_{coarse}$ the Pearson's correlation coefficient with the HDI was -0.35 while when using the $NLDI_{fine}$ the association with the HDI was -0.48. These results are impressive, indicating that the downscaled annual mean NTL data were more correlated with human development compared to the raw annual mean NTL data at 450 m.

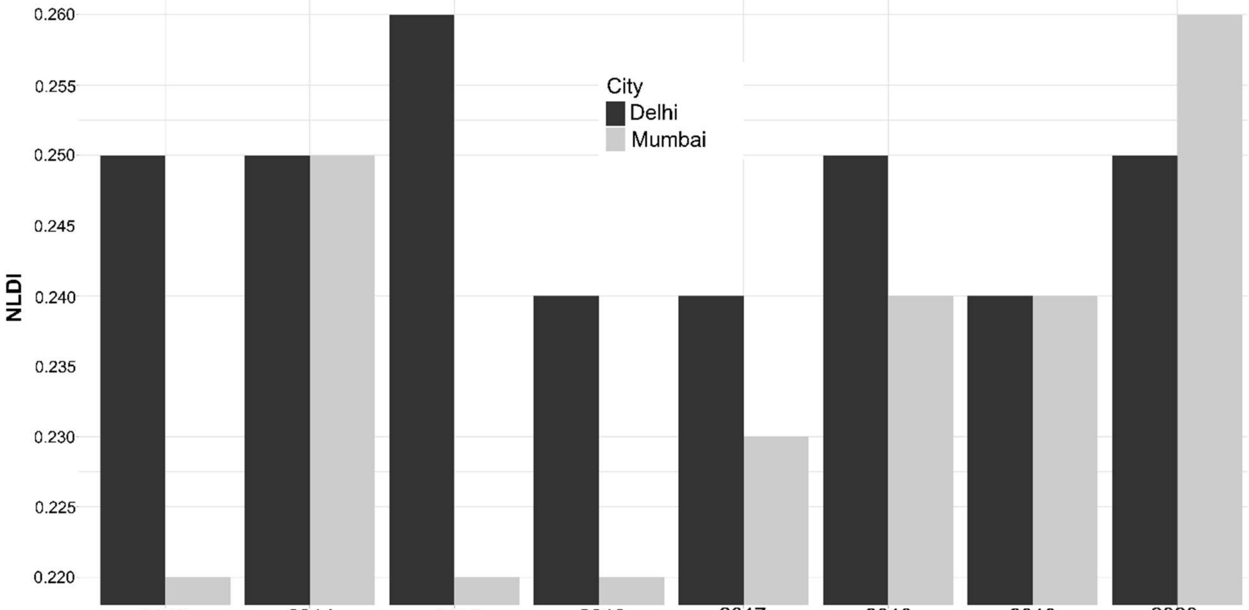

Figure 3-9: Night Light Development Index plotted through time for Mumbai (grey line) and New Delhi (dark grey line), based on single annual mean NTL images from 2013 to 2020.

Figure 3-9 illustrates the evolution of the NLDI for the period 2013-2020 for the cities of Mumbai and New Delhi. It can be seen that the index for Mumbai shows an upward trend which means that light inequality is increasing. On the contrary, the NLDI index for New Delhi is decreasing with the exception for 2015. The data are consistent with the HDI index from Global Data Lab which reveals an increase in the index through time (Table 3-7).

Table 3-7: The HDI and NLDI indexes for New Delhi.

Year	**HDI**	**NLDI**
2013	0.72	0.25
2014	0.73	0.25
2015	0.73	0.26
2016	0.73	0.24
2017	0.74	0.24
2018	0.74	0.25
2019	0.75	0.24

According to many authors, there is an inverse relationship between the two indices (Elvidge et al., 2012; Ghosh et al., 2013). There are no yearly measures of HDI for Mumbai to validate the results, but many newspapers highlighted the rise in inequality in this region (Bendix, 2018; Ashar, 2019).

3.4.3 Gross National Income *per capita*

Gross National Income (GNI) *per capita* for New Delhi (2013–2019) was compared against coarse-resolution (NTL_c) and fine-resolution (NTL_f) NTL using annual mean composite Sum of Lights (SOL) values. Both GNI (in 1,000 USD) and SOL values were logarithmically scaled. Table 3-8 presents the results of linear regressions between GNI and NTL, summarizing model fit (R^2), statistical significance (*p*-value), and confidence intervals (C.I.).

Table 3-8: The statistic results of the comparison of the linear model between Gross National Index *per capita* (GNI) and coarse-resolution NTL (NTL_c) and fine-resolution NTL (NTL_f). C.I. stands for Confidence Intervals. SOL values are derived from mean annual NTL composites.

Model	R^2	***p*-value**	**C.I.**	**Sample size**
GNI ~ NTL_c	0.5	0.084	-5.4 - 0.5	7
GNI ~ NTL_f	0.7	0.023	-5.4 - -0.6	7

The regression results indicate that NTL_f provides a substantially stronger and statistically robust predictor of GNI than NTL_c. While the regression of GNI on NTL_c explains 50% of the variance (R^2 = 0.50), this relationship is not statistically significant at the 5% level (p = 0.084). In contrast, NTL_f explains 70% of the variance in GNI (R^2 = 0.70) and yields a statistically significant association (p = 0.023). This represents a 20% increase in explained variance, demonstrating that

NTL_f data not only improve model fit, but also yield statistically reliable estimates of economic activity.

3.5 Discussion

3.5.1 Random Forest area-to-point regression Kriging (RFATPK)

RFATPK is analogous to the AATPRK reported by Wang et al., (2016a). However, a different non-stationary model was implemented in this study. The results show a notable improvement of the merged images both visually and quantitatively resulting from the adoption of the spatial non-stationary regression model, reflected in a correlation coefficient larger than 0.84 in the regression part for all months and cities, with the exception of Mumbai 2020. In RFATPK, residual sharpening was conducted by ATPK which considered a global method and it is different from the approach proposed by Pardo-Iguzquiza et al. (2011), who developed a local scheme for Kriging interpolation. For each coarse pixel in local ATPK interpolation, semivariogram deconvolution is used to parameterize the regression model and the Kriging weights are calculated. This requires a lot of computational power, especially for areas with many pixels. We instead used global ATPK, which does not require the same computational cost. Since RFATPK is an extension of ATPRK, it benefits from ATPRK's advantages as it takes into consideration both the size of the support and the spatial correlation. Additionally, it can accurately maintain the spectral characteristics of the original coarse data, as illustrated in Table 3-4. The experimental results showed that RFATPK predicted more accurately than the three benchmark techniques. The resulting residuals may differ significantly from region to region if the global regression model in ATPRK is unable to represent adequately the relationship between the coarse and fine images when the observed scene varies locally (i.e., requiring a spatially non-stationary method). Thus, the residuals produced by the local non-stationary regression model are likely to be more suited for subsequent manipulation using a stationary downscaling model. Another point of consideration is the scale effect. It is acknowledged that due to the scale effect there exists differences in the two downscaling processes, that is, from 2025 m to 450 m and from 450 m to 100 m spatial resolution (Zhou et al., 2016; Pu, 2021). The scaling effect in downscaling NTL from a coarse spatial resolution to a high spatial resolution is beyond the scope of this research.

3.5.2 RFATPK and benchmark comparison

When the area of interest is spatially heterogeneous, the RFATARK technique yields more precise predictions. Comparing the proposed RFATPK method against three other image fusion techniques (GWR from regression-based methods, machine learning with splines from hybrid-based techniques and allocation of raster value) is of great interest. Since all computations are undertaken independently in each coarse band, RFATPK is substantially faster than the hybrid technique since it needs to model only the auto-semivariogram for each low-resolution image. The Kriging system in Equation 6's matrices now have substantially smaller sizes. Consequently, RFATPK is more user-friendly and much simpler to automate. Although the regression-based method is similar to RFATPK, the latter has the appealing property of perfect coherence, which is inherent with ATPK. Compared to the simple allocation of raster values, the geostatistical solution preserved fairly accurate, both visually and quantitatively, the spatial patterns of NTL intensity, a property which simple allocation of raster values does not have. In conclusion, the suggested RFATPK method has the following features and benefits.

1. Regression modelling can employ fines-resolution predictors to lessen the uncertainty in spatial downscaling, improving the fused images visually and quantitatively;
2. RFATPK clearly takes into consideration the spatial (auto) correlation between the data and the size of the support (pixel) by inheriting the advantages of ATPRK;
3. RFATPK, can precisely preserve the spectral features;
4. Unlike machine learning with splines, which executes six regression models, RFATPK executes only one local model and incorporates a global method (ATPK), calculates the Kriging weights only one time for the entire region and uses considerably smaller matrices in the Kriging method; this makes it faster for downscaling images.

3.5.3 Use case studies

Monitoring socioeconomic indicators at the city-scale is of great importance for governments and policy makers. As such unbiased data at fine spatial resolution are a critical input to support policy development and decision-making. To highlight the applicability of the downscaling method, two socioeconomic applications were considered at the city-scale.

3.5.3.1 Night Light Development Index

The index is an estimation for economic and human development in a region. The relatively strong association between the NLDI and the HDI (Table 3-7) suggests the former index measures human development, which is consistent with Elvidge et al. (2012). The results using the fused NTL are encouraging and we suggest the downscaled data are suitable for measuring human development at the city-scale.

3.5.3.2 Gross National Income *per capita*

The reference NTL data were less accurate at predicting yearly GNI than the downscaled NTL at the city scale. The application of studies that demonstrate the efficiency of estimating such socioeconomic indicators at the city level is called into question by the poor association between coarse resolution nighttime lights data and GNI and makes it difficult to understand how such data may serve as a reliable indicator of changes in city-scale economic activity. The results provided here, on the other hand, point to the downscaled NTL as a far more accurate way to quantify GNI and a viable substitute for the index. The non-significant relationship for coarse-resolution NTL highlights the importance of fine-scale spatial detail in capturing economic variation within cities. Downscaling NTL via RFATPK not only increases R^2, but also produces statistically robust relationships, demonstrating that fine-resolution satellite sensor data better reflect intra-urban economic structure.

3.5.4 Future research

The point spread function (PSF) exists in every satellite sensor imagery. It has a significant impact on image quality and sets a strict cap on how much information is included in satellite sensor images (Wang et al., 2020). It is clear that the PSF can affect the downscaling process because disaggregating methods aim to increase the pixel size by creating more (sub-) pixels than the original image and thus, better describing the spatial content of a region. A variety of PSFs will be evaluated in a future effort to reduce the uncertainty in the downscaling procedure. Another important limitation is that NTL values cannot be determined from a single covariate, as shown by the global model. This means that, more ancillary variables are more suitable for charactering NTL intensity and may lead to more accurate prediction of the trend (Ye et al., 2021). Future research will focus on incorporating more ancillary variables, mainly from the so called 'social pixels', for example, geo-tagged Twitter data or geo-located POIs. Thus, fusion with social data at a fine resolution should be tested in future. Lastly, as mentioned in the Discussion, Section 5.1, this research did not take into account the scale effect. Therefore, studies in the future should need to be designed for and check if the by accounting for the scale effect will improve the downscaling predictions.

3.6 Conclusions

Spatial downscaling is widely used to transform remotely sensed images from coarse resolution to fine resolution in order to track human activity. For the first time, a strategy for spatially downscaling nighttime lights pictures was presented in this study using RF and ATPK. The RFATPK approach has the advantage of taking into consideration both the spatial correlation between the response variable and the predictors as well as local spatial variation. To show the effectiveness of this approach, it was used on yearly coarse NTL products in two separate Indian megacities.

The geostatistical RFATPK solution was compared against three benchmark algorithms in experiments conducted on one experimental case in the two mega-cities. The results are summarized as follows: 1) The three benchmark methods were outperformed by RFATPK, demonstrating the utility of this technique for spatial sharpening; 2) RFATPK, consistently, assures total coherence with the original coarse data, in contrast to two of the benchmarks, and 3) due to its spatially non-stationary nature, RFATPK was able to lower the residual variance in comparison to a single, global regression model. The encouraging results suggest that RFATPK can produce images that are suitable for socioeconomic analysis at the city-scale, as illustrated when comparing a human development index using coarse-resolution NTL data against fine-resolution nighttime lights. Indeed, the GNI index was better approximated using the downscaled NTL data. Another application suggesting that the disaggregated NTL are more suitable for fine scale (social) applications was the measurement of wellbeing by means of light inequality. The results implied that using the proposed solution, the nighttime lights satellite sensor data are closer to the values of the official statistics (i.e., HDI). According to the results, our method can be generalized worldwide (i.e., to other cities) and for a variety of social science applications.

Chapter 4 Downscaling satellite nighttime light imagery while addressing the blooming effect[2]

---

[2] This chapter is based on the published paper: Tziokas, N., Zhang, C., Tziokas, A., Wang, Q., Atkinson, P.M., 2024, Downscaling Satellite Nighttime Light Imagery While Addressing the Blooming Effect. JSTARS
IEEE Journal of Selected Topics in Applied Earth Observations and Remote Sensing, PP(99):1-18. 10.1109/JSTARS.2024.3429244.

Abstract

In the past 20 years, improvements in nighttime light (NTL) remote sensing have spurred a resurgence of interest in the mapping of human economic activity. Nevertheless, the full potential of NTL data for urban research is constrained by a relatively coarse spatial resolution and the blooming effect. Downscaling NTL data is a potential solution, aiming to obtain fine-resolution nighttime lights data with high accuracy. Most existing remotely sensed image fusion techniques were developed for optical remote sensing images taken during the day. When NTL images are compared to optical images, they exhibit a greater quantity of dark (low value) pixels, higher levels of background noise, and a more obvious blooming effect. In this paper, we proposed a spatially non-stationary, geostatistical-based downscaling technique (random forest area-to-point Kriging) to downscale NTL data while accounting explicitly for the point spread function, thus, dealing with the blooming effect specific to NTL data. We compared several image fusion algorithms for downscaling while reducing the blooming effect. Numerical experiments on two megacities showed that downscaling was improved both numerically and visually by taking the PSF into consideration. During the RF regression, the R^2 increased and the RMSE decreased for both study regions, when accounting for the PSF. For the ATPK-based residual part, considering the PSF led to increased accuracy of prediction. The suggested methodology has the potential to increase the detail and accuracy of the NTL data available for modeling socioeconomic phenomena at the city scale, with wide potential for application in future socioeconomic research.

Keywords - Downscaling; Point spread function; Random forest; area-to-point Kriging; Satellite nighttime light imagery; Urban remote sensing

4.1 Introduction

Nighttime light (NTL) remote sensing data are acknowledged widely as being human-oriented, indicating the distribution and intensity of human activities. This contrasts with the more common optical remote sensing data, such as from Landsat and Sentinel, which focus primarily on the natural environment (Levin et al., 2020). NTL remote sensing has gained significant interest due to its ability to bridge the gap between socioeconomic activity and the benefits of remote sensing data (standardization, repeat measurement, complete coverage). It is frequently utilized to derive objective and third-party socioeconomic indicators, such as on poverty (Jean et al., 2016), populations (Stathakis and Baltas, 2018), urban built-up areas (Ye et al., 2021), GDP and energy consumption (Zheng et al., 2023). Urban areas, where economic activity tends to concentrate, are ideal places to study with the aim of addressing human-oriented issues such as sustainable development.

The Visible Infrared Imaging Radiometer Suite (VIIRS) Day/Night Band (DNB) is one of the most utilized sources of NTL data (Feng et al., 2020). VIIRS offers fine temporal resolution (daily, monthly and yearly images), on-board calibration and the avoidance of saturated pixels, and it is free to acquire. In comparison, alternative NTL satellite products such as Luojia, Jinlin and DMSP-OLS, which have the advantages of either a finer spatial resolution or they extend further back in time, are commonly commercial products and expensive to purchase (Abascal et al., 2023). Notwithstanding the advantages of VIIRS, the utility of the data for scientific and practical applications is limited because of their ~500 m spatial resolution. Elvidge et al. (Elvidge et al.,

2007) stated that a minimum spatial resolution of ~100 m should be used in urban related applications. This has led to issues (such as low accuracy and small correlation) when utilizing NTL imagery for mapping populations, built-up areas and economic indicators (Feng et al., 2020). Moreover, nighttime imaging has the blooming (or overglow) effect, in which light from bright sources spreads into neighboring pixels, creating an overestimation of brightness in surrounding areas; this is equivalent to a large point spread function (PSF).

Downscaling is the term used to describe a reduction in the pixel size of remotely sensed images in the context of remote sensing (Atkinson, 2013). Downscaling has been undertaken using many methodologies and strategies, essentially aiming to increase the information richness of the downscaled images. Area-to-point Kriging (ATPK) is one such method (Kyriakidis, 2004). It has the advantage of absolute coherence, which means that when the downscaled image is upscaled to the original coarse spatial resolution the results are identical. By including a (global) regression term, Wang et al. (2016a) expanded ATPK and called it area-to-point regression Kriging (ATPRK). In ATPRK, covariates at a finer spatial resolution are employed in a (linear) regression model to predict the response variable. Then, the regression model's residuals are downscaled using ATPK. More recently, alternative regression methods have been used in the ATPRK model; nonetheless, the majority of the current algorithms for fusing remote sensing images are designed to fuse optical remote sensing images taken during the day. When NTL images are compared to optical remote sensing, they exhibit a greater quantity of dark pixels (low values) and more background noise (H. Li et al., 2024; Tziokas et al., 2023). Consequently, it is of great interest to confirm the efficacy of conventional ATPK-based optical remote sensing techniques for VIIRS image downscaling.

Sufficiently large correlations between NTL and biophysical and/or socioeconomic covariates at a finer spatial resolution are required for multivariate downscaling. Population data, spectral indices and transport network data are examples. Regression models are fitted between the NTL data and aggregated (coarse resolution) covariates and then used with the fine-resolution covariates as inputs to predict NTL at the fine pixel size. According to Ye et al. (2021) and Liu et al. (2022), there is often a non-linear relationship between NTL and its covariates, which may render global models unsuitable. The capacity of machine learning (ML) algorithms to capture non-linear relations between NTL and fine-resolution covariates has been demonstrated recently (Guo et al., 2023; Liu et al., 2022; Tziokas et al., 2023; Ye et al., 2021). With several independent factors, deep neural network (DNN) and RF algorithms produced accurate predictions among the benchmarked techniques.

The point spread function (PSF) effect is widely seen in NTL remote sensing images (Zheng et al., 2020). It denotes that the signal for a certain pixel is the weighted sum of the contribution from its surrounding and internal pixels. This leads to a basic constraint on the information content of remote sensing images. Both the across-track and along-track directions are taken into consideration by the two-dimensional PSF function (Wang et al., 2020). The instrument's optics, the detector, the electronics, atmospheric influences, and picture resampling are the primary causes of the PSF effect (Cao et al., 2019). In places that are homogenous, the PSF effect might not be a major concern, but in diverse landscapes where mixed pixels predominate, it is essential. To the best of our knowledge, the PSF impact in NTL downscaling has not been studied yet. Therefore, searching for practical ways to lessen the PSF impact in NTL downscaling could provide guidance and potentially increase the accuracy for prediction.

In downscaling, the PSF of interest is not the measurement PSF, but rather the transfer function between images at the original coarse and target fine spatial resolutions (Wang et al., 2020). The transfer function is different subtly to the measurement PSF. It is equivalent to the difference in convolution between the two PSFs used for measurement (Wang et al., 2020). In the multi-variate scenario, additional data covering the same scene at the desired fine spatial resolution are available, despite the data being collected using several sensors or at different wavelengths. An important source of information for calculating the effective transformation PSF is the relationship between the coarse and fine resolution data. Research has established several approaches for PSF estimation (Wang et al., 2020). However, the techniques were designed primarily for optical remote sensing. Solutions need to be identified that can both estimate the PSF for NTL data and work well in scenarios involving several fine covariates.

The major contributions of this paper include:

1. Random forest area-to-point Kriging (RFATPK) was demonstrated for downscaling NTL continua while reducing the PSF effect (multivariate case) and producing more accurate downscaling NTL predictions.
2. An existing solution was applied to estimate the effective transformation PSF for the multi-variate case of NTL downscaling. The solution estimates the PSF for the NTL band and is also suitable for dealing with multiple fine bands.
3. The proposed solution was applied in two case studies with different dominant land uses and different climate profiles to provide important guidance for their use in future applications.

The remainder of this paper is divided into four parts as follows. The concepts of RFATPK are introduced in Sections 4.3.2, followed by the method of transformation PSF estimation. Section 4.4 presents the findings of the experiments conducted on two megacities. The results and associated problems are covered in Section 4.5, along with potential directions for future study. Section 4.6 draws conclusions of the paper.

4.2 Study area and datasets

4.2.1 Study areas

Case study 1: New Delhi, the capital of India, is situated along the Aravalli range, with Yamuna in the center and the Ganga River on its eastern border. New Delhi has a semi-arid climate. It is a major international center and a highly populated metropolis on the Asian subcontinent, being home to over 16 million people (~10,400 people per km^2). Compared to the national average of 31.16%, 93% of the population lives in urban areas, indicating the city's fast industrialization and urbanization (Malik et al., 2022; Naikoo et al., 2020).

Case study 2: As one of the largest metropolitan regions worldwide, the Los Angeles (LA) metropolitan area is the second largest in the USA. The U.S. Office of Management and Budget defines the Metropolitan Statistical Area (MSA) as the combination of Los Angeles and Orange counties, with a population of 9,819 million and a land area of 12,562 km² (Gurney et al., 2019). Because single-family detached homes are so common, the LA metropolitan region has a high degree of urbanization, a low population density, and fragmented retail centers that depend on intricate road networks (Hulley et al., 2019). Based on income, LA is classified by the World Bank as a high-income megacity (Rubinton and Isaacson, 2023). The two study regions are shown in Figure 4-1. To demonstrate the methods more clearly in this paper we used subsets of the two megacities as the study regions.

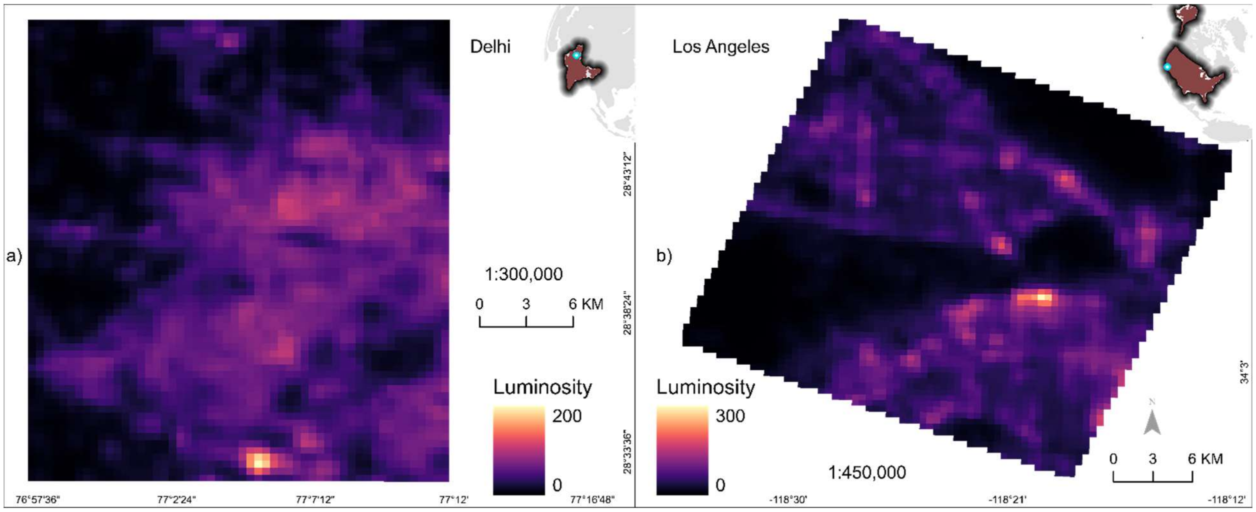

Figure 4-1: The VNP46A3 NTL image for a) New Delhi and b) Los Angeles (LA). The darker colors indicate areas with no NTL luminosity while the brighter colors indicate areas with higher NTL luminosity.

4.2.2 Datasets

Multiple sources of data were used in this research.

Table 4-1: Spatial datasets used in nighttime lights mapping and downscaling for New Delhi and Los Angeles. WorldPop was utilized for New Delhi whereas LandScan for Los Angeles. For the calculated spectral indices, refer to Appendix Table A-1.

Dataset	**Spatial resolution (m)**	**Year**	**Data source**
VNP46A3	~ 500	Monthly	(Marty and Stefanini Vicente, 2025)
WorldPop (constrained)	~100	2015 - 2020	(Tatem, 2017)
LandScan Pop (night)	~ 100	2015 - 2020	("ORNL LandScan Viewer - Oak Ridge National Laboratory," n.d., accessed on June 10, 2023)
Average building height (AGBH)	~ 100	2018	(Pesaresi et al., 2024)
Building volume (GHV)	~ 100	2015, 2020	
Surface (GHS)	~100, ~10, ~100	2015, 2018, 2020	
Mean Landsat 8 spectral indices (Appendix Table A-1) and TIRS	~ 30	Monthly	(Gorelick et al., 2017)
Road network	Vector layer	2015 - 2020	("Geofabrik Download Server," n.d., accessed on June 10, 2023)
Human footprint (HFP)	~ 100	2016 - 2020	(Williams et al., 2020)
Digital Surface Model (DSM)	~ 90	2015 - 2020	(Agency, 2024, accessed on June 10, 2023.
Luojia	130	2018	http://59.175.109.173:8888/index_en.html (accessed June 10, 2023)

4.3 Methodology

The proposed methodology is shown in Figure 4-2 as a sequence of actions intended to achieve the study goals. For downscaling without accounting for the PSF, the target variable and covariates were chosen first, and the covariates were upscaled to match the spatial resolution of the target variable (NTL). The residuals were then extracted as the difference between the RF regression model predictions and the observations. Third, ATPK was used to downscale the RF model residuals. Finally, the NTL raster layer with a spatial resolution of 130 m was created by combining the model prediction with the downscaled residuals.

To estimate the PSF (more specifically transfer function) of the NTL data the following steps were taken:

1. All fine spatial resolution covariates were convolved with a Gaussian PSF (with scale parameter σ_i) and spatially aggregated using a mean function to the coarse spatial resolution of the reference NTL.
2. For the NTL band, a RF regression model was fitted between the multiple aggregated covariates and the observed coarse image (e.g., the NTL). The R^2 was calculated.
3. Step 2 was conducted for all parameter candidates of σ (from 0.3 to 2 standard deviations * the pixel size, with step 0.1). For the visited coarse band, the optimal σ was estimated as the one leading to the largest R^2 in step 2.

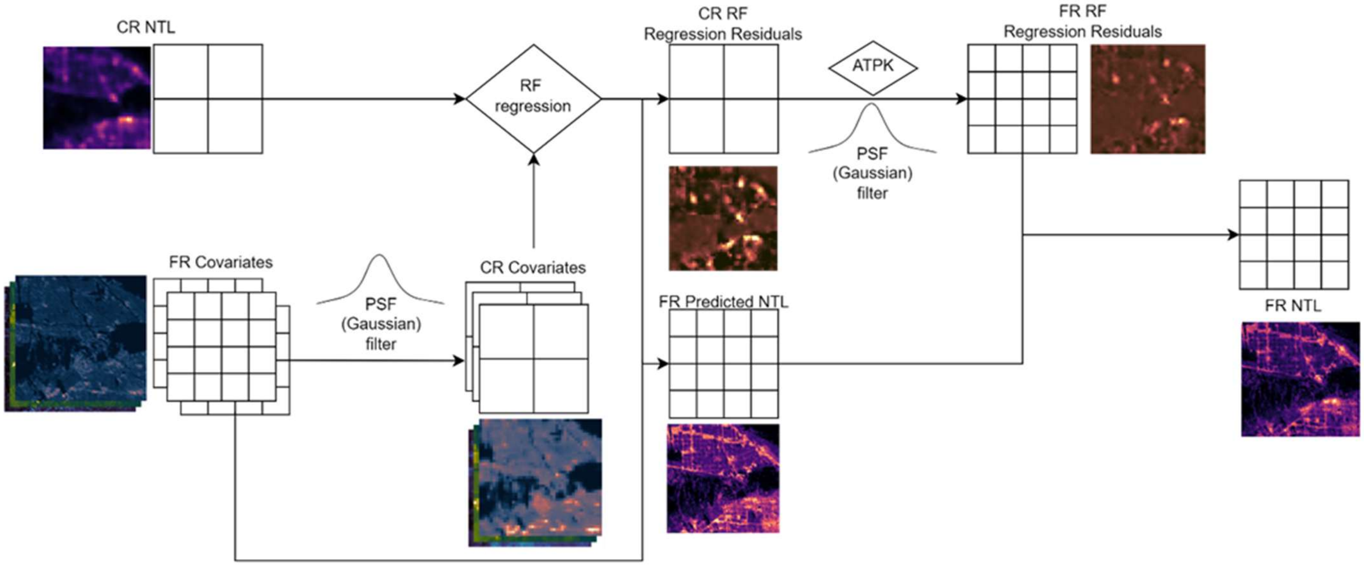

Figure 4-2: The methodology for applying RFATPK for downscaling NTL imagery. The acronyms CR and FR represent coarse resolution and fine resolution, respectively.

4.3.1 Preprocessing of spatial data

All data were re-projected to the EPSG:7760 and EPSG:3309 reference systems, for New Delhi and LA, respectively. We removed tunnels from the provided road network vector data as we hypothesized that no light inside a tunnel can be detected from the sensor (Wu et al., 2021). Moreover, using a brute-force approach, we searched all the possible combinations of road classes and found the optimal one that maximizes the correlation with the NTL. Then, we rasterized the data using a 130 m-by-130 m pixel size raster.

Because the Luojia satellite imagery has a similar spectral range to the NPP-VIIRS NTL, it was used to validate the downscaled NTL data. Then, Luojia imagery was, first, georeferenced using

30 carefully selected control points throughout each study region. The images were then re-projected to each of the projection systems, contingent upon the study region, and resampled using the spatial average to 130 m (Liu and Li, 2023). The following equation was then used to convert the image DN to radiance values, based on laboratory calibration data from the satellite data website:

$$r = \mathrm{DN}^{3/2} \cdot 10^{-10} \cdot w \qquad (1)$$

where w is the bandwidth, measured in $\mathrm{Wm^{-2}sr^{-1}}$, DN is the digital number acquired by Luojia, and r is the radiance value. Since Luojia's radiometric range is 0.46-0.98 µm, w equals 0.52 µm.

The following data pre-processing procedures were applied to the monthly NTL product: (1) cloud removal and (2) outlier detection. In line with the cloud quality flag, we filtered the NTL radiance to retain only pixels with no cloud or cloud shadow detected. Moon illumination fractions were corrected, and anomalous pixels were examined using DNB quality flags once the clouds were cleared.

In this research, we used a variable selection approach to exclude covariates with low prediction power, even though RF can handle uncorrelated covariates with the response variable. This was accomplished using the R (R Core Team, 2025) package *VSURF* (Genuer et al., 2015). It involves a two-step process where the variable selection procedure begins by ranking variables using raw variable importance (VI) scores obtained from repeated random forests and those exhibiting low importance across these repetitions are eliminated. This data-driven criterion, avoids reliance on normalized VI scores or assumptions of normality, ensuring robustness and reproducibility across varying model configurations. Second, a final subset is obtained by adding the sorted variables one after the other to the regression model. For further information, interested readers may consult Genuer et al. (2015).

4.3.2 RFATPK

Because global regression models, such as the one used in ATPRK, makes the assumption that parameters are geographically invariant, it cannot fit relationships locally. Furthermore, it is possible that the global regression residual does not satisfy stationarity requirements (e.g., second-order stationarity), which would complicate the Kriging interpolation. The Random Forest (RF) is a non-parametric ensemble learning approach with high accuracy and resilience to multicollinearity, that was developed from the bagging algorithm (Xu et al., 2020). Using a nonlinear regression model, the RFATPK approach considers both the geographical non-stationarity of the calculated residual NTL and the nonlinear correlation between NTL and the covariates. RFATPK formulation consists of a trend component as well as a regression residual component.

In the RFATPK technique, a regression model based on RF and independent variables at the coarse resolution is used initially to predict the geographic trend of NTL at the fine resolution. Next, a fine-scale prediction of the residual NTL is obtained by downscaling the coarse residual NTL using ATPK.

4.3.2.1 RF to estimate the spatial trend

Due to its high accuracy and low risk of overfitting, RF has been used frequently in regression tasks (Hutengs and Vohland, 2016). A random vector generated separately and uniformly for every tree in the forest determines the values of each tree in a RF, which is a mixture of uncorrelated decision regression tree covariates. The RF regression approach was used in this research to increase the spatial resolution of NTL from 430 m to 130 m. Based on the nonlinear connection between the covariates calculated at 130 m spatial resolution from a variety of environmental and socioeconomic determinants, the original NTL data were downscaled. Following Wang et al. (2020) the 130 m spatial trend of NTL was predicted using the RF-based regression method which is summarized as follows:

Initially, we applied a Gaussian filter to the covariates and then we spatially averaged them to match the NTL resolution. The filter's standard deviation ranged from 0.3 to 2 times the size of the coarse pixel, with a step of 0.1.

The RF regression approach, which can be stated using the following equation, was used to create the multivariate nonlinear regression model between the coarse NTL and the aggregated covariates:

$$\hat{Z}^{l}_{\text{Regression}}(x_0) = \mathrm{RF}(\boldsymbol{Z}K_1, \boldsymbol{Z}K_2, \dots, \boldsymbol{Z}K_l) + \boldsymbol{R} \tag{2}$$

The function $\mathrm{RF}(\cdot)$ represents the multivariate nonlinear regression algorithm between NTL and the K covariates (showed in Table 4-2, depending on the megacity) constructed with the RF regression model and $\boldsymbol{R}$ are the coarse-resolution regression residuals. $\boldsymbol{Z}K_l$ is the coarse covariate produced by upscaling the corresponding fine resolution covariate (or spectral band) k using a PSF:

$$\boldsymbol{Z}k_l = \boldsymbol{Z}k_l * h_k \tag{3}$$

where h_k designates the transformation PSF between the fine and coarse resolution covariates. The RF algorithm was implemented using the R (R Core Team, 2025) package, *ranger* (Wright and Ziegler, 2017).

Two-thirds of the covariates for each tree in the model were chosen as training samples using a bootstrap-based sampling technique to build the RF-based function approximation model. For each bootstrap-based sampling procedure, the remaining one-third of the inputs served as out-of-bag (OOB) data, meaning they were not used in the training process (Hu et al., 2020). An important parameter is the number of regression trees (*ntree*) in the forest. As the number of trees increases, Oshiro et al. (Oshiro et al., 2012) claim that the model's performance eventually reaches a breaking point. Thus, the moment the OOB error reached its minimum, we stopped adding extra regression trees (Hutengs and Vohland, 2016). In addition, the splitting rule played an important role in accuracy improvement, and an appropriate significance threshold to allow splitting had to be found (Borup et al., 2023). The RF-based nonlinear regression model in Eq. 2 can receive the 130 m independent variables as direct input. Next, it is possible to compute the NTL's downscaled spatial trend at a resolution of 130 m.

4.3.2.2 ATPK for downscaling residuals

In the next step of RFATPK, the coarse-resolution residuals $\boldsymbol{R}$ yielded in the regression model in the initial step are sharpened to a fine resolution using the ATPK algorithm:

$$\hat{Z}^{l}_{Residuals}(x_0) = \sum_{i=1}^{N} \lambda_i \, \boldsymbol{R}(x_i), \text{s.t.} \sum_{i=1}^{N} \lambda_i = 1 \tag{4}$$

where $\boldsymbol{R}(x_i)$ is the residual for the ith neighbor. The weights are calculated according to the Kriging matrix:

$$\begin{bmatrix} \boldsymbol{\gamma}_{\mathrm{CC}} & \mathbf{1}^{T} \\ \mathbf{1} & 0 \end{bmatrix} \begin{bmatrix} \boldsymbol{\lambda} \\ \theta \end{bmatrix} = \begin{bmatrix} \boldsymbol{\gamma}_{\mathrm{FC}} \\ 1 \end{bmatrix} \tag{5}$$

where $\boldsymbol{\gamma}_{\mathrm{CC}} = [\gamma_{\mathrm{CC}}(\mathbf{s}_{ij}), i = 1, \ldots, N, j = 1, \ldots, N]$ is an $N \times N$ matrix of coarse-to-coarse semivariances between the coarse resolution pixels centered at $\mathbf{x}_i$ and $\mathbf{x}_j$ ($\mathbf{s}$ is the Euclidean distance between the centroids of any random two pixels), $\boldsymbol{\gamma}_{\mathrm{FC}} = [\gamma_{\mathrm{FC}}(\mathbf{s}_{0i}), i = 1, \ldots, N]^{T}$ is an $N \times 1$ vector of fine-to-coarse semivariances between the fine and coarse resolution pixels centered at $\mathbf{x}_0$ and $\mathbf{x}_i$, $\boldsymbol{\lambda} = [\lambda_i, i = 1, \ldots, N]^{T}$ is an $N \times 1$ vector of weights for the N coarse resolution neighbors, $\mathbf{1}$ is a $1 \times N$ vector of ones, and θ denotes the Lagrange multiplier (Wang et al., 2020).

Assume that h_k is the PSF utilized for transforming the fine-resolution covariates to the coarse spatial resolution. The semivariograms $\gamma_{\mathrm{FC}}(\mathbf{s})$ and $\gamma_{\mathrm{CC}}(\mathbf{s})$ used in Eq. 5 are computed by convolving the fine-to-fine semivariogram (represented as $\gamma_{\mathrm{FF}}(\mathbf{s})$) between any two fine resolution pixels. The $\gamma_{\mathrm{FF}}(\mathbf{s})$, $\gamma_{\mathrm{FC}}(s)$ and $\gamma_{\mathrm{CC}}(\mathbf{s})$ semivariograms are a function of the distance and direction vector $\mathbf{s}$ (which is called lag in the field of geostatistics), that is, they are influenced specifically by separation distance and direction and not by the specific locations of the pixels. Also, the semivariogram can be seen as a 2-D image centered at (0, 0), which is built from values in all directions and at multiple distances. In this sense, $\gamma_{\mathrm{FC}}(\mathbf{s})$ and $\gamma_{\mathrm{CC}}(\mathbf{s})$ are computed as:

$$\begin{aligned} \gamma_{\mathrm{FC}}(\mathbf{s}) &= \gamma_{\mathrm{FF}}(\mathbf{s}) * h_C(\mathbf{s}) = \int_{x \in V(\mathbf{s})} \gamma_{\mathrm{FF}}(\mathbf{x}) \cdot h_C(\mathbf{s} - \mathbf{x}) d\mathbf{x} \\ &= \sum_{x_1 = s_1 - w_1}^{s_1 + w_1} \sum_{x_2 = s_2 - w_2}^{s_2 + w_2} \gamma_{\mathrm{FF}}(x_1, x_2) \cdot h_C(s_1 - x_1, s_2 - x_2) \end{aligned} \tag{6}$$

$$\begin{aligned} \gamma_{\mathrm{CC}}(\mathbf{s}) &= \gamma_{\mathrm{FF}}(\mathbf{s}) * h_C(s) * h_C(-\mathbf{s}) = \gamma_{\mathrm{FC}}(\mathbf{s}) * h_C(-\mathbf{s}) \\ &= \int_{\mathbf{x} \in V(\mathbf{s})} \gamma_{\mathrm{FC}}(\mathbf{x}) \cdot h_C(\mathbf{x} - \mathbf{s}) d\mathbf{x} \\ &= \sum_{x_1 = s_1 - w_1}^{s_1 + w_1} \sum_{x_2 = s_2 - w_2}^{s_2 + w_2} \gamma_{\mathrm{FC}}(x_1, x_2) \cdot h_C(x_1 - s_1, x_2 - s_2) \end{aligned} \tag{7}$$

where * indicates the convolution operator, $V(\mathbf{s})$ is the spatial coverage (with an extent of $2w_1 + 1$ by $2w_2 + 1$ fine resolution pixels) of the PSF centered at point $\mathbf{s} = (s_1, s_2)$, and $\mathbf{x} = (x_1, x_2)$ is the center of the fine resolution pixel within coverage $V(\mathbf{s})$ in the 2-D semivariogram image: $\gamma_{FF}(\mathbf{s})$ or $\gamma_{FC}(\mathbf{s})$.

The fine-to-fine semivariogram $\gamma_{FF}(\mathbf{s})$ is unknown and it can be approximated by deconvolution of the areal semivariogram calculated from the original coarse spatial resolution image (Goovaerts, 2008; Pardo-Iguzquiza et al., 2011; Wang et al., 2015). The prime solution is determined as the one that, once convolved according to Eq. 7, is the same as the known areal semivariogram. It should be noted that here the corresponding semivariograms are of the residuals as in ATPRK, not of the original variable as in ATPK. Readers interested in a more in-depth discussion of the deconvolution methodology utilized in this research can be found in Wang et al. (2016a).

The benefit of ATPK, namely the perfect coherence property, which was illustrated theoretically by Wang et al. (2015), is carried over to RFATPK:

$$\hat{\mathbf{Z}}_F^l * h_C = \mathbf{Z}_C^l \tag{8}$$

The PSF effect is considered in both regression modeling (see Eq. 3) and ATPK-based residual downscaling. With respect to the former, different PSFs will result in different upscaled images $\boldsymbol{Z}_C^k$ and different regression models (i.e., different predictions from $\hat{\mathbf{Z}}_{\mathrm{Regression}}^l$). This means that, different residuals, $\mathbf{R}_C^l$, will be produced from the regression model conditional upon the choice of PSF. This will have a direct effect on the prediction of $\hat{Z}_{\mathrm{Residuals}}^l(\mathbf{x})$ in ATPK-based residual downscaling.

It is clear from the previously discussed downscaling approach utilizing RFATPK that the transformation PSF relating images at different resolutions to each other, rather than the PSF of the original measurements, plays a crucial role in modeling semivariograms at different spatial scales and should not be disregarded. It is crucial to ascertain the transformation PSF for downscaling in advance because it may not be known in real-world situations. Finding methods that approximate the appropriate transformation PSF for the multivariate scenario, while taking into account the availability of auxiliary data at the requisite fine spatial resolution, is a more feasible strategy.

4.3.2.3 PSF estimation

It is known that there always exists a statistical relation among different spectral bands covering the same region, and largely for spectral bands with similar wavelengths. It is hypothesized that the single coarse resolution image $\boldsymbol{ZK}_l$ can be defined as a linear combination of the set of bands $\boldsymbol{ZK}_l(k = 1, \ldots, K)$ created by upscaling the existing fine spatial resolution images $\boldsymbol{Zk}_l$ $(k = 1, \ldots, K)$ at other wavelengths:

$$\boldsymbol{ZK}_l = \sum_k a_k\,(\boldsymbol{Zk}_l * h_k) + \boldsymbol{\varepsilon} \tag{9}$$

As such, the best scale transformation PSF h_k for image (or spectral band) $\boldsymbol{ZK}$ can be determined as the one reducing the fitting error $\boldsymbol{\varepsilon}$:

$$\hat{h}_c^l = \underset{h_c^l}{argminf}\left(\mathbf{z}_c^l - \sum_k a_k(\boldsymbol{Zk}_l * h_k)\right) \tag{10}$$

where f is an operator for determining the fitting error and it is computed by the fitting regression model (e.g., the classical global linear regression model, RF regression, etc.). Each coarse band is assigned a distinctive optimal PSF h_k, which varies for the several coarse resolution bands.

4.3.3 Urban socioeconomic applications

A major application of NTL imagery is its use as a proxy measure with which to study socioeconomic disparities. Here, we use the sharpened NTL imagery as a proxy for such phenomena to illustrate the benefits of our proposed approach to downscaling NTL data.

Previous research has already highlighted the superiority of the downscaled NTL compared to coarse scale counterparts, to some extent (Tziokas et al., 2023). In this study, to further highlight the benefits of the geostatistical model, RFATPRK, we conducted experiments using two socioeconomic variables. These were (1) the Human Development Index (HDI) and (2) income, measured in \$1,000. More specifically, a linear regression model was fitted using socioeconomic variables and the (downscaled with and without a PSF) NTL data, and their coefficients of determination (R^2) were compared. In this section, the entire megacities were utilized, and the downscaling parameters were extracted from the model of the smaller regions, due to the fact that the smaller regions incorporate a mix of land uses.

Yearly data for the two indices for both megacities were acquired from the Global Data Lab website ((“Global Data Lab - Innovative Instruments for Turning Data into Knowledge,” n.d.), accessed September 10, 2023). Then, using the LC data and the built-up class as a mask, we removed the non-built-up areas from the NTL images. The reason for doing so is that the exclusion of non-residential areas can increase the accuracy of predicting of socioeconomic variables (Pérez-Sindín et al., 2021).

4.4 Results

4.4.1 Significance of the selected variables for the RF regression

Table 4-2 shows the variable importance derived from RF in two megacities. It is important to note that while this importance score provides a relative evaluation of the contributions of the input variables, it is not the same as the correlation coefficient. Different covariates were used for the two megacities, with some similarities.

Table 4-2: RF regression variable importance scores across all megacities. IMP (Imperviousness), MNDWI (Modified Normalized Difference Water Index), BRBA (Band Ratio for Built-up Area), BAEI (Built-up Area Extraction Index), AVG AREA (Average Area), POP (Population Count), AGBH (Average Global Building Height), GNDVI (Green Normalized Difference Vegetation Index), DSM (Digital Surface Model), GHS (Global Human Settlement), TIRS (Thermal Infrared).

City	**Covariates**							
LA	IMP	MNDWI	BRBA	BAEI	AVG AREA	POP		
	652.43	405.86	236.47	195.87	148.61	82.00		
New Delhi	AGBH	POP	BRBA	HFP	GNDVI	DSM	GHS	TIRS
	157.97	139.06	138.07	104.78	101.96	81.84	73.11	46.18

Across both city-specific models, built-up indices exhibit the highest variable importance scores, with the exception of MNDWI, indicating that built-environment predictors account for a substantial share of NTL variability within each model. This pattern is observed consistently in both Los Angeles and New Delhi.

In the LA model, population (POP) has the lowest importance score (82.00) among the predictors, while MNDWI and built-up indices (e.g., BRBA and BAEI) dominate the ranking. In the New Delhi model, average building height (AGBH) ranks as the most influential covariate, followed by built-up indices and additional predictors including HFP, GNDVI, DSM, GHS, and TIRS. Compared to LA, a broader set of variables contributes to NTL variation in the New Delhi model. Variable importance scores differ between the two city-specific models; however, these scores are reported for each model independently. The models were estimated separately, employ different sets of predictors, and use different population datasets. Accordingly, the reported importance rankings represent within-model, city-specific results rather than statistically tested differences between cities.

Because variable importance values depend on the composition and inter-correlation of input variables, the rankings should be interpreted as relative measures within each model.

4.4.2 Validation of the PSF approximation

The proposed technique was used to fuse monthly NTL composites from 2015 to 2020. The goal of this experiment was to fuse the fine resolution 130 m covariates with the monthly NTL images to downscale NTL to 130 m. For the NTL, the Gaussian PSF was used.

LA and New Delhi served as the research locations for validating the suggested geostatistical filter-based image enhancement technique. With this design, that is, two megacities located in different geographic regions with different climates, as well as different numbers of images used for creation of the monthly composite, it is possible to explore the different effects that these parameters (i.e., climate and number of images) have on the capability of the proposed method. The minimum number of clear pixels per monthly composite pixel was at least seven.

The RF regression model was evaluated quantitatively using the R^2, and the RFATPK-based downscaling strategy was evaluated using the root-mean-squared error (RMSE).

4.4.3 RF regression

Based on Wang et al. (2020), the Gaussian filter's ideal σ (standard deviation) is the one that produces the largest R^2 in the (RF) regression. The results for the cities of New Delhi and LA in 2018 as an example year are listed below.

Figure 4-3 illustrates the R^2 of the RF model plotted against PSF size (i.e., σ) for the megacities of New Delhi (plot a) and LA (plot b), respectively. RF could explain more than 96% of the variation in NTL intensity for New Delhi and more than 85% for LA.

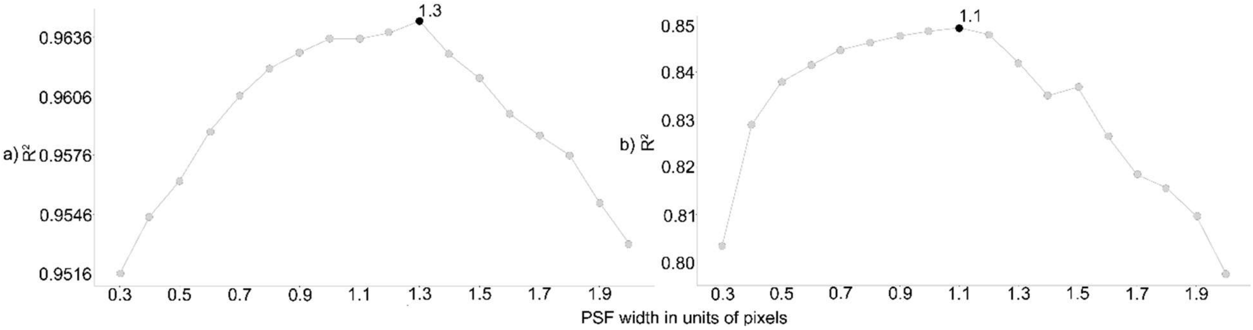

Figure 4-3: Plot of the RF R^2 (y-axis) against PSF width (x-axis). The PSF width that yielded the largest R^2 is plotted in black. a) R^2 for New Delhi, b) R^2 for LA.

The optimal parameter maximizing the R^2 was selected from the pool composed of 17 values (0.3, 0.4, …, and 2 coarse pixels). For LA, the largest R^2 value in the RF regression model was $\sigma = 1.1$ while for New Delhi it was $\sigma = 1.3$. The results indicate that after a certain value (1.1 and 1.3 coarse pixels) the larger the width of the PSF the smaller the R^2. The results are comparable to the work of Wang et al. (2020) where they downscaled day-time satellite sensor imagery and found similar behavior.

4.4.4 RFATPK results

Luojia NTL data were used to assess the PSF parameter estimation. The assessment was carried out using a two-step process. The preservation of spatial patterns in the downscaled NTL, the validation data (i.e., Luojia's NTL), and the original coarse resolution NTL data were first visually inspected and compared. After that, the downscaled NTL data were subjected to a Gaussian filter (with σ varying from 0.4 to 2), and the RMSE was computed using the validation data. This was done because, despite the validation data being regarded as "true" data (i.e., perfect data without errors) the measurement PSF effect also has a significant impact on Luojia's images (Bu et al., 2019). Figure 4-4 and Figure 4-5 for New Delhi and LA, respectively, demonstrate this, where it can be seen that the downscaled NTL images are clearly sharper than the Luojia reference images.

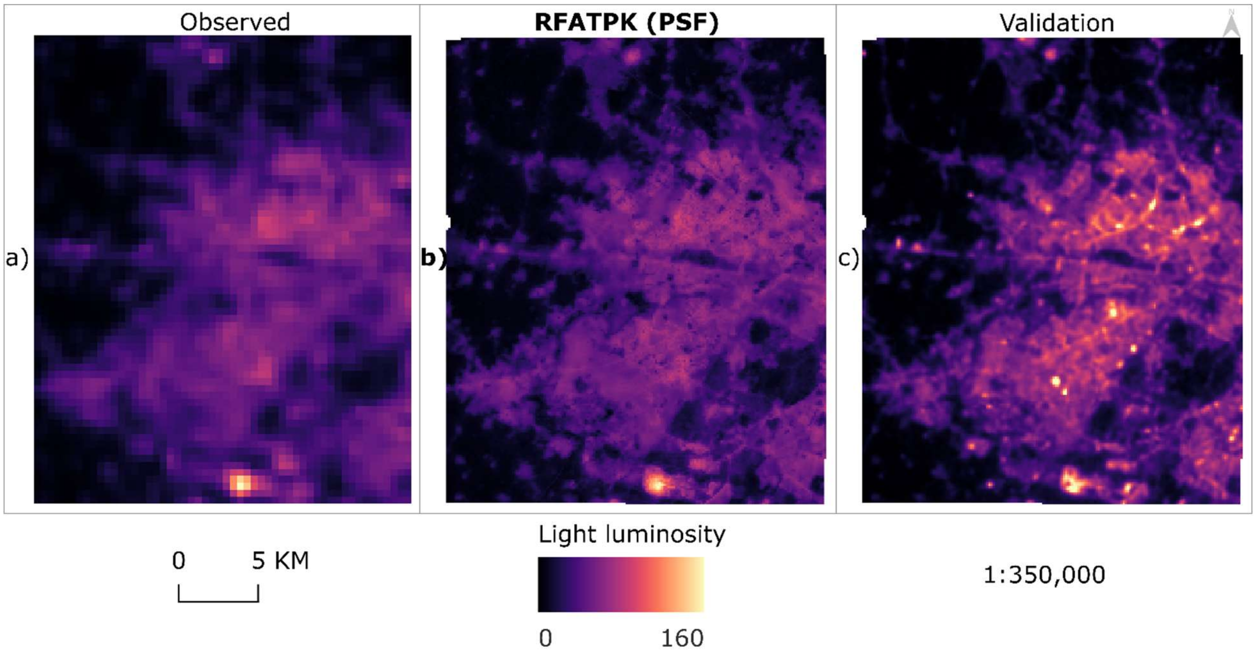

Figure 4-4: Downscaling results of the NTL imagery (New Delhi) using the selected PSF width (1.3 coarse pixel size). a) is the reference NTL image at the coarse spatial scale, b) is the downscaled NTL image, c) is the validation image, Luojia. **Bold** shows the proposed method.

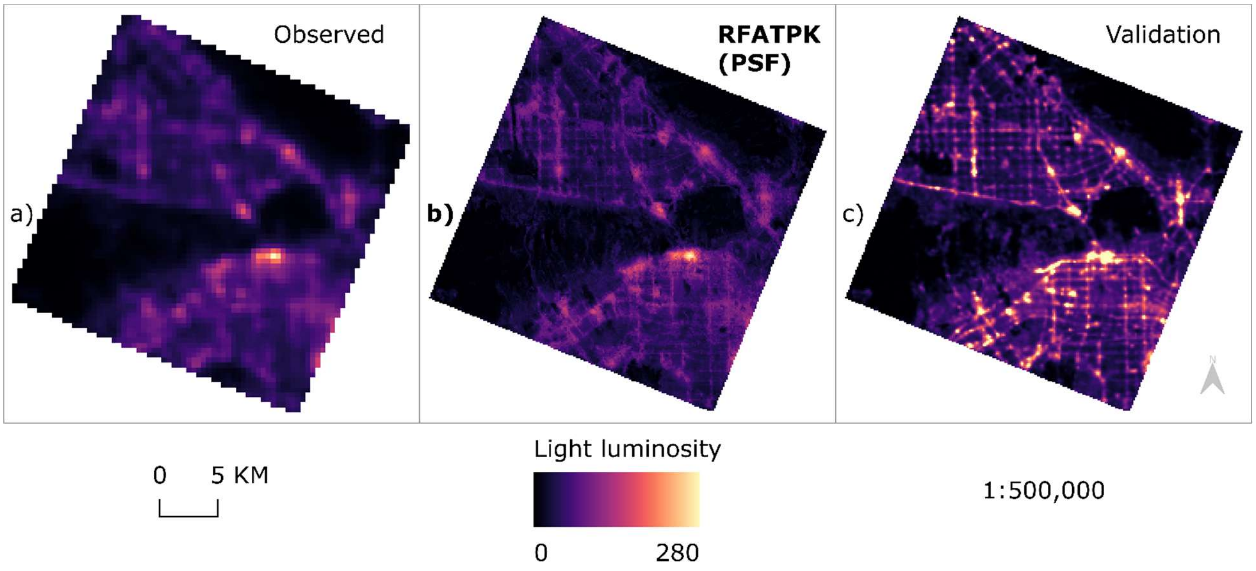

Figure 4-5: Downscaling results of the NTL imagery (LA) using the selected PSF width (1.1 coarse pixel size). a) is the reference NTL image at the coarse spatial scale, b) is the downscaled NTL image, c) is the validation image, Luojia. **Bold** shows the proposed method.

From Figure 4-4b and Figure 4-5b, the downscaling results can be compared to the reference NTL (a) and the validation NTL (c). In both megacities the predicted NTL captures the spatial variability of brightness reasonably well, and visually the results are more comparable to the validation NTL.

Moreover, the spatial structure of the study sites (e.g., road network) is well defined in the downscaled images and is even more obvious in the maps (b), compared to the validation data.

A highlight is the areas with high light intensity. For both megacities these areas represent the airport: for New Delhi this is located in the south part of the image (Figure 4-4 and Figure 4-6, (a)), while for LA the airport is in the west of the image (Figure 4-5 and Figure 4-7, (a)). The other bright spots in LA are dense road networks. In the downscaled images (maps (b) in Figure 4-5 and Figure 4-7) the bright spots were maintained, but their difference in brightness compared to other land uses is not as obvious as in the Luojia images. The results indicate that over complex terrains (i.e., different land uses) RF struggles to model the differences in brightness. The results are in line with other research downscaling land surface temperature data where similar behavior was observed (Ebrahimy et al., 2021).

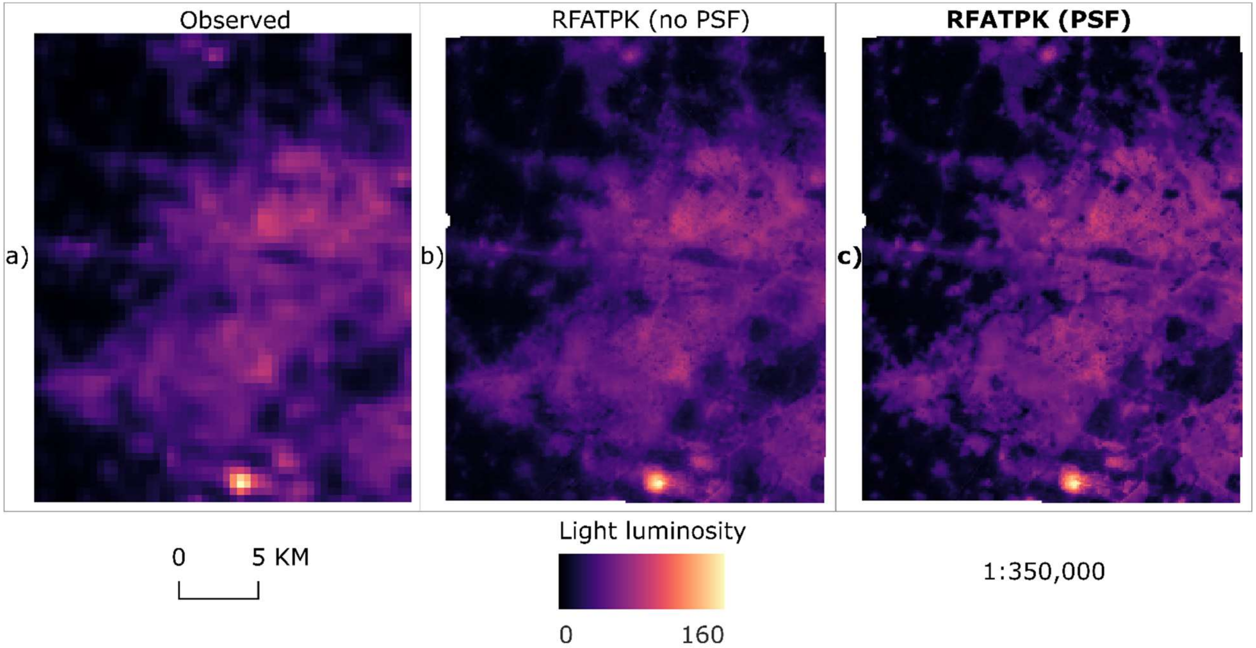

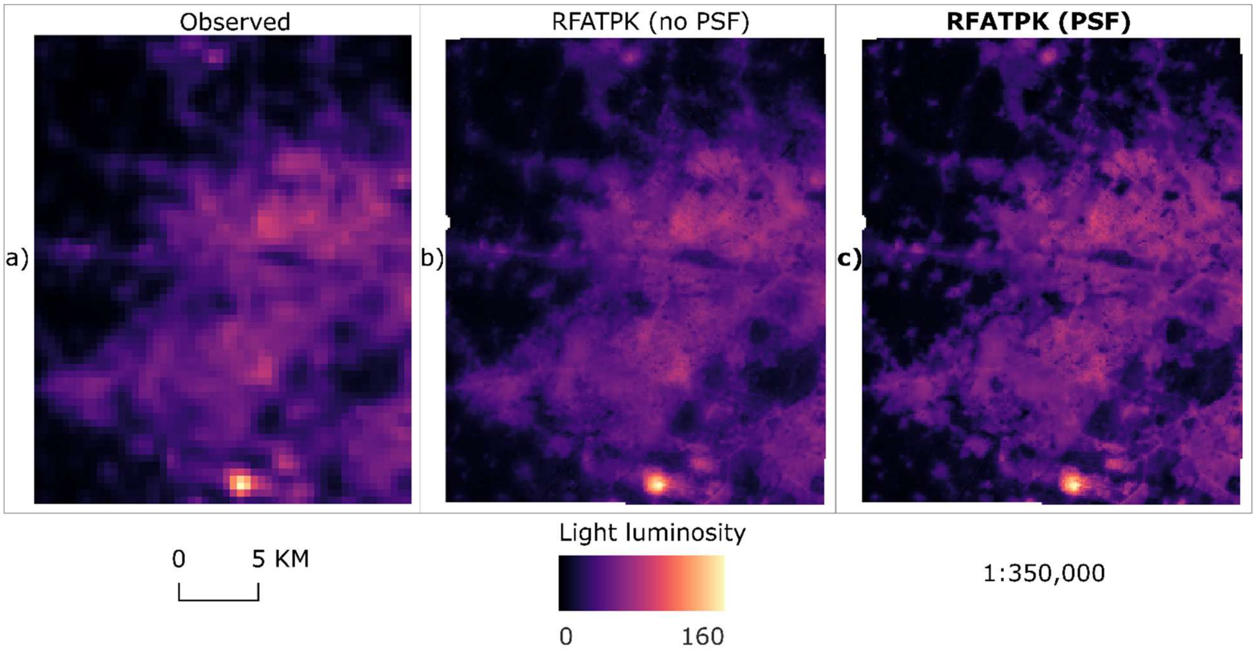

Figure 4-6 and Figure 4-7 illustrate the differences between the downscaled NTL images without accounting for the PSF and with the PSF for New Delhi (Figure 4-6) and LA (Figure 4-7), respectively.

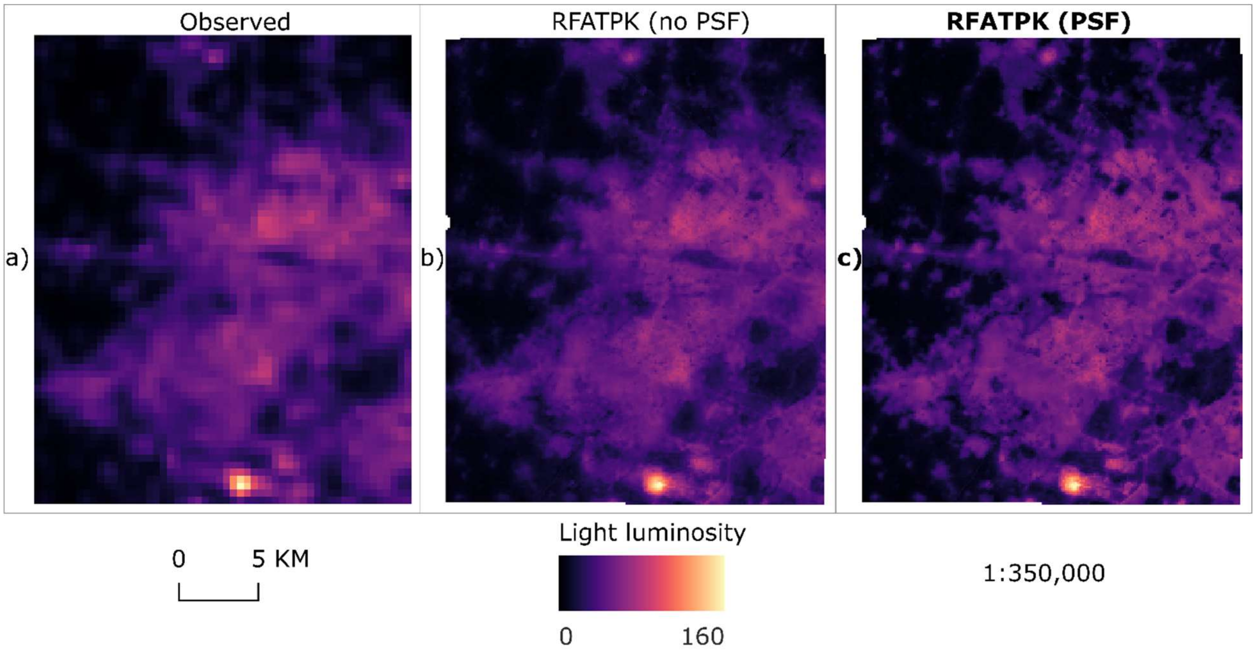

Figure 4-6: Downscaling results for the 130 m NTL image for New Delhi. (a) 430 m coarse image. (b) RFATPK with PSF. (c) RFATPK without PSF. **Bold** shows the proposed method.

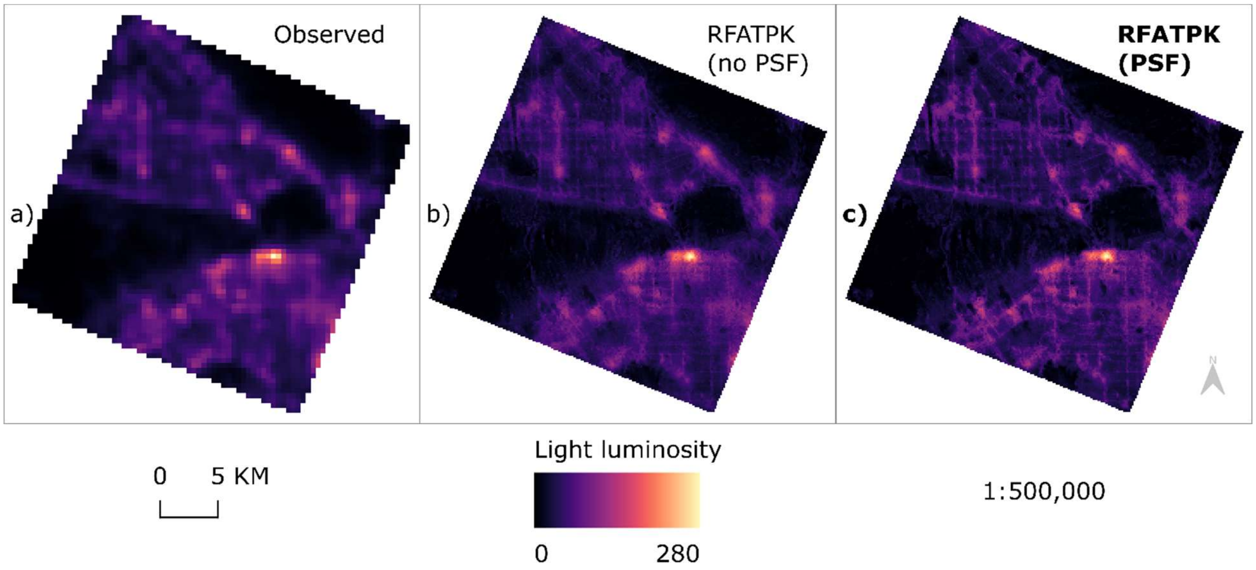

Figure 4-7: Downscaling results for the 130 m NTL image for LA. (a) 430 m coarse image. (b) RFATPK with PSF. (c) RFATPK without PSF. **Bold** shows the proposed method.

Predictions made with the PSF considered are visually much clearer than those made without it and shows more spatial information (such as the road network). Additionally, there is a greater contrast between parts that are lit and those that are not, indicating that the blooming effect has been lessened by taking the PSF into account.

Moreover, we provided the results without ATPK-based residual downscaling to further validate the effectiveness of RFATPK. The validation was done using Luojia images as reference.

Table 4-3: Comparison of the RFATPK and RF (without ATPK-based residual downscaling) methods using a Luojia image as reference. **Bold** indicates the best model.

Megacity	Method	Metric		Slope
		R^2	RMSE	
New Delhi	**RFATPK**	**0.94**	**9.92**	**1.42**
	RF	0.83	15.57	1.38
LA	**RFATPK**	**0.80**	**42.18**	**1.87**
	RF	0.70	50.26	1.81

As shown in Table 4-3, the predictions of both mega-regions are more accurate when considering ATPK-based residual downscaling in terms of R^2 and RMSE. More specifically, the R^2 for New Delhi and LA was 0.94 and 0.80 for the RFATPK method, whereas the RF method was 0.83 and 0.70, respectively. For the city of LA, the R^2 difference was 0.1, and the RFATPK produced more accurate predictions. The same trend was observed for the RMSE, low for the RFATPK method in both areas. Additionally, the slope values for RFATPK were 1.42 and 1.87, compared to 1.38 and 1.81 for the RF model in New Delhi and LA. Such difference demonstrates that the RFATPK is more accurate than RF when downscaling NTL.

4.4.5 Quantitative validation

For quantitative comparison of the downscaled NTL with the transformation PSF (denoted as RFTPK_U), we used the predictions proposed in our method (i.e., the ones presented in Figure 4-4 and Figure 4-5 (b)) and the predictions without accounting for the PSF (denoted as RFATPK_D). Moreover, we downscaled the NTL using ATPRK_D and an allocation of pixel values of the coarse resolution NTL to a grid of 130 m (called Allocation-based downscaling). Also, recent studies have proposed methods for downscaling NTL data, such as Geographically Weighted Regression (GWR) (Ye et al., 2021) and Multiscale Geographically Weighted Regression (MGWR) (Wu et al., 2022). To further highlight the effectiveness of the proposed method, we included the above approaches in comparison with RFATPK. For the ATPRK, GWATPK and MGWATPK, we removed predictors which had a Variance Inflation Factor greater than 10 since those methods are sensitive to multi-collinearity (Zhong et al., 2024). Luojia's NTL is used as the validation dataset and the results are presented in Table 4-4.

Table 4-4: Quantitative comparison (in terms of R^2 and RMSE) of the downscaling results for the NTL images for the two megacities. In **bold** are the results with the largest R^2 and smallest RMSE.

Megacity	**Method**	**Index**	
		R^2	RMSE
New Delhi	RFATPK$_D$	0.9281	10.4564
	RFATPK$_U$	**0.9355**	**9.9216**
	ATPRK$_D$	0.8955	13.8664
	GWR	0.8981	13.7053
	MGWR	0.9091	11.7018
	Allocation	0.9002	13.5680
LA	RFATPK$_D$	0.7988	42.2587
	RFATPK$_U$	**0.7997**	**42.1826**
	ATPRK$_D$	0.7723	44.6239
	GWR	0.7711	44.7264
	MGWR	0.7832	43.6784
	Allocation	0.7744	44.4478

Based on Table 4-4, for the megacity of New Delhi, it can be observed that the highest R^2 and lowest RMSE was achieved when using the proposed approach (RFATPK$_U$). 0.9355 and 9.9216 were the values for R^2 and RMSE, respectively. For LA, again, RFATPK$_U$ achieved the best results, with 0.7997 and 42.1825 for the R^2 and RMSE. Apart from the quantitative comparison a visual one was considered. Moreover, the Allocation-based downscaling performed better than ATPRK in LA, but RFATPK (with and without the PSF) outperformed the other methods in both megaregions. This is because the study sites there are multiple land cover/uses (e.g., airports, water bodies, vegetation), thus, a global regression model, such as the linear regression model in ATPRK$_D$, cannot capture the local spatial variability adequately. RF on the other hand, as a local model, can model the variations.

The maps below depict a visual comparison of the downscaling approaches for New Delhi (Figure 4-8) and LA (Figure 4-9).

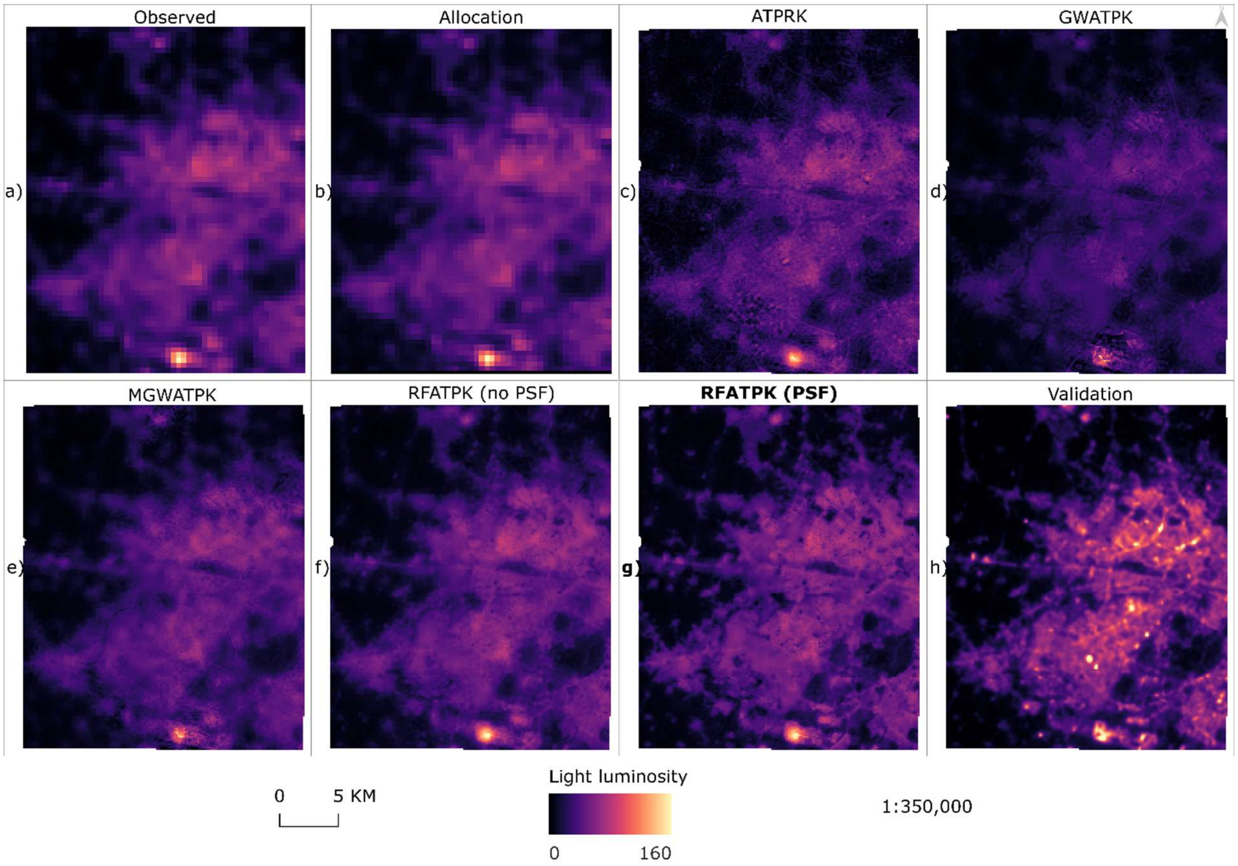

Figure 4-8: Downscaling results for the various downscaling approaches for the subregion of New Delhi’s megacity. a) Observed NTL data, b) Allocation-based downscaling, c) ATPRK, d) GWATPK, e) MGWATPK, f) RFATPK (no PSF), **g) RFAPTK (PSF)**, h) validation NTL data (Luojia). With **bold**, the proposed method.

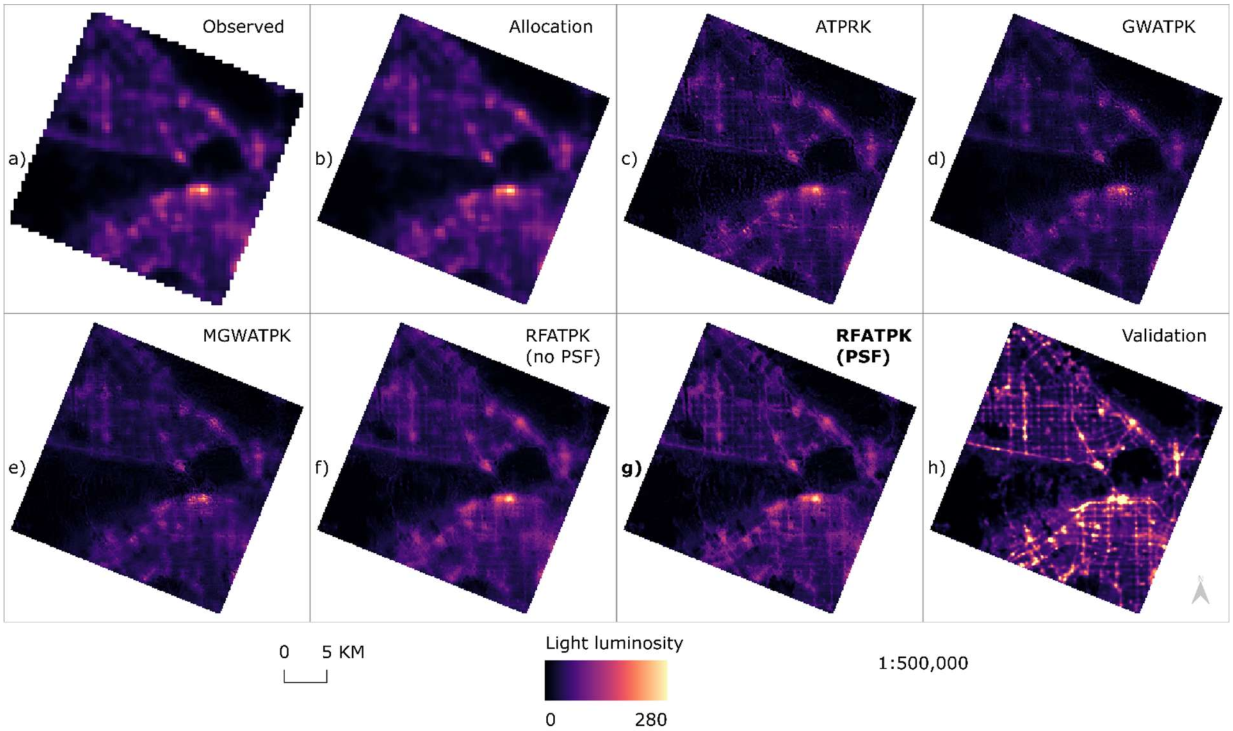

Figure 4-9: Downscaling results for the various downscaling approaches for the subregion of LA's megacity. a) Observed NTL data, b) Allocation-based downscaling, c) ATPRK, d) GWATPK, e) MGWATPK, f) RFATPK (no PSF), **g) RFATPK (PSF)**, h) validation NTL data (Luojia). With **bold**, the proposed method.

Local spatial differences could be noticed for the ATPK-based-downscaling techniques when compared with the validation product, revealed good agreement between the ATPRK and RFATPK downscaling results and Luojia for both megacities. In contrast, the patterns of validation data were not observed via Allocation-based downscaling. Pattern preservation is crucial since the validation data are taken as "true". For both megaregions, although the ATPRK and RFATPK (with and without the PSF) achieved satisfactory visual results, in the disaggregated NTL images using the RFATPK method, the spatial pattern appears clearer. ATPRK downscaled nighttime light imagery shows some outliers in the image for New Delhi, indicating areas where the model could not capture well the relationship between the data. RFATPK (PSF), shows spatial details (e.g., road network) clearer compared to the ATPRK and RFATPK (no PSF).

4.4.6 Urban socioeconomic applications

The results of linear regression between the socioeconomic indices, the coarse resolution NTL the downscaled NTL data with and without accounting for the PSF are presented in Table 4-5. For both megacities the R^2 between the indices and the downscaled NTL is larger than for coarse resolution NTL (denoted with the subscript C next to the index).

More precisely, for the megacity of New Delhi, the R^2 between the HDI and the NTL without the PSF (denoted with subscript D) was 0.4478 while for the NTL where the blooming effect was mitigated (denoted with subscript U) was 0.4383, a difference of 0.0095. This suggests that when not accounting for the PSF, the estimated human development is slightly higher compared to the approach when we proxy the index using the RFATPK_{U} but the difference is small. The income values for New Delhi are very close to each other, indicating that the method of downscaling NTL has a minimal, but noticeable, impact on the estimated income levels.

The HDI values for Los Angeles also exhibit a small range, with HDI_{U} being the highest. This implies that accounting for the PSF leads to a slightly higher estimation of human development compared to the other methods. For Los Angeles, leads to a higher estimation of income compared to the estimation when we use the coarse spatial resolution NTL and is almost identical when we use the downscaled NTL with the blooming effect being mitigated.

Table 4-5: R^2 between socioeconomic indices and luminosity (linear regression). In **bold** are the results with the largest R^2. The subscripts C, D, U means coarse resolution NTL, downscaled NTL without accounting for the PSF and downscaled NTL with the PSF being mitigated, respectively.

Megacity	**Index**					
	HDI_{U}	HDI_{D}	HDI_{C}	Income_{U}	Income_{D}	Income_{C}
New Delhi	0.4383	**0.4478**	0.4358	**0.2474**	0.2471	0.2465
LA	**0.2499**	0.2426	0.2240	0.2566	**0.2567**	0.2455

4.5 Discussion

Very few satellite sensor image enhancing techniques take into account how the neighbors physically influence the central pixel via the PSF effect. While taking the PSF into consideration, the suggested RFATPK method enabled the prediction of NTL at a fine spatial resolution (130 m) with highly satisfactory results. The downscaled data generated have a wide range of potential applications, including those that rely on image processing for remote sensing. The ability to discern the borders more clearly between land cover and land use classes is a significant gain that results from filtering, or minimization of the PSF effect. Two techniques of validation were used to assess the 130 m downscaled predictions: visual and quantitative.

4.5.1 Targeting predictors in RF

Although RF is applicable in high-dimensional settings due to its potential to identify informative predictors automatically, our results highlight the need to target a subset of predictors before final predictions. This is because the predictive power of the covariates is location dependent and different factors contribute to the spatial variation of NTL. An initial targeting step (i.e., variable selection) has been added to the RF algorithm, acting as an important complement to the prediction itself. Reducing the number of predictors has two benefits. Firstly, as mentioned in Borup et al. (2023), RF might fail in situations with high dimensionality, thus, reducing the number of predictors while keeping the strong ones only serves as a critical step. Secondly, predictors with high prediction power in one city might not be good covariates for another city, thus, with the variable selection we exclude the independent variables with poor predictive power from the subsequent analysis.

4.5.2 Downscaled Results

The 130 m RFATPK predictions for the two experimental regions of New Delhi and LA are shown in Figure 4-4 and Figure 4-5, respectively. While there are differences overall between the 130 m predictions and the validation data, the bright areas and NTL-free areas have a similar spatial structure. Even while the regression model in the RFATPK technique captured local spatial heterogeneity, it missed certain spatial information, particularly in the NTL extremes, that is the bright areas. This is because RF cannot model extremes well, especially when the distribution is heavily skewed (Heuvelink and Webster, 2022). Predictions in such areas with very high brightness are under-predicted, a phenomenon known as conditional bias (Takoutsing and Heuvelink, 2022).

RFATPK has three significant benefits. First, since it is nonparametric, incorporates prediction accuracy, and is resilient to noise, overfitting, and outliers, it can handle huge datasets with associated conditional variables. The built-in variable importance evaluation is the second. Each variable may be compared to the prediction results, and its significance is assessed by randomly permuting the variables. Theoretically, RFATPK should be suitable for downscaling and capable of resolving multivariable and nonlinear problems. Lastly, the scale effect of the residuals NTL when downscaling the VIIRS NTL was taken into account by the RFATPK.

As shown in Figure 4-4 and Figure 4-5, the road network for LA and the land cover for New Delhi played a crucial role in discriminating NTL luminosity. The results suggest that the method can be generalized to other megacities worldwide where the spatial structure of the road network can be readily obtained either from the fine resolution covariates or the land cover.

4.5.3 Fitting model for PSF estimation

The RF model was chosen for estimating the relationship between the coarse and fine bands in Eq. 13. Theoretically, other options like local regression or even spatially weighted regression can be used to quantify the non-linear relationship. When the research area is broad and the data gathering conditions (e.g., viewing angle) vary locally or regionally, these models could be more beneficial since the effective PSF becomes location-dependent (Wang et al., 2020). In this instance, an object- or pixel-based estimation of the PSF is possible. However, this spatially adaptive technique could be highly costly to compute, particularly if the research region is very large. In accordance with user needs, the computational burden and PSF estimation accuracy must be suitably balanced.

4.5.4 Comparison of the accuracy of the predictions with other methods

The performance of the RFATPK approach was compared with RF, GWATPK, MGWATPK, ATPRK, and Allocation of pixel values in two different geographic regions. Despite the simplicity of all models, GWATPK and MGWATPK require much more computational time compared to the rest of the methods, with the Allocation of pixel values being the fastest. This is because GWR and MGWR fit a separate regression model at each location. ATPRK, although computationally is fast, when the data exhibit local variations, such as the NTL, the global model cannot capture the changes in brightness in the study areas. In addition, GWATPK, MGWATPK and ATPRK cannot handle multicollinearity (Zhong et al., 2024). Allocation of pixel values, being the simplest form of downscaling, cannot increase the information content at fine spatial scale.

RF (without residuals downscaling) is a non-spatial model, and it ignores the geographical locations of the measurements. This can limit the prediction accuracy of the model. Another disadvantage of the RF approach is that the high spatial resolution predictions are not consistent with the observed coarse resolution NTL, because there is no constraint in the RF regression that ensures that the process is ideal (i.e., the model fully explains the NTL variability).

RFATPK, inherent the advantages of RF (i.e., can deal with large datasets, can handle multicollinearity, extreme values, and has good predictive power), and the advantages of ATPK (treats each observed data as a centroid by taking account of the spatially surrounding coarse pixels and size of support, holds the key superiority of coherence between the observed data and the predicted data, and does not require much computational time) (Yihang Zhang et al., 2021).

4.5.5 Describing the NTL blooming effect

This research presented a geostatistical solution (RFATPK) that can be used to address the PSF effect on NTL images. There is always a difference in PSF between bands and sensors. To ensure the effectiveness of the geostatistical solutions, the PSF must be characterized precisely. Since the majority of the research currently published claims that the Gaussian filter approximates the true PSF well, we assumed this filter for PSF estimation (Cao et al., 2019; Zheng et al., 2020). However, in practice, the true PSF can be more complicated than the Gaussian filter. The general strategy presented in this paper can be applied to other scenarios with different PSFs, as the implementation of RFATPK is not affected by the particular form of PSF (Wang et al., 2020).

It would be intriguing to examine various PSFs for both the along-track and across-track orientations (Wang et al., 2020). Additionally, hierarchical models may be considered to characterize the PSF. The PSF, for example, may consist of a combination of several filters, such as the triangular and Gaussian filters, or other filters (such as the ideal square wave filter). However, it should be noted that when downscaling, what matters is not the PSF of the original measurements (that is, the path from a point on the ground to a pixel in the image), but rather the transformation PSF between the original coarse and target fine spatial resolution (Wang et al., 2020). This implies that PSF characterization and estimation depend on the quality of the observed coarse and fine bands as well as the sensor; hence, estimation must be done case-by-case. The extent to which prospective alternatives, including nested models, may improve PSF characterization reliability, and how well they can generalize to handle data from other sensors, is unclear.

A small discrepancy was observed between the optimal R^2 in the regression among the megacities. This difference can be explained by the different atmospheric conditions and the number of images involved in the monthly composite. As mention by Bu et al. (2019), among the contributors to the PSF are atmospheric effects and the atmospheric conditions of the particular month (March for New Delhi, February for LA). In this research, the focus was the applicability of the method in general, that is, to mitigate the blooming effect during downscaling, and it should be noted that daily images (i.e., not a composite) should be used, where available, to model the *ideal* PSF of the NTL imagery. As stated in Section 2.2, we did not use the daily NTL product here because of the lack of pixels in the study regions due to cloud cover or other quality parameters. In future, we will utilize the daily NTL product from Black Marble (VNP46A2) to investigate the true measurement PSF of a range of NTL sensors.

4.5.6 Computational cost

The PSF effect causes a pixel's signal to be tainted by its surrounding pixels. More neighboring pixels are involved when taking the PSF effect into account while downscaling, than when not accounting for the PSF. This is accomplished for ATPK-based solutions using the semivariogram modeling procedure. As seen by Eqs. 8 and 9, convolution considers additional fine pixels from neighbors within the spatial coverage of the PSF, as opposed to standard ATPK, which considers only the center coarse pixel (i.e., without the PSF). The cost of computing will increase as more pixels are considered. The computing time for the two NTL images is displayed in Table 4-6.

Table 4-6: Processing time of RFATPK for the NTL images for the two megacities. VS stands for Variable Selection.

Megacity	**Method**	**Time (minutes)**	**VS (minutes)**
New Delhi	ATPK_U	6.45	0.36
	ATPK_D	6.27	
LA	ATPK_U	25.45	1.16
	ATPK_D	24.46	

The computation time increases from around 28 seconds for New Delhi and 1 minute for LA when the PSF is considered. This shows that, to provide more accurate downscaling forecasts, computing performance is in fact compromised when taking the PSF effect into account; yet the overall processing cost (a few seconds) may be considered acceptable. Because of the high level of parallelization of the R (R Core Team, 2025) package *atakrig* (Hu and Huang, 2020) and the coarser spatial resolution of NTL compared to the satellite sensor images, these findings differ from those of Wang et al. (2020). Here, fewer pixels cover the research area(s) compared to the data utilized by Wang et al. (2020) (10 m pixel size).

Moreover, the variable selection step, although adds more computational cost to the analysis (1 minute and 16 seconds for LA and 36 seconds for New Delhi), is a valuable step when there are a lot of predictors and, potentially, if include them all could reduce ability of RF model for prediction due to the use of weak predictors.

4.5.7 Ambiguities in spatial downscaling

Covariates must resemble the brightness in the study region in some way (such as similar spatial structure) to be useful to aid in downscaling. We purposefully avoided additional types of covariates (such as land use data) in this study where the relation with NTL could not be hypothesized explicitly, even though they may have increased the accuracy of downscaling in some cases. We may consider such data in the future because other authors have claimed to be able to enhance regression prediction accuracy (Chen et al., 2021).

As mentioned previously, RFATPK tends to underpredict regions with extremely high values. It was observed that downscaled NTL was biased in the highest brightness ranges. The difficulty of the RFATPK-based downscaling technique to replicate extremely high value light intensity is probably due to a lack of training data in these brightness ranges, which prevents the RF regression model from being properly calibrated. Extreme gradient boosting, or a different local model like the spatially weighted random forest, or a subset of machine learning known as deep learning (DL), might all be potential solutions for this specific problem. To the best of our knowledge, Wang et al. (2022) is the only example of downscaling NTL imaging using DL. Nevertheless, these methods are often computationally costly and need many training points. Although DL techniques have limitations, they are a viable option for modeling non-linear connections and should be considered in further research.

4.5.8 Urban socioeconomic applications

Effective criteria must be established to evaluate the differences in socioeconomic development between megacities and track advancement towards the global sustainable development goals. The potential utilization of fine resolution NTL data, which has not been employed widely in related studies, is enhanced by our findings and methodology. The experiments undertaken here demonstrated that downscaled NTL data represents a suitable proxy for measuring socioeconomic differences within megacities. The downscaled NTL data, which accounted for the PSF, reduced the blooming effect inherent in NTL data and increased the ability to represent socioeconomic variables relative to not accounting for the PSF. This means that NTL imagery at a fine resolution produced through the geostatistical approach for sharpening offers a valuable resource for socioeconomic applications, and an alternative to classical methods of measuring human activities.

The small correlation between the socioeconomic indices and the NTL (both at the coarse and fine spatial scales) was due to the fact that few observations (6) were used in the linear model. This small sample size limits the statistical power and the generalizability of the results, meaning that the findings should be interpreted with caution. Despite that, the results indicate that the disaggregated nighttime light data offers a better proxy than their coarse-resolution counterparts.

4.6 Conclusion

Due to their accessibility and usefulness as proxies, nighttime illumination data are utilized frequently in socioeconomic research. However, their spatial resolution is too coarse for many socioeconomic applications, and they are prone to the blooming effect which reduces even further the variation in brightness across pixels within cities and, thus, ultimately reduces the utility of the NTL data. Methods for downscaling remotely sensed images offer a possible solution to the former problem, but until now, the blooming effect in NTL data due to the PSF has not been addressed when downscaling NTL data. To improve downscaling in the multivariate case and account for the PSF impact while downscaling NTL, RFATPK, a geostatistical-based method, was applied in this research. The experimental findings showed that taking the PSF into account when downscaling generates more accurate predictions at the fine resolution. This benefit was shown to propagate forward to when evaluating social and economic phenomena at the urban scale using the downscaled NTL images.

Chapter 5 Uneven urban resilience across economic sectors revealed by satellite nighttime lights[3]

---

[3] This chapter is based on the *under-review* paper: Tziokas, N., Zhang, C., Tziokas, A., Atkinson, P.M., 2026, Uneven urban resilience across economic sectors revealed by satellite nighttime lights. Nature Cities

Abstract

Urban resilience is critical in the context of global disruptions such as the COVID-19 pandemic, yet recovery processes are rarely uniform across urban economies. How resilience varies across economic sectors and geographical contexts, and the extent to which it is structured by business essentiality, remains poorly understood at the global scale. Here, we use the COVID-19 lockdowns as a natural experiment and analyze monthly satellite-derived nighttime light trajectories for 98 city–sector combinations across 48 global cities between 2018 and 2023. We identify four archetypal sectoral trajectories that capture distinct resilience responses and reveal two dominant dimensions structuring recovery outcomes: economic essentiality and sectoral structure. Resilience is strongly polarized by essentiality, with resilient trajectories concentrated in essential economic sectors, while chronic decline is disproportionately associated with non-essential sectors, particularly in Europe. A pronounced geographic divergence emerges, as cities in Latin America and Asia consistently exhibit resilient or full recovery trajectories, in contrast to widespread and persistent sectoral decline across European cities. These findings show that urban resilience is neither uniform nor city-wide, but instead emerges from geographically contingent, sector-specific dynamics strongly conditioned by essentiality. Our findings call for a rethinking of urban resilience frameworks, moving beyond city-level aggregates toward sector-sensitive recovery strategies in an era of increasingly uneven urban transitions.

5.1 Introduction

Cities are often treated as cohesive systems when confronted with disruption, with recovery assessed through aggregate indicators at the city or regional level (J. Liu et al., 2024; Y. Zhang et al., 2024a). Yet major shocks rarely affect urban economies uniformly. As the immediate crisis receded following the COVID-19 pandemic, some cities rebounded quickly, while others experienced prolonged stagnation or decline (Liu et al., 2023; Yoruk et al., 2023; Lowe et al., 2024). The pandemic made these uneven recoveries observable at an unprecedented global scale (Bourdin and Levratto, 2024; Rao et al., 2024; Sun et al., 2024). These geographic disparities pose a central challenge for urban resilience research: whether cities recover as integrated wholes, or as assemblages of economic sectors with fundamentally different capacities to absorb and respond to shocks.

Recovery often fractures along internal economic lines, with different sectors following sharply divergent trajectories (Liu et al., 2023; Yuan and Hu, 2023; Sánchez and Cuadrado-Roura, 2024). While prior research has documented substantial variation in post-shock recovery across cities and regions (Li and Wei, 2023; Menoni et al., 2024; Zhang et al., 2024b), less is known about how these geographic disparities are produced through sector-specific dynamics within cities. City-level aggregates can signal stabilization even as some sectors stagnate or decline (Liu et al., 2024), potentially reinforcing pre-existing inequalities (Wang et al., 2024; Yoneoka et al., 2024; Wu et al., 2025b). Understanding urban resilience therefore requires moving beyond city-wide indicators to examine how recovery is distributed within cities.

Economic sectors constitute a critical but underexplored dimension through which urban resilience is produced and distributed. Ignoring sectoral dynamics risks obscuring structural vulnerabilities that shape post-shock trajectories and condition long-term recovery. A sectoral perspective is thus essential for identifying both vulnerable components of urban economies and the structural factors that shape recovery. Whether sectoral recovery trajectories exhibit generalizable patterns across cities worldwide remains an open question, and the role of sector essentiality in structuring resilience outcomes has yet to be examined systematically.

Progress on understanding sectoral resilience at global scales has been limited. Official economic statistics are often temporally lagged, spatially coarse, and inconsistent across national contexts (Chen and Quan, 2021; Du et al., 2024; Han et al., 2024; Hassankhani et al., 2021; Watmough and Marcinko, 2024; Yao et al., 2023). These constraints hinder their ability to capture dynamic, sector-specific responses to disruption that shape post-shock recovery (Ma et al., 2023; Z. Wang et al., 2024). As a result, empirical analysis of urban economic resilience has remained largely confined to aggregated city-level indicators or to narrowly defined case studies, limiting comparative insight into sectoral dynamics across diverse urban contexts.

Here, we use the COVID-19 lockdowns as a global disruption to examine resilience across key economic sectors within 48 globally distributed cities (Figure 5-1). By tracing post-disruption trajectories using monthly fine-resolution nighttime light (NTL) brightness as a proxy for sectoral activities, we identify archetypal patterns of recovery that reveal the dimensions distinguishing resilient from vulnerable sectors. Specifically, we ask why some urban economic sectors consistently recover while others experience persistent decline, and how these trajectories are shaped by sectoral function, essentiality, and geographic context. We show that urban resilience is neither uniform nor evenly distributed, but instead structured by sector-specific, and regionally contingent dynamics, with resilience outcomes strongly polarized by essentiality. These findings reposition sectoral structure and essentiality as central to understanding uneven urban resilience and its implications for post-shock recovery and global urban inequality.

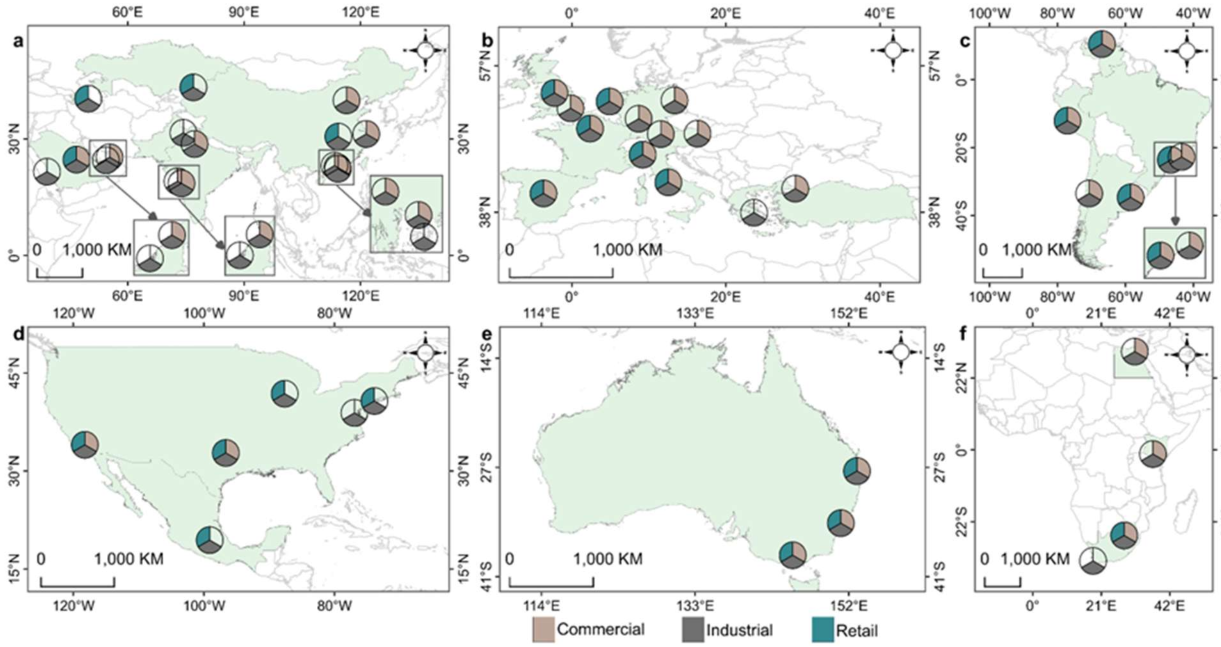

Figure 5-1: Study cities and sectoral delineations. Global distribution of the 48 study cities included in the analysis of sectoral resilience. Panels **a—f** show regional views for (**a**) Asia, (**b**)

Europe, (**c**) South America, (**d**) North America, (**e**) Australia, and (**f**) Africa. Each city is represented by a pie chart indicating the presence of commercial (brown), industrial (dark grey), and retail (green) sectors; blank slices denote the absence of a given sector in that city. Light green shading indicates the country of each sector. Insets highlight densely clustered cities to improve legibility at regional scales. Sectoral boundaries were delineated using OpenStreetMap data (https://download.geofabrik.de/), and continental outlines and national borders were obtained from World Bank open data (https://data.worldbank.org/).

5.2 Results

We identify four archetypal resilience trajectories in urban economic sectors following the COVID-19 lockdowns, defined by characteristic patterns in nighttime light (NTL) brightness (Appendix Figures A1-A4). These include Chronic Decline, marked by persistent post-lockdown reductions in NTL; Partial Recovery, characterized by incomplete rebounds that remain below pre-pandemic levels; Full Recovery, in which NTL returns to baseline conditions; and Resilient trajectories, where brightness is maintained or increases throughout the disruption period.

Using monthly fine-resolution NTL time-series from 2018 to 2023, we constructed trajectories for 98 city–sector combinations across 48 global cities (Methods; R^2 = 0.6–0.7 across periods; Appendix Table A-2). These combinations cluster into the four archetypes as follows: Chronic Decline (32.4%), Partial Recovery (13.3%), Full Recovery (22.9%), and Resilient (31.4%). Overall, only 54.3% of sectors achieve either sustained resilience or complete recovery by the end of the study period, indicating that prolonged vulnerability is a common outcome. The distribution of these trajectories reveals pronounced geographic differentiation across global urban systems.

5.2.1 Geographic divergence in sectoral resilience

Sectoral resilience patterns vary systematically across regions. European cities display widespread Chronic Decline across the commercial, industrial, and retail sectors, indicating broad-based and persistent post-pandemic contraction. In contrast, Latin American cities consistently exhibit Resilient trajectories across all sectors, while North American cities show greater sector-dependent variability. Cities in China and India achieve predominantly Resilient or Full Recovery outcomes, whereas Gulf cities present mixed trajectories across economic activities.

The above geographic contrasts are evident in the spatial distribution of recovery archetypes across the commercial, industrial, and retail sectors (Figure 5-2a–c) and are reinforced by continent-level net changes in NTL brightness (Table 5-1). European cities classified under Chronic Decline exhibit consistently negative net changes across sectors, with particularly large losses in retail activity (reaching −19.9 nW cm^{-2} sr^{-1}). In contrast, Resilient trajectories in South and North America are associated with substantial net gains in NTL brightness, especially in the commercial and retail sectors (reaching +20.9 nW cm^{-2} sr^{-1}). Full Recovery outcomes show moderate positive net changes across continents, reflecting intermediate recovery trajectories. Notably, these patterns do not align with a simple Global North–South divide, but instead indicate region-specific configurations of resilience and vulnerability across urban economies.

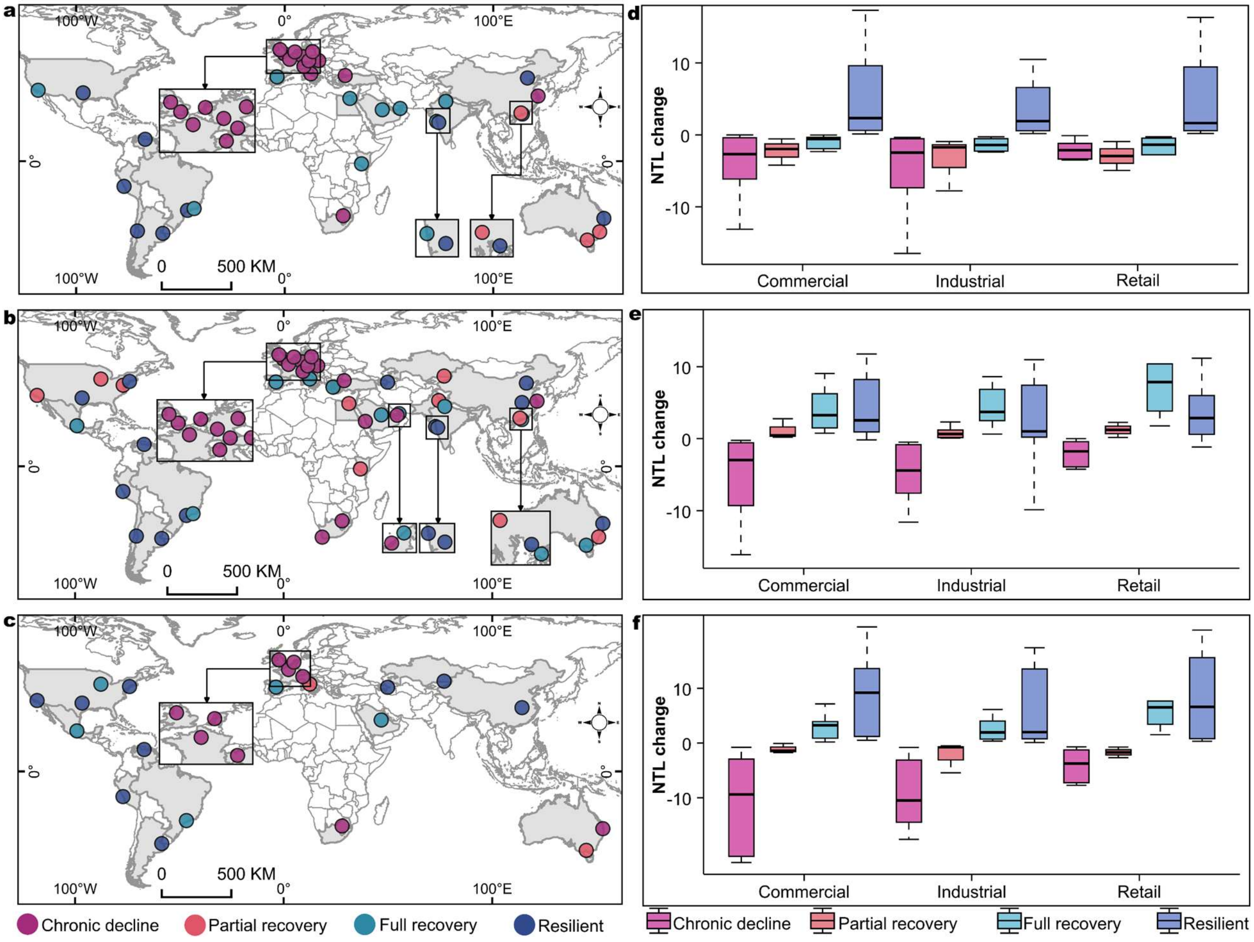

Figure 5-2: Sectoral polarization and geographic divergence in recovery archetypes. Spatial and temporal patterns of recovery archetypes across 98 city-sector combinations in 48 global cities between 2018 and 2023. **a**—**c**, Global distribution of recovery archetypes for the (**a**) Commercial, (**b**) Industrial, and (**c**) Retail sectors. Points are color-coded by archetype: Chronic Decline (purple), Partial Recovery (orange), Full Recovery (cyan) and Resilient (blue). Insets highlight densely clustered cities to improve legibility at regional scales. **d**—**f**, Sector-specific distributions of nighttime light changes across three recovery phases: Gross Impact (**d**; Lockdown minus Pre lockdown), Recovery (**e**; Post-lockdown minus Lockdown), and Net Impact (**f**; Post-lockdown minus Pre-lockdown). Boxplots are grouped by sector on the *x*-axis and colored by archetype, illustrating systematic differences in both shock exposure and recovery magnitude across sectoral trajectories. Center lines denote medians; box bounds represent the interquartile range; whiskers extend to 1.5× the interquartile range. National boundaries in **a**—**c** are based on public domain vector data by World Bank (https://data.worldbank.org/).

Table 5-1: Net sectoral change by resilience archetype and continent. Mean net change in nighttime light (NTL) brightness (nW cm^{-2} sr^{-1}) from pre-lockdown to post-lockdown periods, summarized by resilience archetype, continent, and economic sector. Archetypes are assigned at the city–sector level; continental values represent averages across observed city-sector combinations within each archetype. Negative values (purple shading) indicate sustained dimming in NTL brightness, whereas positive values (green shading) indicate net increases in activity. Cells marked with "–" denote continent-archetype combinations not observed in the dataset.

Archetype	Continent	Commercial	Industrial	Retail
Chronic decline	Africa	−0.8	−6.8	−1.6
	Asia	−15.8	−7.9	—
	Europe	−13.5	−17.4	−19.9
	Oceania	—	—	−5.9
Partial recovery	Africa	—	−0.6	—
	Asia	−1.4	−3.5	—
	Europe	—	—	−2.7
	North America	—	−1.7	—
	Oceania	−0.9	−0.7	−0.8
Full recovery	Africa	+4.0	—	—
	Asia	+5.1	+1.8	+15.4
	Central America	—	+6.1	+6.5
	Europe	+3.2	+2.2	+3.4
	North America	+0.9	—	+7.6
	Oceania	—	+0.3	—
	South America	+3.3	+4.2	+1.5
Resilient	Asia	+5.0	+4.9	+4.9
	North America	+13.0	+8.0	+7.7
	Oceania	+5.8	+2.0	—
	South America	+15.8	+8.1	+20.9

5.2.2 Sectoral polarization of resilience outcomes

Within this globally differentiated landscape, resilience trajectories diverge sharply across economic sectors. Commercial activities exhibit the most polarized responses, with 37% experiencing Chronic Decline, concentrated in European cities such as Amsterdam, Berlin, and Frankfurt (Appendix Figure A-1), while 29% follow Resilient trajectories, notably in Buenos Aires, Beijing, and Brisbane (Figure 5-2a; Appendix Figure A-4). Industrial sectors display a more balanced distribution across archetypes, including Chronic Decline (31%), Partial Recovery (19%), Full Recovery (21%), and Resilient (29%) (Figure 5-2b). Retail sectors demonstrate the highest overall resilience, with 41% maintaining Resilient trajectories, particularly in North and South American cities including New York, Los Angeles, Buenos Aires, and Caracas (Appendix Figure A-4), although 27% experience Chronic Decline, predominantly in Europe (Figure 5-2c; Appendix Table A-2).

Differences between archetypes emerge during lockdown periods and intensify thereafter. During lockdowns, Resilient sectors maintain positive NTL changes across all sector types (mean change: +5.32 Commercial, +3.68 Industrial, +4.91 Retail), whereas Chronic Decline sectors experience substantial contractions (−4.29 Commercial, −4.60 Industrial, −2.92 Retail) (Figure 5-2d; Appendix Table A-3). Post-lockdown trajectories diverge further: Full Recovery sectors rebound strongly (mean change: +5.50 Commercial, +4.34 Industrial, +10.9 Retail), while Chronic Decline sectors continue to deteriorate (−8.38 Commercial, −9.47 Industrial, −11.6 Retail) (Figure 5-2e). Net changes from pre-pandemic baselines to the study endpoint reveal sustained gains in Resilient sectors and comparably large cumulative losses in Chronic Decline sectors (Figure 5-2f).

5.2.3 Essentiality and sectoral structure as dimensions of resilience

Resilience outcomes across cities and sectors are structured along two dominant and interpretable dimensions, revealing a latent resilience space shaped jointly by economic essentiality and sectoral structure. Multiple Correspondence Analysis identifies a first dimension (32% of explained variance) separating essential from non-essential activities, and a second dimension (26%) differentiating Commercial and Retail sectors from Industrial activity (Figure 5-3a).

Resilience archetypes segregate significantly along the essentiality dimension ($\chi^2 = 11$, p = 0.01), with Resilient trajectories disproportionately associated with essential services and Chronic Decline concentrated among non-essential activities (Figure 5-3b). Segregation is greater along the sectoral structure dimension, ($\chi^2 = 16$, p = 0.001), where Chronic Decline clusters within Commercial and Retail sectors and Full Recovery trajectories are associated predominantly with Industrial sectors (Figure 5-3c). Joint consideration of both dimensions reveals distinct configurations of vulnerability and robustness: essential Industrial sectors occupy the most resilient region of the resilience space, whereas non-essential Commercial and Retail activities form the most vulnerable cluster (Figure 5-3a, Figure 5-3d). Sectoral structure explains a greater share of variance in resilience outcomes ($\eta^2 = 0.17$) than essentiality alone ($\eta^2 = 0.12$), indicating that urban resilience is shaped not only by whether activities are deemed essential, but also by how sectoral functions are embedded within urban economic systems.

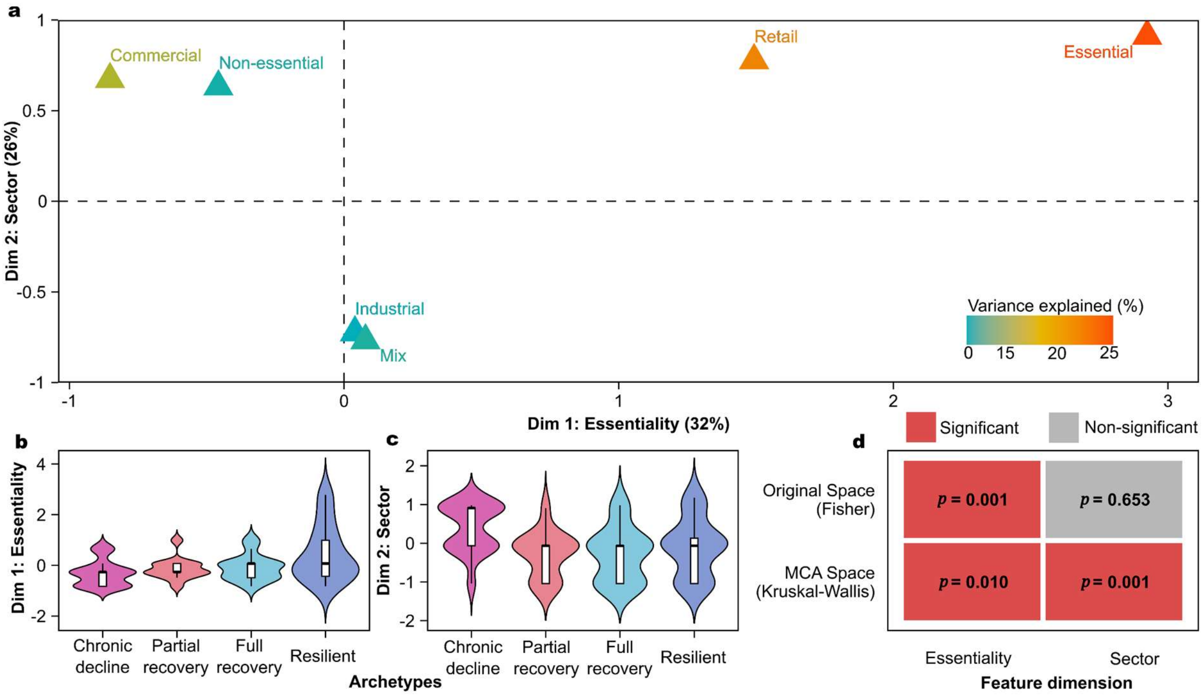

Figure 5-3: Essentiality and sectoral structure organize resilience archetypes. Multiple Correspondence Analysis (MCA) of resilience archetypes across 98 city–sector combinations, showing how recovery outcomes are structured by economic essentiality and sectoral configuration. **a**, MCA variable contribution showing the two principal dimensions of resilience space: Dimension 1 (Essentiality; 32% of variance explained) and Dimension 2 (Sector; 26% of variance explained). Points represent categorical variables, positioned according to their association with each dimension; color intensity indicates relative contribution to dimensional structure (red = high contribution, blue = low contribution). **b**, **c**, Distributions of resilience archetypes along Dimension 1 (**b**) and Dimension 2 (**c**), demonstrating systematic separation of archetypes along the essentiality and sectoral axes, respectively. Boxplots show median values (center lines), interquartile ranges (boxes), and 1.5× interquartile ranges (whiskers). **d**, Statistical tests supporting these separations: Fisher's exact tests indicate significant associations between archetypes and both essentiality and sector type in the original categorical space, while Kruskal–Wallis tests confirm significant differentiation of archetypes along the MCA dimensions.

5.3 Discussion

This study demonstrates that urban economic resilience to global disruption is neither uniform nor city-wide, but instead structured by sectoral function, essentiality, and geography. Using COVID-19 lockdowns as a natural experiment, we show that urban sectors follow distinct resilience archetypes, revealing systematic divergence rather than convergence (Glückler, 2007; John, 1993) in post-shock trajectories. Chronic Decline remains widespread, particularly in European cities, while Resilient and Full Recovery outcomes cluster in specific sectors and regions. Together, these findings challenge prevailing resilience frameworks that assume either rapid rebound (Glückler, 2007; John, 1993) or path-dependent (Bourdin and Levratto, 2024) recovery at the city scale, and instead point to a sectoral differentiated resilience landscape.

Our results reveal that three interrelated dimensions—essentiality, sectoral structure, and geographic context—jointly shape resilience outcomes. While each dimension has been discussed independently in prior work (OECD, 2020; W. Wang et al., 2022; Y. Zhang et al., 2024a), our analysis integrates them within a single empirical framework, demonstrating how their interaction produces patterned configurations of vulnerability and robustness. Essentiality emerges as a primary axis of resilience, with sectors linked to indispensable provisioning and production maintaining activity during disruption and recovering more rapidly thereafter. Sectoral structure further differentiates outcomes: industrial activities embedded in stable value chains are more resilient than commercial and discretionary retail sectors reliant on mobility and non-essential consumption. Geographic context moderates both dimensions, amplifying or dampening vulnerabilities depending on regional economic structures and institutional capacity.

These interacting dimensions explain why resilience and decline coexist within urban economies. Industrial sectors demonstrate robustness not simply because they are essential, but because their functions are supported by redundancy, substitutability, and continuity within broader production networks. In contrast, commercial and discretionary retail sectors experience chronic decline where demand is structurally contingent on physical co-presence (Huang et al., 2024) and discretionary spending. Under such conditions, firm-level adaptation cannot compensate for the absence of essential demand, revealing limits to resilience strategies that focus narrowly on flexibility or innovation without addressing structural exposure (Setyadi et al., 2025). Retail sectors illustrate this bifurcation most clearly, with essential provisioning maintaining throughput while non-essential formats remain persistently vulnerable.

Geographic divergence further underscores that resilience is not governed by universal urban mechanisms. European cities exhibit disproportionately high rates of Chronic Decline across sectors, particularly in commercial and retail activities, reflecting region-specific structural constraints (Dascher-Preising and Greiner, 2023) rather than intrinsic urban fragility. In contrast, cities in Latin America and Asia display more resilient trajectories across sectors despite comparable exposure to global disruption, suggesting that economic diversity and functional composition can offset shock impacts. These patterns highlight the importance of context in resilience assessment and caution against generalized interpretations of post-pandemic recovery.

The findings carry important implications for urban resilience policy. Rather than pursuing uniform recovery strategies, interventions should be attuned to sectoral vulnerability and structural exposure (Dascher-Preising and Greiner, 2023). Policies that strengthen essential provisioning, support diversification within sectoral systems, and enable functional reconfiguration of vulnerable commercial spaces are more likely to enhance resilience than place-based strategies alone (Z. Liu et al., 2024; Z. Wang et al., 2024). Crucially, resilience planning should recognize divergence as a structural condition of urban economies rather than an anomaly to be corrected.

Several limitations warrant consideration. Nighttime light data capture activity intensity rather than economic value, precluding direct comparison with conventional indicators such as GDP or Gross Value Added. Nevertheless, fine-resolution NTL enables consistent global comparison of sectoral dynamics that remain poorly observed in official statistics. Interpretation of European Chronic Decline should also consider policy- and technology-driven factors that may reduce observed illumination without implying proportional economic contraction, including remote working practices (Fellnhofer et al., 2025), emissions-reduction strategies, and the widespread transition to energy-efficient, directional LED street lighting (Kyba et al., 2021). In addition, sectoral aggregation relies on OpenStreetMap land-use polygons, which distinguish broad functional classes, but which do not encode higher-order differentiation within sectors (e.g., banking or financial services within commercial land use), potentially grouping activities with distinct operational roles and lighting behaviors. Future research should address these limitations by integrating NTL data with higher-resolution functional classifications derived from national land-use datasets, administrative records, or firm-level information, and by jointly examining policy, energy, and institutional drivers of observed NTL trajectories. Future research could integrate sectoral NTL trajectories with economic, institutional, and governance indicators, extend analysis to neighborhood and firm scales, and examine whether similar resilience spaces emerge under other forms of disturbance, including climate-related or financial shocks.

Taken together, this study suggests that urban resilience is best understood as plural rather than singular: a configuration of sector-specific and context-dependent trajectories shaped by essentiality, structure, and geography. Recognizing this plurality is essential for rethinking how cities adapt to global disruption and for designing resilience strategies that acknowledge, rather than obscure, uneven urban transitions.

5.4 Methods

We analyze sectoral urban resilience using archetypal representations derived from nighttime light (NTL) trajectories. Monthly fine-resolution NTL brightness is used as an indicator of sectoral activity intensity, enabling systematic and comparable analysis of disruption and recovery trajectories across cities and economic sectors.

5.4.1 Study area and sectoral delineation

We conducted a comparative analysis of sectoral resilience across 48 global cities spanning all inhabited continents (Figure 5-1). Three urban economic sectors—commercial, industrial, and retail—were selected due to their central role in post-COVID urban economies and their contrasting functional characteristics. Sectoral polygons were delineated using OpenStreetMap (OSM) land-use features (“OpenStreetMap,” n.d.) and ESRI Land Cover data (“Esri Land Cover,” n.d.). To ensure temporal consistency, only polygons present in both 2018 and 2023 were retained, excluding areas that underwent functional conversion (Liu et al., 2019). Polygons smaller than 25 ha were removed to align with the spatial resolution of nighttime light data. This process yielded 98 city–sector combinations for analysis.

Cities were selected through a sequential filtering procedure based on the Globalization and World Cities (GaWC) classification (“World Cities 2024 – GaWC,” n.d.) to ensure global coverage while avoiding regional over-representation (Xu et al., 2021). Cities were excluded if they exhibited persistent cloud contamination, ambiguous nighttime light patterns, or insufficient data quality. Only cities that experienced documented COVID-19 restriction policies, as recorded by the Oxford COVID-19 Government Response Tracker (OxCGRT) (Hale et al., 2021), were retained.

5.4.2 Nighttime lights (NTL) data

Monthly nighttime light (NTL) data were obtained from NASA’s Black Marble product (VNP46A3), which provides globally consistent, cloud-masked observations at a native spatial resolution of 500 m (Román et al., 2018). Quality flags were applied to exclude low-quality observations. To improve spatial precision and better align with sectoral polygons, NTL data were downscaled to 130 m resolution using Random Forest Area-to-Point Kriging (RFATPK) (Tziokas et al., 2024). Mean NTL brightness was calculated for each sectoral polygon using area-weighted aggregation, generating monthly time series from January 2018 to December 2023.

To isolate resilience-related brightness changes from urban expansion, we applied a stable built-up mask using ESRI 10 m land cover data for 2018 and 2023. Only pixels classified as impervious in both years were retained, ensuring that observed NTL changes reflect sectoral activity rather than land-use change (Liu et al., 2019).

5.4.3 Time-series decomposition using STL

Sector-level NTL time series were decomposed using Seasonal-Trend decomposition via LOESS (STL) (Clevelard, B et al., 1990; Zhao et al., 2020) to separate long-term trends from seasonal and irregular components. The trend component was retained as an indicator of underlying sectoral activity. For each city–sector combination, piecewise linear regressions were fitted to pre-lockdown, lockdown, and post-lockdown periods, defined using the “Stay-at-home requirements” indicator (C6) from the Oxford COVID-19 Government Response Tracker (Hale et al., 2021). Midpoint values of each segment were extracted to characterize trajectory shifts across periods. Temporal sequences of NTL brightness (y_t) were divided into trend (T_t), seasonal (S_t), and remainder (R_t) additive components:

$$y_t = T_t + S_t + R_t \tag{1}$$

5.4.4 Resilience archetype classification

We adopted an archetypal approach (Cutler and Breiman, 1994) to characterize extreme patterns of sectoral response. Four archetypes were defined based on relative changes in NTL trends across the three periods: Chronic Decline, Partial Recovery, Full Recovery, and Resilient. City–sector combinations were assigned to archetypes using explicit, rule-based criteria based on the relative ordering of segment midpoints, ensuring transparency and reproducibility.

5.4.5 Sector classification and essentiality

Sectoral polygons were classified through systematic visual inspection using high-resolution imagery in Google Earth Pro (Google LLC, 2025), cross-referenced with OSM attributes. Classification criteria were applied consistently across cities. Essentiality was categorized as essential, non-essential, or mixed based on whether sectoral functions were designated as indispensable during COVID-19 restrictions. Sectoral structure and essentiality were treated as categorical variables in subsequent analysis.

5.4.6 Multiple Correspondence Analysis (MCA)

To examine how essentiality and sectoral structure relate to resilience archetypes, we applied Multiple Correspondence Analysis (MCA) (D'Esposito et al., 2014) to the 98 city–sector combinations. MCA was used to identify latent dimensions structuring categorical associations among sector type, essentiality, and resilience archetype. The first two dimensions, which captured the largest share of explained variance, were retained for interpretation and hypothesis testing. MCA builds a disjunctive matrix of polygons and categories, where distances between polygons are characterized by the infrequency of shared categories. Formally, the Chi-square distance between two polygons (i) and (i') is given in Eq. 2:

$$d\left(i,i^{\prime}\right)=\sqrt{\sum_{j}\left(\frac{\left(p_{ij}-p_{i^{\prime}j}\right)^{2}}{p_{+j}}\right)} \tag{2}$$

where p_{ij} and $p_{i'j}$ are relative frequencies for row i and i' in column j and p_{+j} is the marginal relative frequency, or “mass” as it is called in MCA, for column j. Polygons possessing identical categories aggregate proximate to the origin of the dimensional space, whereas less frequent categories are positioned farther along the axes. Singular value decomposition produces principal axes that optimize captured variance, enabling categorical diversity to be visualized within a condensed dimensional framework. The first dimension was retained as the data-driven index of resilience divergence, capturing the greatest variability among city–sector combinations.

Chapter 6 Discussion and Conclusions

Leveraging nighttime light data to assess sector-level urban resilience comprehensively on a global scale poses a formidable challenge, necessitating scalable methodologies capable of encompassing all the dimensions of resilience. The primary challenges in evaluating sector-level urban resilience using nighttime lights data are the coarse spatial resolution of current NTL datasets, which obscures fine-grained sector-specific fluctuations, and the dynamic character of urban economic activity, which necessitates real-time analysis. The development of sophisticated analytical frameworks that incorporate fine-resolution NTL data and dynamic analysis is necessary to assess sector-specific urban resilience accurately and to bridge the gap between satellite-derived metrics and ground-truth socioeconomic datasets.

Fine-resolution NTL data offers a promising systematic approach for sector-level urban resilience assessment, as this approach utilizes alterations in brightness, which serve as indicators of sector-specific reactions to external disturbances, and the integration of this approach enables the monitoring of economic and infrastructural activity, offering a multifaceted framework for understanding and addressing complex urban resilience challenges. This strategy is informed by the broader concept of urban resilience, which posits that various components of a city demonstrate disparate recovery patterns in the aftermath of shocks, such as the novel COVID-19 pandemic (Z. Liu et al., 2024). The capacity of discrete urban sectors, such as retail, airports and industrial, to withstand and recover from adverse impacts is referred to as sectoral resilience (Fromhold-Eisebith, 2015). This concept is manifested in the temporal variations in NTL brightness, as they are frequently influenced by a combination of sector-specific traits, policy actions and general economic conditions which, in turn, drive patterns of resilience. Cities may be categorized into different resilience trajectory scenarios according to sectoral performance throughout time by methodically examining these trends, offering a uniform yet adaptable framework for worldwide investigation and enables an organized comparison of urban resilience across various circumstances. As a result, combining sectoral resilience indicators with fine-resolution NTL data provides a scalable and data-driven approach for comprehending urban resilience dynamics at a never-before-seen degree of detail.

This thesis developed a novel analytical framework that utilizes fine-resolution NTL data to classify cities into distinct urban resilience scenarios based on sector-based NTL trajectories, enabling comprehensive evaluation of sectoral performance through clearly defined metrics. To ensure a detailed knowledge of sectoral resilience dynamics, the research was carried out independently for the three main urban sectors: retail, industrial and airports. The main drivers of the resilience trends were determined by combining sector-specific features, and qualitative evaluations. Mitigation of the blooming effect while downscaling nighttime lights data and their validation as a proxy for sectoral productivity were also crucial methodological considerations for the use of fine-resolution NTL data, which produced a large correlation between the NTL trends and sector-specific economic performance. By addressing the shortcomings of traditional resilience assessment techniques that depend on surveys or nation-specific economic data, these methodological advancements provided a framework that is both scalable and globally applicable. In addition, the classification of urban resilience trajectories was designed to provide policymakers with a simple yet accurate way to rapidly determine which sectors of a city were most affected - either positively or negatively - by shocks like the COVID-19 pandemic lockdowns. More informed decision-making is made possible by this methodical, data-driven approach, which also advances our worldwide understanding of urban resilience. In conclusion, this thesis makes the following significant contributions:

1. Implementing a geostatistical downscaling method for NTL data, which has been utilized for daytime satellite images, with great potential for use in NTL-based urban research.
2. Enhancing the quality of NTL imagery and increasing its accuracy for urban research and applications by mitigating the blooming effect in downscaled NTL data, for the first time.
3. Developing a method that is sector-specific, globally scalable, and which does not rely on traditional data, and is of outmost importance for targeted economic policies at the operational level in the "New Normal" that societies are now living in.

This chapter presents the primary conclusions derived from the research, while addressing the research issues posed and offering suggestions for the future.

6.1 Research findings and conclusions

This section of the study presents the findings and conclusions of the research, which are supported by the objectives outlined in Section 1.5.

Objective 1: Apply a modern geostatistical solution, named RFATPK, which specifically has been applied to daytime imagery, to downscale a nighttime imagery. This objective examined whether a modern geostatistical analysis model could be adapted from daytime satellite imagery to nighttime light (NTL) data without sacrificing spatial or radiometric accuracy. The RFATPK technique combines machine learning modeling with geostatistical residuals downscaling, allowing it to account for local variations while maintaining perfect coherence across different levels.

Applying RFATPK to satellite NTL data in differing major urban hubs (New Delhi and Mumbai) showed that the approach steadily surpassed other downscaling methods in both statistical testing and expert observation. In comparison to alternative regression-based methods, RFATPK generated more smooth and coherent lighting layouts while maintaining fidelity to the original coarse-resolution data.

This is vital for urban resilience research, where random local noise can be mistakenly viewed as financial shifts. The results confirm that RFATPK is an effective and transferable solution for NTL downscaling, enabling fine-resolution representations of urban economic activity that are robust enough for subsequent sector-level analysis.

Objective 2: Mitigate the blooming effect, inherent in every nighttime imagery, while downscaling it to enhance the downscaled imagery both visually and quantitatively. This objective tackled a major flaw of nighttime light data: the blooming effect, which consistently "bleeds" light from bright locations into nearby zones. If left unchecked, spillover creates geographic distortion that exaggerates perceived growth in crowded city centers and hides poverty or downturns elsewhere.

Blooming reduction was directly built into both phases of the analytical framework—during the statistical modeling phase and within the downscaling process. By factoring in the light diffusion patterns into the spatial analysis workflow, the technique fixed light bleed while maintaining radiometric accuracy.

Although gains in overall accuracy metrics (e.g., R^2) appear statistically small, they signify the removal of predictable spatial bias rather than random noise. For measuring economic wealth, such adjustments are practically impactful: small changes in measured brightness can shift growth categories, risk rankings, and government focus. The findings show that adjusting for blooming improves the clarity and trustworthiness of satellite-based economic indicators, thereby increasing their value for urban resilience studies.

Objective 3: Using the downscaled nighttime imagery, monitor urban resilience at the sector level and understand the factors behind it. Drawing upon the methodological progress of Objectives 1 and 2, the current objective created a structured model to assess urban resilience at the sector level using fine-resolution nighttime light data. Rather than viewing cities as uniform entities, the research analyzed commercial, industrial, and retail sectors separately, acknowledging that industries vary in vulnerability, and exposure to mobility restrictions.

Sectoral light-activity trends during and after COVID-19 lockdowns were grouped into four archetypes—Chronic Decline, Partial Recovery, Full Recovery and Resilient—offering a scalable and clear depiction of resilience patterns. The findings demonstrate that resilience is not evenly distributed: essential sectors consistently show stable NTL trajectories, while non-essential ones, particularly in European cities, undergo lasting decline in NTL brightness.

By connecting archetypal outcomes to essentiality, sectoral structure, and geographic setting, this chapter demonstrates that urban resilience is determined by foundational economic factors rather than general urban processes. These discoveries provide practical insights for government officials by pinpointing which economic sectors are inherently at risk and which setups enable adaptive capacity under global shocks.

6.2 Reflections

This core of this thesis is organized into three primary chapters (Chapters 3 to 5), each of which focuses on a distinct aspect of the research, which were the development and enhancement of downscaling methods for NTL data, the integration of blooming effect within the framework of downscaling, and the application of fine-resolution NTL data for urban resilience analysis. This thesis is primarily based on the following logical progression: initially, fine-resolution NTL serve as a better proxy for urban studies, then, by mitigating an effect that exists ubiquitously in NTL imagery (i.e., the blooming effect) researchers can further enhance the suitability of nighttime lights data for modelling social and economic phenomena related to cities, and finally, using these fine-resolution NTL (with the blooming effect being mitigated), researchers can monitor urban resilience at the sector level. Detailed links are shown as follows:

When addressing the challenge of downscaling NTL data to enhance its applicability for socioeconomic studies, chapters 3 and 4 collectively illustrate how methodological advancements can serve as a conduit to bridge the prevailing gap between coarse-resolution satellite data and urban-scale analysis. The coarse spatial resolution of NTL imaging is a basic drawback that limits its use to fine-scale urban studies. In diverse urban settings, “traditional” ATPRK is not the optimal approach since it assumes spatial stationarity. Hence, to generate fine-resolution NTL data, Chapter 3 presented Random Forest Area-to-Point Kriging (RFATPK), a novel geostatistical downscaling approach that combines machine learning with geostatistical interpolation. This approach maintained the property of perfect coherence while demonstrating superior accuracy when compared to benchmark techniques. Nevertheless, the PSF of the NTL data was not specifically taken into consideration by RFATPK in chapter 3. This is a problem that is especially pertinent in cities where there is concentrated artificial illumination. By incorporating the PSF into the downscaling process, Chapter 4 overcame this limitation and ensured that the geographical redistribution of light more accurately reflects the actual spatial distribution of socioeconomic activity. The accuracy of downscaled NTL data was increased both visually and numerically by simulating explicitly the PSF, especially in high-density urban environments. Although more effort is required to generalize the methodology across various urban morphologies and lighting conditions, these methodological developments helped to increase the usefulness of NTL for fine-scale urban research.

Chapter 5 applies the improved nighttime light data developed in Chapters 3 and 4 to examine how different urban economic sectors responded to and recovered from the COVID-19 pandemic. Using monthly satellite observations for 98 city–sector combinations across 48 global cities, the chapter shows that recovery is not uniform within cities, but varies systematically across sectors and regions. Essential sectors consistently maintained activity or recovered quickly, while non-essential sectors—particularly in European cities—experienced persistent decline. These patterns demonstrate that urban resilience cannot be understood at the city level alone, but must be assessed at the level of economic function. For decision makers, this finding is important because it shows that uniform recovery policies risk overlooking structurally vulnerable sectors. The chapter demonstrates that fine-resolution nighttime light data provide a scalable and globally comparable way to identify where resilience is strong, where it is weak, and which sectors require targeted intervention, even in contexts where detailed economic statistics are unavailable.

These methodological advancements reflect a systematic refinement process focused on enhancing both precision and interpretability of the fine-resolution NTL data. The initial focus on spatial resolution and spectral coherence in Chapter 3 formed the groundwork for the PSF correction analyzed in Chapter 4, ultimately enabling the sector-level urban resilience monitoring introduced in Chapter 5. Each advancement built upon the previous work, creating increasingly accurate spatial representations of urban illumination. The spatial scales of study also grew over the chapters. To validate the downscaling technique, experiments were carried out in particular urban case studies (such as Mumbai, New Delhi and Los Angeles) in Chapters 3 and 4. In order to evaluate sectoral resilience, Chapter 5 then expanded the methodology globally, including 48 cities. The suggested framework's scalability is highlighted by this transition from methodological development to worldwide use.

Future studies might consider including more socioeconomic datasets, enhancing robustness across various urban contexts, and modifying the approach for real-time applications, that is, building on the results in this thesis which show the promise of fine-resolution NTL for monitoring urban resilience. The implementation of the downscaling approaches detailed in chapters 3 and 4 relied exclusively on open-source software tools, namely the R (R Core Team, 2025) platform which underscores the potential for the development of technically rigorous and replicable methodologies for NTL sharpening through the utilization of accessible computing resources and these findings underscore the feasibility of implementing analogous approaches in diverse institutional or resource-constrained contexts. Downscaling the data required for Chapter 5, Lancaster's High-End Computing (HEC) was used, which can process large volumes of data through parallel computing. This enabled the research focus to shift from local (i.e., a couple of cities studied in Chapters 3 and 4) to global analysis, where such compute resource is needed for quantifying global responses to lockdown policies at fine-spatial scales.

In conclusion, the creation of techniques that allow for precise sector-level evaluations of urban resilience monitoring using fine-resolution nighttime light data can make a substantial contribution to international efforts to promote urban sustainability by providing insightful information for well-informed policy decisions and focused interventions.

6.3 Recommendations

This thesis developed a novel approach for sector-level urban resilience assessment using downscaled nighttime light data, addressing the inherent limitations of coarse-resolution imagery and the blooming effect. While this research provides a foundation for global-scale analysis, many aspects of the approach warrant further investigation. First, while NTL data serve as a useful proxy for human activity and urban vibrancy (Yatao Zhang et al., 2021), they inherently lack completeness due to factors such as missing data caused by weather conditions and the focus on nighttime activities. This means that NTL data may not capture urban resilience comprehensively during adverse weather conditions or the daytime. An important direction is the integration of broader datasets beyond the data used in this study, enabling a more comprehensive understanding of the multi-dimensional nature of urban resilience. Furthermore, this study used broad sectors (e.g., retail, industrial) for the analysis. Future research should include more detailed functional land uses (e.g., types of industrial sectors). Moreover, this study utilized monthly composites of NTL. It would be of great interest to adopt the same methodology using nightly NTL and monitor resilience on that basis.

Apart from the previous recommendations discussed beforehand, the proposed downscaling methods could also be developed further from multiple perspectives, including data sources, techniques and applications. Detailed recommendations are made as follows:

1. Data sources

The thesis focused on downscaling NTL imagery using specific ancillary variables to assist the downscaling. However, many other data sources exist in the field of remote sensing, such as hyperspectral, synthetic aperture radar (SAR) and LiDAR, which have not been used in this research, and the fusion of these multiple data sources would be a potential future direction. Moreover, land use and land cover data could also be incorporated along with other socioeconomic variables, like points of interest (POIs), as they reflect certain elements of human activity and they are closely linked to NTL (Ye et al., 2021).

2. Techniques

Deep learning is a common subfield of machine learning that has been researched extensively for downscaling (Zhang et al., 2024). The primary benefits of deep learning-based techniques are similar to those of conventional learning-based techniques in that they can successfully decrease downscaling uncertainty by using spatial structure information in real fine spatial resolution images (i.e., training data) to train a model. Future studies should investigate this kind of approach given deep learning's potent non-linear fitting capability for challenging issues. The spatial variability of the PSF with the sensor's viewing angle (VA) is a crucial component that is frequently ignored by the state-of-the-art in downscaling remote sensing imaging, especially when it comes to NTL data. Although previous research recognizes the significance of taking the PSF into consideration (Wang et al., 2020), it always assumes a static, or “fixed,” PSF for the whole image. This simplification ignores the intrinsic spatial variability of the PSF and is usually expressed as a single value, such as the standard deviation of a Gaussian filter. In practice, the PSF fluctuates as the sensor's VA departs from the nadir. A key optical characteristic of the sensor, the angular dependency of the PSF, has important ramifications for downscaling accuracy, particularly when taking into account the blooming effect in NTL data.

The blooming effect will unavoidably be more noticeable with a broader PSF, which means the sensor disperses light from a point source across a larger region. On the other hand, less blooming occurs with a narrower PSF, when the light is more narrowly concentrated. As a result, the PSF's size and shape directly affect how much blooming is realized. Because the PSF itself changes depending on the viewing angle of the sensor, this connection is essential.

To account for the shifting PSF and how it affects the measured brightness, the transfer function used in downscaling should ideally be a function of the VA. The transfer function may dynamically adapt to the image's fluctuating levels of blurring by integrating the VA into the downscaling procedure. This would make it possible to recreate the underlying light distribution more precisely, especially in regions where there are notable VA changes.

A notable gap in existing approaches is highlighted by the lack of previous work in both daytime and nighttime remote sensing that specifically takes into consideration the sensor's VA and its impact on the PSF during downscaling.

3. Applications

Implementation of the proposed NTL downscaling techniques holds potential to enhance the utility of nighttime lights data by introducing increased spatial granularity, thereby facilitating the realization of significant practical applications. Enhancing urban studies in fast growing metropolitan areas is an important avenue. In these areas, a variety of stakeholders, such as city administrations, infrastructure planners and business sectors, need comprehensive geospatial data for well-informed urban management and sustainable development projects. To improve the downscaled NTL products for more accurate examination of socioeconomic processes and human settlements, more sophisticated approaches should be investigated, such as integration with fine-resolution demographic information and the use of super-resolution algorithms. The application was mainly focused on showcasing increased spatial detail in diverse urban environments, building on the research's emphasis on VIIRS NTL data. Future research will aim to downscale NTL in rural settings and compare the outcomes with recent, publicly available, SDGSAT-1 NTL data.

6.4 Conclusions

The present study sought to assess urban resilience across the globe and in specific sectors. To this end, a set of innovative techniques for downscaling and using satellite NTL data were adopted and modified. A more sophisticated understanding of urban responses to disruptive events, particularly the COVID-19 pandemic lockdowns, was facilitated by major advances in both spatial resolution and the analytical methodology. The findings of this study are as follows: (1) to enhance the spatial resolution of the NTL data, this thesis adopted and utilized a modern geostatistical approach for the first time. Fine-resolution NTL imagery was produced by the combination of random forest regression with area-to-point Kriging, a technique specially tailored for NTL data. This method offers a more thorough and precise depiction of light emissions during the night in cities, marking a substantial breakthrough in NTL data processing. The increased spatial resolution of the downscaled data is essential for facilitating later assessments of localized urban dynamics and urban studies. (2) The technique created in this thesis successfully reduced the blooming effect, a ubiquitous occurrence in all NTL satellite sensor images. This study is the first to successfully implement a method to deal with this phenomenon during NTL downscaling. The overestimation of light emissions in metropolitan areas was reduced by combining a geostatistical-based methodology with an advanced machine learning algorithm, producing downscaled NTL data that were more accurate and reliable. The validity of the ensuing studies depends on this blooming effect mitigation, especially when socioeconomic phenomena are being proxied at the city level. (3) Leveraging the downscaled and blooming-effect-mitigated NTL data, this thesis conducted the first global-scale assessment of urban resilience at the sector level. By analyzing the differential impacts of COVID-19 lockdowns on various urban functional sectors, this research provides critical insights into the unique vulnerabilities and recovery patterns of urban economies. The integrated methodology, combining a novel downscaling technique with sector-wise resilience assessment, represents a significant contribution to NTL-based urban resilience studies. This approach opens new avenues for targeted policy interventions and resilience planning, offering a more granular and timely understanding of urban dynamics during disruptive events. The increased spatial resolution and accuracy of the processed NTL data, achieved through the methodologies described in the previous paragraphs, were fundamental to the success of this sector-wise analysis, enabling a more nuanced and insightful examination of urban resilience.

References

Abascal, A., Kyba, C., Holker, F., Kuffer, M., Arroyo, H.L., Walczak, K., De Miguel, A.S., Degen, T., Roman, M.O., 2023. Mapping the Invisibles: Global Urban Inequalities through Night Lights. 2023 Jt. Urban Remote Sens. Event, JURSE 2023 1–4. https://doi.org/10.1109/JURSE57346.2023.10144207

Agency, E.S., 2024. Copernicus Global Digital Elevation Model.

Amegavi, G.B., Nursey-Bray, M., Suh, J., 2024. Exploring the realities of urban resilience: Practitioners' perspectives. Int. J. Disaster Risk Reduct. 103, 104313. https://doi.org/10.1016/j.ijdrr.2024.104313

Anderson, K., Ryan, B., Sonntag, W., Kavvada, A., Friedl, L., 2017. Earth observation in service of the 2030 Agenda for Sustainable Development. Geo-Spatial Inf. Sci. 20, 77–96. https://doi.org/10.1080/10095020.2017.1333230

Arifwidodo, S.D., Chandrasiri, O., 2023. Urban green space visitation and mental health wellbeing during COVID-19 in Bangkok, Thailand. Front. Public Heal. 11, 1–8. https://doi.org/10.3389/fpubh.2023.1292154

Atkinson, P.M., 2013. Downscaling in remote sensing. Int. J. Appl. Earth Obs. Geoinf. 22, 106–114. https://doi.org/10.1016/j.jag.2012.04.012

Atkinson, P.M., Pardo-Igúzquiza, E., Chica-Olmo, M., 2008. Downscaling cokriging for super-resolution mapping of continua in remotely sensed images. IEEE Trans. Geosci. Remote Sens. 46, 573–580. https://doi.org/10.1109/TGRS.2007.909952

Bhanarkar, A.D., Purohit, P., Rafaj, P., Amann, M., Bertok, I., Cofala, J., Rao, P.S., Vardhan, B.H., Kiesewetter, G., Sander, R., Schöpp, W., Majumdar, D., Srivastava, A., Deshmukh, S., Kawarti, A., Kumar, R., 2018. Managing future air quality in megacities: Co-benefit assessment for Delhi. Atmos. Environ. 186, 158–177. https://doi.org/10.1016/j.atmosenv.2018.05.026

Bharti, N., Tatem, A.J., 2018. Fluctuations in anthropogenic nighttime lights from satellite imagery for five cities in Niger and Nigeria. Sci. Data 5, 1–9. https://doi.org/10.1038/sdata.2018.256

Borup, D., Christensen, B.J., Mühlbach, N.S., Nielsen, M.S., 2023. Targeting predictors in random forest regression. Int. J. Forecast. 39, 841–868. https://doi.org/10.1016/j.ijforecast.2022.02.010

Bouhennache, R., Bouden, T., Taleb-ahmed, A., 2019. A new spectral index for the extraction of built-up land features from Landsat 8 satellite imagery. Geocarto Int. 34, 1531–1551. https://doi.org/10.1080/10106049.2018.1497094

Bourdin, S., Levratto, N., 2024. The spatial footprint of COVID-19 and local policy answers. Reg. Stud. 58, 255–262. https://doi.org/10.1080/00343404.2023.2242411

Breiman, L., 2001. Random Forests. Mach. Learn. 45, 5–32. https://doi.org/https://doi.org/10.1023/A:1010933404324

Brokamp, C., Jandarov, R., Rao, M.B., LeMasters, G., Ryan, P., 2017. Exposure assessment models for elemental components of particulate matter in an urban environment: A comparison of regression and random forest approaches. Atmos. Environ. 151, 1–11. https://doi.org/10.1016/j.atmosenv.2016.11.066

Brown, J., 2023. MACHISPLIN: Interpolation of noisy multi-variate data using machine learning ensembling.

Bruederle, A., Hodler, R., 2018. Nighttime lights as a proxy for human development at the local level. PLoS One 13, 1–22. https://doi.org/10.1371/journal.pone.0202231

Bu, Xu, Zhang, Zhang, 2019. Night-light Image Restoration Method Based on Night Scattering Model for Luojia 1-01 Satellite. Sensors 19, 3761. https://doi.org/10.3390/s19173761

Bullock, E.L., Woodcock, C.E., Holden, C.E., 2020. Improved change monitoring using an ensemble of time series algorithms. Remote Sens. Environ. 238, 1–53. https://doi.org/10.1016/j.rse.2019.04.018

Büyüközkan, G., Ilıcak, Ö., Feyzioğlu, O., 2022. A review of urban resilience literature. Sustain. Cities Soc. 77. https://doi.org/10.1016/j.scs.2021.103579

Cao, X., Hu, Y., Zhu, X., Shi, F., Zhuo, L., Chen, J., 2019. A simple self-adjusting model for correcting the blooming effects in DMSP-OLS nighttime light images. Remote Sens. Environ. 224, 401–411. https://doi.org/10.1016/j.rse.2019.02.019

Chang, T.C., Tang, J.H., Chan, T.C., 2025. Spatiotemporal impact of urban development on nighttime light intensity and its hotspot distribution. PLoS One 20, 1–15. https://doi.org/10.1371/journal.pone.0325696

Chen, C., Zhao, S., Duan, Z., Qin, Z., 2015. An Improved Spatial Downscaling Procedure for TRMM 3B43 Precipitation Product Using Geographically Weighted Regression. IEEE J. Sel. Top. Appl. Earth Obs. Remote Sens. 8, 4592–4604. https://doi.org/10.1109/JSTARS.2015.2441734

Chen, G., Chen, Q., 2025. Putting Urban Resilience in Geographical Context: The Case of City Regions in Hainan, China, in the Wake of COVID-19 and Beyond. Sustainability 17, 8697. https://doi.org/10.3390/su17198697

Chen, X., Nordhaus, W.D., 2011. Using luminosity data as a proxy for economic statistics. Proc. Natl. Acad. Sci. U. S. A. 108, 8589–8594. https://doi.org/10.1073/pnas.1017031108

Chen, X., Quan, R., 2021. A spatiotemporal analysis of urban resilience to the COVID-19 pandemic in the Yangtze River Delta. Nat. Hazards 106, 829–854. https://doi.org/10.1007/s11069-020-04493-9

Chen, Z., Yu, B., Yang, C., Zhou, Y., Yao, S., Qian, X., Wang, C., Wu, B., Wu, J., 2021. An extended time series (2000-2018) of global NPP-VIIRS-like nighttime light data from a cross-sensor calibration. Earth Syst. Sci. Data 13, 889–906. https://doi.org/10.5194/essd-13-889-2021

Cheng, T., Ma, L., Zhao, Y., Zhao, C., 2024. Large-scale and rapid perception of regional economic resilience from data-driven insights. Int. J. Digit. Earth 17, 1–22.

https://doi.org/10.1080/17538947.2024.2365971

Cheng, Z., Wang, J., Ge, Y., 2022. Mapping monthly population distribution and variation at 1-km resolution across China. Int. J. Geogr. Inf. Sci. 36, 1166–1184. https://doi.org/10.1080/13658816.2020.1854767

Chi, G., Fang, H., Chatterjee, S., Blumenstock, J.E., 2022. Microestimates of wealth for all low- and middle-income countries. Proc. Natl. Acad. Sci. U. S. A. 119, 1–11. https://doi.org/10.1073/pnas.2113658119

Chrysoulakis, N., Ludlow, D., Mitraka, Z., Somarakis, G., Khan, Z., Lauwaet, D., Hooyberghs, H., Feliu, E., Navarro, D., Feigenwinter, C., Holsten, A., Soukup, T., Dohr, M., Marconcini, M., Holt Andersen, B., 2023. Copernicus for urban resilience in Europe. Sci. Rep. 13, 1–16. https://doi.org/10.1038/s41598-023-43371-9

Clevelard, B, R., Cleveland S, William, McRae, E, J., Terpenning, I., 1990. Statistical Model. J. Off. Stat. 6, 3–73.

Cutler, A., Breiman, L., 1994. Archetypal Analysis. Technometrics 36, 338. https://doi.org/10.2307/1269949

D’Esposito, M.R., De Stefano, D., Ragozini, G., 2014. On the use of Multiple Correspondence Analysis to visually explore affiliation networks. Soc. Networks 38, 28–40. https://doi.org/10.1016/j.socnet.2014.01.003

Dascher-Preising, F., Greiner, A., 2023. Monetary-fiscal policy relations in the euro area: The impact on the primary balance. J. Econ. Behav. Organ. 216, 1–9. https://doi.org/10.1016/j.jebo.2023.09.026

Dasgupta, N., 2022. Using satellite images of nighttime lights to predict the economic impact of COVID-19 in India. Adv. Sp. Res. 70, 863–879. https://doi.org/10.1016/j.asr.2022.05.039

Datola, G., 2023. Implementing urban resilience in urban planning: A comprehensive framework for urban resilience evaluation. Sustain. Cities Soc. 98, 104821. https://doi.org/10.1016/j.scs.2023.104821

Diop, S., Asongu, S.A., Nnanna, J., 2021. COVID-19 economic vulnerability and resilience indexes: Global evidence. Int. Soc. Sci. J. 71, 37–50. https://doi.org/10.1111/issj.12276

Du, H., Zhan, W., Zhou, B., Ju, Y., Liu, Z., Middel, A., Huang, K., Zhao, L., Chakraborty, T., Wang, Z., Wang, S., Li, J., Li, L., Huang, F., Ji, Y., Li, X., Li, M., 2025. Exacerbated heat stress induced by urban browning in the Global South. Nat. Cities 2, 157–169. https://doi.org/10.1038/s44284-024-00184-9

Du, W., Zhai, G., Shi, Y., Lu, Y., 2024. Structural resilience disparities in regional city networks under the influence of Typhoon Fitow and COVID-19. Cities 155, 105460. https://doi.org/10.1016/j.cities.2024.105460

Du, Y., Wang, Q., Zhou, J., 2023. How does digital inclusive finance affect economic resilience: Evidence from 285 cities in China. Int. Rev. Financ. Anal. 88, 102709. https://doi.org/10.1016/j.irfa.2023.102709

Ebrahimy, H., Aghighi, H., Azadbakht, M., Amani, M., Mahdavi, S., Matkan, A.A., 2021. Downscaling MODIS Land Surface Temperature Product Using an Adaptive Random Forest Regression Method and Google Earth Engine for a 19-Years Spatiotemporal Trend Analysis over Iran. IEEE J. Sel. Top. Appl. Earth Obs. Remote Sens. 14, 2103–2112. https://doi.org/10.1109/JSTARS.2021.3051422

Egger, D., Edward, M., Shana S. Warren, Ashish, S., Elliott, C., Dean, K., Doug, P., Mushfiq, M., Günther, F., Christopher, U., Michael, W., Johannes, H., Magdalena, L., Susan, A., Paula Lopez-Pena, Salim, B., Macartan, H., Layna, L., Niccoló, M., Andrew, W., Austin, D., Utz, J.P., Tilman, G., Maarten, V., Carolyn, N., Corey, V., 2021. Falling living standards during the COVID-19 crisis: Quantitative evidence from nine developing countries. Sci. Adv. 5, 1–12.

Elmqvist, T., Andersson, E., Frantzeskaki, N., McPhearson, T., Olsson, P., Gaffney, O., Takeuchi, K., Folke, C., 2019. Sustainability and resilience for transformation in the urban century. Nat. Sustain. 2, 267–273. https://doi.org/10.1038/s41893-019-0250-1

Elvidge, C.D., Baugh, K., Zhizhin, M., Hsu, F.C., Ghosh, T., 2017. VIIRS night-time lights. Int. J. Remote Sens. 38, 5860–5879. https://doi.org/10.1080/01431161.2017.1342050

Elvidge, C.D., Baugh, K.E., Anderson, S.J., Sutton, P.C., Ghosh, T., 2012. The Night Light Development Index (NLDI): A spatially explicit measure of human development from satellite data. Soc. Geogr. 7, 23–35. https://doi.org/10.5194/sg-7-23-2012

Elvidge, C.D., Baugh, K.E., Kihn, E.A., Kroehl, H.W., Davis, E.R., 1997. Mapping city lights with nighttime data from the DMSP Operational Linescan System. Photogramm. Eng. Remote Sensing 63, 727–734.

Elvidge, C.D., Cinzano, P., Pettit, D.R., Arvesen, J., Sutton, P., Small, C., Nemani, R., Longcore, T., Rich, C., Safran, J., Weeks, J., Ebener, S., 2007. The nightsat mission concept. Int. J. Remote Sens. 28, 2645–2670. https://doi.org/10.1080/01431160600981525

Elvidge, C.D., Zhizhin, M., Ghosh, T., Hsu, F.C., Taneja, J., 2021. Annual time series of global viirs nighttime lights derived from monthly averages: 2012 to 2019. Remote Sens. 13, 1–14. https://doi.org/10.3390/rs13050922

EOC Download - WSF2019 [WWW Document], n.d. URL https://download.geoservice.dlr.de/WSF2019/ (accessed 7.10.25).

Esri Land Cover [WWW Document], n.d. URL https://livingatlas.arcgis.com/landcover/ (accessed 6.10.23).

Fellnhofer, K., Angelidou, M., Flacke, J., Fontanella, L., Fransz, M., Karanfil, Ö., Kelmali, E., Kiran, S., Kolias, P., Kundu, V., Mataftsi, K., Mone, T., Nasi, G., Orer, H.S., Papageorgiou, M., Papanikolaou, P., Pfeffer, K., Istoriou, T., Plastara, D., Pasmatzi, K., Pozoukidou, G., Prodromidou, A., Roma-Athanasiadou, E., Sakarya, S., Serafini, G.O., Stylianidis, E., Selçuk, S.H., Tavantzis, I., Thomopoulos, N., Tsifodimou, Z.E., Vlemmas, C.M., Xu, T., Kayı, İ., 2025. A large-scale dataset for analysing remote working in urban and rural areas across Europe. Sci. Data 12, 1–13. https://doi.org/10.1038/s41597-025-05972-z

Feng, G., Wang, K., Yin, D., Zou, S., Wang, L., 2020. How to account for endmember variability in spectral mixture analysis of night-time light imagery? Int. J. Remote Sens. 41, 3147–3161. https://doi.org/10.1080/01431161.2019.1699673

Fromhold-Eisebith, M., 2015. Sectoral Resilience: Conceptualizing Industry-Specific Spatial Patterns of Interactive Crisis Adjustment. Eur. Plan. Stud. 23, 1675–1694. https://doi.org/10.1080/09654313.2015.1047329

Ge, Y., Jin, Y., Stein, A., Chen, Y., Wang, Jianghao, Wang, Jinfeng, Cheng, Q., Bai, H., Liu, M., Atkinson, P.M., 2019. Principles and methods of scaling geospatial Earth science data. Earth-Science Rev. 197, 102897. https://doi.org/10.1016/j.earscirev.2019.102897

Genuer, R., Poggi, J.M., Tuleau-Malot, C., 2015. VSURF: An R package for variable selection using random forests. R J. 7, 19–33. https://doi.org/10.32614/rj-2015-018

Geofabrik Download Server [WWW Document], n.d. URL https://download.geofabrik.de/ (accessed 6.10.23).

Georgeson, L., Maslin, M., Poessinouw, M., Howard, S., 2016. Adaptation responses to climate change differ between global megacities. Nat. Clim. Chang. 6, 584–588. https://doi.org/10.1038/nclimate2944

Getis, A., Ord, J.K., 1992. The Analysis of Spatial Association by Use of Distance Statistics. Geogr. Anal. 24, 189–206. https://doi.org/10.1111/j.1538-4632.1992.tb00261.x

Ghosh, T., Anderson, S.J., Elvidge, C.D., Sutton, P.C., 2013. Using nighttime satellite imagery as a proxy measure of human well-being. Sustain. 5, 4988–5019. https://doi.org/10.3390/su5124988

Ghosh, T., Sutton, P., Powell, R., Anderson, S., Elvidge, C.D., 2009. Estimation of Mexico’s informal economy using DMSP nighttime lights data. 2009 Jt. Urban Remote Sens. Event. https://doi.org/10.1109/URS.2009.5137751

Gibson, J., Boe-Gibson, G., 2021. Nighttime lights and county-level economic activity in the United States: 2001 to 2019. Remote Sens. 13. https://doi.org/10.3390/rs13142741

Gibson, J., Olivia, S., Boe-Gibson, G., Li, C., 2021. Which night lights data should we use in economics, and where? J. Dev. Econ. 149, 102602. https://doi.org/10.1016/j.jdeveco.2020.102602

Global Data Lab - Innovative Instruments for Turning Data into Knowledge [WWW Document], n.d. URL https://globaldatalab.org/ (accessed 6.10.23).

Glückler, J., 2007. Economic geography and the evolution of networks. J. Econ. Geogr. 7, 619–634. https://doi.org/10.1093/jeg/lbm023

Gong, P., Li, X., Wang, J., Bai, Y., Chen, B., Hu, T., Liu, X., Xu, B., Yang, J., Zhang, W., Zhou, Y., 2020. Annual maps of global artificial impervious area (GAIA) between 1985 and 2018. Remote Sens. Environ. 236, 111510. https://doi.org/10.1016/j.rse.2019.111510

Gong, Y., Li, X., Li, D., Zhang, X., 2025. Urban recovery patterns after the 2023 Turkey-Syria earthquake revealed by SDGSAT-1 nighttime light data. Remote Sens. Environ. 328. https://doi.org/10.1016/j.rse.2025.114888

Google LLC, 2025. Google Earth Pro (Version 7.3.6).

Goovaerts, P., 2008. Kriging and semivariogram deconvolution in the presence of irregular geographical units. Math. Geosci. 40, 101–128. https://doi.org/10.1007/s11004-007-9129-1

Goovaerts, P., 2006. Geostatistical analysis of disease data: Accounting for spatial support and population density in the isopleth mapping of cancer mortality risk using area-to-point Poisson kriging. Int. J. Health Geogr. 5, 1–31. https://doi.org/10.1186/1476-072X-5-52

Gorelick, N., Hancher, M., Dixon, M., Ilyushchenko, S., Thau, D., Moore, R., 2017. Google Earth Engine: Planetary-scale geospatial analysis for everyone. Remote Sens. Environ. 202, 18–27. https://doi.org/10.1016/j.rse.2017.06.031

Gu, T., Zhao, H., Yue, L., Liu, Y., Guo, J., Tang, J., Zhao, P., 2025. Spatial heterogeneity of urban resilience: Quantifying key determinants by spatial machine learning model embedded in density-structure-function framework. Cities 167, 106305. https://doi.org/10.1016/j.cities.2025.106305

Guo, B., Hu, D., Liu, Y., Zheng, Q., Lin, A., Atkinson, P.M., 2024. Downscaling of nighttime light imagery with a spatially local estimation model using human activity-physical features. Int. J. Appl. Earth Obs. Geoinf. 130, 103924. https://doi.org/10.1016/j.jag.2024.103924

Guo, J., Zhang, F., Zhao, H., Pan, B., Mei, L., 2023. Reconstructing Three-decade Global Fine-Grained Nighttime Light Observations by a New Super-Resolution Framework 1–34. https://doi.org/https://doi.org/10.48550/arXiv.2307.07366

Gurney, K.R., Patarasuk, R., Liang, J., Song, Y., O'keeffe, D., Rao, P., Whetstone, J.R., Duren, R.M., Eldering, A., Miller, C., 2019. The Hestia fossil fuel CO2 emissions data product for the Los Angeles megacity (Hestia-LA). Earth Syst. Sci. Data 11, 1309–1335. https://doi.org/10.5194/essd-11-1309-2019

Hale, T., Angrist, N., Goldszmidt, R., Kira, B., Petherick, A., Phillips, T., Webster, S., Cameron-Blake, E., Hallas, L., Majumdar, S., Tatlow, H., 2021. A global panel database of pandemic policies (Oxford COVID-19 Government Response Tracker). Nat. Hum. Behav. 5, 529–538. https://doi.org/10.1038/s41562-021-01079-8

Han, H., Bai, X., Costanza, R., Dong, L., 2024. The effects of COVID-19 on the resilience of urban life in China. npj Urban Sustain. 4, 1–13. https://doi.org/10.1038/s42949-024-00167-8

Hassankhani, M., Alidadi, M., Sharifi, A., Azhdari, A., 2021. Smart city and crisis management: Lessons for the covid-19 pandemic. Int. J. Environ. Res. Public Health 18. https://doi.org/10.3390/ijerph18157736

Head, A., Manguin, M., Tran, N., Blumenstock, J.E., 2017. Can Human Development be Measured with Satellite Imagery?, in: Proceedings of the Ninth International Conference on Information and Communication Technologies and Development. ACM, New York, NY, USA, pp. 1–11. https://doi.org/10.1145/3136560.3136576

Heuvelink, G.B.M., Webster, R., 2022. Spatial statistics and soil mapping: A blossoming partnership under pressure. Spat. Stat. 50, 100639.

https://doi.org/10.1016/j.spasta.2022.100639

Hu, F., Wei, Z., Zhang, W., Dorjee, D., Meng, L., 2020. A spatial downscaling method for SMAP soil moisture through visible and shortwave-infrared remote sensing data. J. Hydrol. 590, 125360. https://doi.org/10.1016/j.jhydrol.2020.125360

Hu, L., Meng, J., Xiong, C., Fang, W., Yang, J., Liu, M., Bi, J., Ma, Z., 2024. City-level resilience to extreme weather shocks revealed by satellite nighttime lights in China. Sustain. Cities Soc. 101, 105167. https://doi.org/10.1016/j.scs.2023.105167

Hu, M., Huang, Y., 2020. atakrig: An R package for multivariate area-to-area and area-to-point kriging predictions. Comput. Geosci. 139, 104471. https://doi.org/10.1016/j.cageo.2020.104471

Huang, S., Hu, S., Hu, Q., Chen, Q., 2024. Resilience analysis of urban commercial area under the COVID-19 epidemic using night-time light remote sensing data. Ann. GIS 30, 345–366. https://doi.org/10.1080/19475683.2024.2390412

Huang, X., Song, Y., Yang, J., Wang, W., Ren, H., Dong, M., 2022. Toward accurate mapping of 30-m time-series global impervious surface area (GISA). Int. J. Appl. Earth Obs. Geoinf. 109, 102787. https://doi.org/https://doi.org/10.1016/j.jag.2022.102787

Hulley, G., Shivers, S., Wetherley, E., Cudd, R., 2019. New ECOSTRESS and MODIS land surface temperature data reveal fine-scale heat vulnerability in cities: A case study for Los Angeles County, California. Remote Sens. 11, 6–8. https://doi.org/10.3390/rs11182136

Hutengs, C., Vohland, M., 2016. Downscaling land surface temperatures at regional scales with random forest regression. Remote Sens. Environ. 178, 127–141. https://doi.org/10.1016/j.rse.2016.03.006

IEAG, 2014. A World that Counts: Mobilising the Data Revolution for Sustainable Development, Coediciones. Naciones Unidas Comisión Económica para América Latina y el Caribe (CEPAL).

Imperviousness Density 2018 (raster 10 m and 100 m), Europe, 3-yearly — Copernicus Land Monitoring Service [WWW Document], n.d. URL https://land.copernicus.eu/en/products/high-resolution-layer-imperviousness/imperviousness-density-2018 (accessed 7.10.25).

Jasiński, T., 2019. Modeling electricity consumption using nighttime light images and artificial neural networks. Energy 179, 831–842. https://doi.org/10.1016/j.energy.2019.04.221

Jean, N., Burke, M., Xie, M., Davis, W.M., Lobell, D.B., Ermon, S., 2016. Combining satellite imagery and machine learning to predict poverty. Science (80-.). 353, 790–794. https://doi.org/10.1126/science.aaf7894

Jerven, M., 2017. How Much Will a Data Revolution in Development Cost? Forum Dev. Stud. 44, 31–50. https://doi.org/10.1080/08039410.2016.1260050

Jerven, M., 2013. Comparability of GDP estimates in sub-saharan Africa: The effect of revisions in sources and methods since structural adjustment. Rev. Income Wealth 59, 16–36. https://doi.org/10.1111/roiw.12006

Jia, M., Li, X., Gong, Y., Belabbes, S., Dell'Oro, L., 2023. Estimating natural disaster loss using improved daily night-time light data. Int. J. Appl. Earth Obs. Geoinf. 120. https://doi.org/10.1016/j.jag.2023.103359

Jiang, L., Liu, Y., 2024. Dynamic assessment of the COVID-19 lockdown in the Xinjiang region using night-time light remote sensing. Int. J. Digit. Earth 17. https://doi.org/10.1080/17538947.2023.2300317

Jin, Y., Ge, Y., Wang, J., Chen, Y., Heuvelink, G.B.M., Atkinson, P.M., 2018a. Downscaling AMSR-2 soil moisture data with geographically weighted area-to-area regression kriging. IEEE Trans. Geosci. Remote Sens. 56, 2362–2376. https://doi.org/10.1109/TGRS.2017.2778420

Jin, Y., Ge, Y., Wang, J., Heuvelink, G.B.M., Wang, L., 2018b. Geographically weighted area-to-point regression kriging for spatial downscaling in remote sensing. Remote Sens. 10, 1–22. https://doi.org/10.3390/rs10040579

John, E., 1993. The Balance of Nature? Ecological Issues in the Conservation of Species and Communities by Stuart L. Pimm (University of Chicago Press, Chicago and London, 1992, ISBN 0 226 66830 4, 434 pp., SB £21.50/$26.95). Oryx 27, 125–126. https://doi.org/10.1017/s0030605300020731

Kapucu, N., Ge, Y., Rott, E., Isgandar, H., 2024. Urban resilience: Multidimensional perspectives, challenges and prospects for future research. Urban Gov. 4, 162–179. https://doi.org/10.1016/j.ugj.2024.09.003

Kerry, R., Goovaerts, P., Rawlins, B.G., Marchant, B.P., 2012. Disaggregation of legacy soil data using area to point kriging for mapping soil organic carbon at the regional scale. Geoderma 170, 347–358. https://doi.org/10.1016/j.geoderma.2011.10.007

Kopiika, N., Karavias, A., Krassakis, P., Ye, Z., Ninic, J., Shakhovska, N., Argyroudis, S., Mitoulis, S.A., 2025. Rapid post-disaster infrastructure damage characterisation using remote sensing and deep learning technologies: A tiered approach. Autom. Constr. 170, 105955. https://doi.org/10.1016/j.autcon.2024.105955

Kuhn, M., 2008. Building predictive models in R using the caret package. J. Stat. Softw. 28, 1–26. https://doi.org/10.18637/jss.v028.i05

Kyba, C.C.M., Kuester, T., De Miguel, A.S., Baugh, K., Jechow, A., Hölker, F., Bennie, J., Elvidge, C.D., Gaston, K.J., Guanter, L., 2017. Artificially lit surface of Earth at night increasing in radiance and extent. Sci. Adv. 3, 1–8. https://doi.org/10.1126/sciadv.1701528

Kyba, C.C.M., Ruby, A., Kuechly, H.U., Kinzey, B., Miller, N., Sanders, J., Barentine, J., Kleinodt, R., Espey, B., 2021. Direct measurement of the contribution of street lighting to satellite observations of nighttime light emissions from urban areas. Light. Res. Technol. 53, 189–211. https://doi.org/10.1177/1477153520958463

Kyriakidis, P.C., 2004. A geostatistical framework for area-to-point spatial interpolation. Geogr. Anal. 36, 259–289. https://doi.org/10.1111/j.1538-4632.2004.tb01135.x

Kyriakidis, P.C., Yoo, E.H., 2005. Geostatistical prediction and simulation of point values from areal data. Geogr. Anal. 37, 124–151. https://doi.org/10.1111/j.1538-4632.2005.00633.x

Leal Filho, W., Mbah, M.F., Dinis, M.A.P., Trevisan, L.V., de Lange, D., Mishra, A., Rebelatto, B., Ben Hassen, T., Aina, Y.A., 2024. The role of artificial intelligence in the implementation of the UN Sustainable Development Goal 11: Fostering sustainable cities and communities. Cities 150, 105021. https://doi.org/10.1016/j.cities.2024.105021

Lei, Z., Zhou, S., Cheng, P., Xie, Y., 2024. Improved Population Mapping for China Using the 3D Building, Nighttime Light, Points-of-Interest, and Land Use/Cover Data within a Multiscale Geographically Weighted Regression Model. ISPRS Int. J. Geo-Information 13. https://doi.org/10.3390/ijgi13090335

LeSage, J.P., Kelley Pace, R., Lam, N., Campanella, R., Liu, X., 2011. New Orleans business recovery in the aftermath of Hurricane Katrina. J. R. Stat. Soc. Ser. A Stat. Soc. 174, 1007–1027. https://doi.org/10.1111/j.1467-985X.2011.00712.x

Levin, N., Johansen, K., Hacker, J.M., Phinn, S., 2014. A new source for high spatial resolution night time images - The EROS-B commercial satellite. Remote Sens. Environ. 149, 1–12. https://doi.org/10.1016/j.rse.2014.03.019

Levin, N., Kyba, C.C.M., Zhang, Q., Sánchez de Miguel, A., Román, M.O., Li, X., Portnov, B.A., Molthan, A.L., Jechow, A., Miller, S.D., Wang, Z., Shrestha, R.M., Elvidge, C.D., 2020. Remote sensing of night lights: A review and an outlook for the future. Remote Sens. Environ. 237. https://doi.org/10.1016/j.rse.2019.111443

Li, F., Liao, S., Liu, W., Li, F., 2024. Assessment of post-pandemic economic recovery in Beijing , China , using night-time light data. Remote Sens. Lett. 15, 603–613. https://doi.org/10.1080/2150704X.2024.2359098

Li, H., Jing, L., Dou, C., Ding, H., 2024. A Comprehensive Assessment of the Pansharpening of the Nighttime Light Imagery of the Glimmer Imager of the Sustainable Development Science Satellite 1. Remote Sens. 16. https://doi.org/10.3390/rs16020245

Li, H., Wei, Y.D., 2023. COVID-19 , cities and inequality ☆. Appl. Geogr. 160, 103059. https://doi.org/10.1016/j.apgeog.2023.103059

Li, K., Cheng, B., Li, X., Zhang, X., Wang, G., Gao, J., He, Q., Gan, Y., 2024. An Image Fusion Algorithm for Sustainable Development Goals Satellite-1 Night-Time Light Images Based on Optimized Image Stretching and Dual-Domain Fusion. Remote Sens. 16, 1–23. https://doi.org/10.3390/rs16224298

Li, R., Liu, X., Li, X., 2015. Estimation of the PM2.5 Pollution Levels in Beijing Based on Nighttime Light Data from the Defense Meteorological Satellite Program-Operational Linescan System. Atmosphere (Basel). 6, 607–622. https://doi.org/10.3390/atmos6050607

Li, S., Dragicevic, S., Castro, F.A., Sester, M., Winter, S., Coltekin, A., Pettit, C., Jiang, B., Haworth, J., Stein, A., Cheng, T., 2016. Geospatial big data handling theory and methods: A review and research challenges. ISPRS J. Photogramm. Remote Sens. 115, 119–133. https://doi.org/10.1016/j.isprsjprs.2015.10.012

Li, X., Chen, F., Chen, X., 2013. Satellite-observed nighttime light variation as evidence for global armed conflicts. IEEE J. Sel. Top. Appl. Earth Obs. Remote Sens. 6, 2302–2315. https://doi.org/10.1109/JSTARS.2013.2241021

Lin, T., Rybnikova, N., 2023. Changes in the Association between GDP and Night-Time Lights during the COVID-19 Pandemic: A Subnational-Level Analysis for the US. Geomatics 3, 156–173. https://doi.org/10.3390/geomatics3010008

Liu, C., Zhang, Q., Luo, H., Qi, S., Tao, S., Xu, H., Yao, Y., 2019. An efficient approach to capture continuous impervious surface dynamics using spatial-temporal rules and dense Landsat time series stacks. Remote Sens. Environ. 229, 114–132. https://doi.org/10.1016/j.rse.2019.04.025

Liu, J., Lin, Z., Chau, K.W., Shi, Y., Yang, L., 2024. Urban resilience in face of the pandemic: Tracing changes in public events before, amid and after the fifth wave of COVID-19 in Hong Kong. Cities 147, 104827. https://doi.org/10.1016/j.cities.2024.104827

Liu, R., Li, X., Zhang, Z., 2024. Urban Resilience of Large Public Health Events Based on NPP-VIIRS Nighttime Light Images: A Case Study of 35 Large Cities in China. Sustainability 16, 7483. https://doi.org/10.3390/su16177483

Liu, S., Zhao, X., Zhang, F., Qiu, A., Chen, L., Huang, J., Chen, S., Zhang, S., 2022. Spatial Downscaling of NPP-VIIRS Nighttime Light Data Using Multiscale Geographically Weighted Regression and Multi-Source Variables. Remote Sens. 14. https://doi.org/10.3390/rs14246400

Liu, W., Zhou, J., Li, X., Zheng, H., Liu, Y., 2024. Urban resilience assessment and its spatial correlation from the multidimensional perspective: A case study of four provinces in North-South Seismic Belt, China. Sustain. Cities Soc. 101, 105109. https://doi.org/10.1016/j.scs.2023.105109

Liu, X., Li, X., 2023. Luojia nighttime light data with a 130m spatial resolution providing a better measurement of gridded anthropogenic heat flux than VIIRS. Sustain. Cities Soc. 94, 104565. https://doi.org/10.1016/j.scs.2023.104565

Liu, X.H., Kyriakidis, P.C., Goodchild, M.F., 2008. Population-density estimation using regression and area-to-point residual kriging. Int. J. Geogr. Inf. Sci. 22, 431–447. https://doi.org/10.1080/13658810701492225

Liu, Y., Liu, W., Zhang, X., Lin, Y., Zheng, G., Zhao, Z., Cheng, H., Gross, L., Li, X., Wei, B., Su, F., 2023. Nighttime light perspective in urban resilience assessment and spatiotemporal impact of COVID-19 from January to June 2022 in mainland China. Urban Clim. 50, 101591. https://doi.org/10.1016/j.uclim.2023.101591

Liu, Z., Fang, C., Liao, X., Fan, R., Sun, B., Mu, X., 2023. Adaptation and adaptability: Deciphering urban resilience from the evolutionary perspective. Environ. Impact Assess. Rev. 103, 107266. https://doi.org/10.1016/j.eiar.2023.107266

Liu, Z., Wang, Y., Huang, X., Zhang, Z., Lai, Q., Li, M., 2024. Assessment of national economic repercussions from Shanghai’s COVID-19 lockdown. Humanit. Soc. Sci. Commun. 11, 1579. https://doi.org/10.1057/s41599-024-04100-3

Lowe, M., Bell, S., Briggs, J., McMillan, E., Morley, M., Grenfell, M., Sweeting, D., Whitten, A., Jordan, N., 2024. A research-based, practice-relevant urban resilience framework for local government. Local Environ. 29, 886–901.

https://doi.org/10.1080/13549839.2024.2318571

Lu, S., Xiao, Y., Lu, Y., Lin, J., 2025. Spatialization of electricity consumption by combining high-resolution nighttime light remote sensing and urban functional zoning information. Geo-Spatial Inf. Sci. 28, 527–540. https://doi.org/10.1080/10095020.2024.2356757

Lu, T., Zhang, W., 2025. Delineating Urban High–Risk Zones of Disease Transmission: Applying Tensor Decomposition to Trajectory Big Data. ISPRS Int. J. Geo-Information 14, 1–24. https://doi.org/10.3390/ijgi14080285

Ma, S., Li, S., Zhang, J., 2023. Spatial and deep learning analyses of urban recovery from the impacts of COVID-19. Sci. Rep. 13, 1–14. https://doi.org/10.1038/s41598-023-29189-5

Ma, X., Chen, X., Du, Y., Zhu, X., Dai, Y., Li, X., Zhang, R., Wang, Y., 2022. Evaluation of Urban Spatial Resilience and Its Influencing Factors: Case Study of the Harbin–Changchun Urban Agglomeration in China. Sustainability 14, 2899. https://doi.org/10.3390/su14052899

Malik, K., Kumar, D., Perissin, D., Pradhan, B., 2022. Estimation of ground subsidence of New Delhi, India using PS-InSAR technique and multi-sensor radar data. Adv. Sp. Res. 69, 1863–1882. https://doi.org/10.1016/j.asr.2021.08.032

Mård, J., Di Baldassarre, G., Mazzoleni, M., 2018. Nighttime light data reveal how flood protection shapes human proximity to rivers. Sci. Adv. 4, 1–7. https://doi.org/10.1126/sciadv.aar5779

Marlier, M.E., Jina, A.S., Kinney, P.L., DeFries, R.S., 2016. Extreme Air Pollution in Global Megacities. Curr. Clim. Chang. Reports 2, 15–27. https://doi.org/10.1007/s40641-016-0032-z

Marty, R., Stefanini Vicente, G., 2025. blackmarbler: Black Marble Data and Statistics.

Menoni, S., Galderisi, A., Carrion, D., 2024. Cross-Sectoral and Multilevel Dimensions of Risk and Resilience Management in Urban Areas Enabled by Geospatial Data Processing. Sustainability 16, 26. https://doi.org/https://doi.org/10.3390/ su16198712

Middya, A.I., Roy, S., 2021. Geographically varying relationships of COVID-19 mortality with different factors in India. Sci. Rep. 11, 1–12. https://doi.org/10.1038/s41598-021-86987-5

Mokhtari, Z., Bergantino, A.S., Intini, M., Elia, M., Buongiorno, A., Giannico, V., Sanesi, G., Lafortezza, R., 2025. Nighttime light extent and intensity explain the dynamics of human activity in coastal zones. Sci. Rep. 15, 1–12. https://doi.org/10.1038/s41598-025-85917-z

Naikoo, M.W., Rihan, M., Ishtiaque, M., Shahfahad, 2020. Analyses of land use land cover (LULC) change and built-up expansion in the suburb of a metropolitan city: Spatio-temporal analysis of Delhi NCR using landsat datasets. J. Urban Manag. 9, 347–359. https://doi.org/10.1016/j.jum.2020.05.004

Nijman, J., 2010. A study of space in Mumbai's slums. Tijdschr. voor Econ. en Soc. Geogr. 101, 4–17. https://doi.org/10.1111/j.1467-9663.2009.00576.x

OECD, 2021, 2020. COVID-19 and the retail sector: impact and policy responses, Tackling

Coronavirus, OECD Policy Responses to Coronavirus (COVID-19). https://doi.org/10.1787/371d7599-en

Omar, M.A., Inaba, K., 2020. Does financial inclusion reduce poverty and income inequality in developing countries? A panel data analysis. J. Econ. Struct. 9. https://doi.org/10.1186/s40008-020-00214-4

OpenStreetMap [WWW Document], n.d. URL https://www.openstreetmap.org/#map=19/40.421861/-3.697758 (accessed 7.10.25).

ORNL LandScan Viewer - Oak Ridge National Laboratory [WWW Document], n.d. URL https://landscan.ornl.gov/ (accessed 7.10.25).

Oshiro, T.M., Perez, P.S., Baranauskas, J.A., 2012. How Many Trees in a Random Forest?, in: Lecture Notes in Artificial Intelligence (Subseries of Lecture Notes in Computer Science). pp. 154–168. https://doi.org/10.1007/978-3-642-31537-4_13

Paprotny, D., Mengel, M., 2023. Population, land use and economic exposure estimates for Europe at 100 m resolution from 1870 to 2020. Sci. Data 10, 372. https://doi.org/10.1038/s41597-023-02282-0

Pardo-Igúzquiza, E., Chica-Olmo, M., Atkinson, P.M., 2006. Downscaling cokriging for image sharpening. Remote Sens. Environ. 102, 86–98. https://doi.org/10.1016/j.rse.2006.02.014

Pardo-Iguzquiza, E., Rodríguez-Galiano, V.F., Chica-Olmo, M., Atkinson, P.M., 2011. Image fusion by spatially adaptive filtering using downscaling cokriging. ISPRS J. Photogramm. Remote Sens. 66, 337–346. https://doi.org/10.1016/j.isprsjprs.2011.01.001

Paris, R.G., Rienow, A., 2025. Shedding light on local development: Unveiling spatial dynamics from infrastructure implementation through nighttime lights in the Nacala corridor, Mozambique. Remote Sens. Appl. Soc. Environ. 37, 101388. https://doi.org/10.1016/j.rsase.2024.101388

Park, N., Kim, Y., Kwak, G.-H., 2019. An overview of theoretical and practical issues in spatial downscaling of coarse resolution satellite-derived products. Korean J. Remote Sens. 35, 589–607.

Pereira, O.J.R., Melfi, A.J., Montes, C.R., Lucas, Y., 2018. Downscaling of ASTER thermal images based on geographically weighted regression kriging. Remote Sens. 10, 1–20. https://doi.org/10.3390/rs10040633

Pérez-Sindín, X.S., Chen, T.H.K., Prishchepov, A. V., 2021. Are night-time lights a good proxy of economic activity in rural areas in middle and low-income countries? Examining the empirical evidence from Colombia. Remote Sens. Appl. Soc. Environ. 24. https://doi.org/10.1016/j.rsase.2021.100647

Pesaresi, M., Politis, P., 2022. GHS-BUILT-S R2022A - GHS built-up surface grid , derived from Sentinel2 composite and Landsat , multitemporal (1975-. Eur. Comm. Jt. Res. Cent. https://doi.org/10.2905/D07D81B4-7680-4D28-B896-583745C27085

Pesaresi, M., Schiavina, M., Politis, P., Freire, S., Krasnodębska, K., Uhl, J.H., Carioli, A., Corbane, C., Dijkstra, L., Florio, P., Friedrich, H.K., Gao, J., Leyk, S., Lu, L., Maffenini, L., Mari-Rivero, I., Melchiorri, M., Syrris, V., Van Den Hoek, J., Kemper, T., 2024. Advances on the global human settlement layer by joint assessment of earth observation and population survey data. Int. J. Digit. Earth 17, 1–54. https://doi.org/10.1080/17538947.2024.2390454

Popandopulo, G., Illarionova, S., Shadrin, D., Evteeva, K., Sotiriadi, N., Burnaev, E., 2023. Flood Extent and Volume Estimation Using Remote Sensing Data. Remote Sens. 15, 1–19. https://doi.org/10.3390/rs15184463

Probst, P., Boulesteix, A.L., 2018. To tune or not to tune the number of trees in random forest. J. Mach. Learn. Res. 18, 1–8. https://doi.org/https://doi.org/10.48550/arXiv.1705.05654

Pu, R., 2021. Assessing scaling effect in downscaling land surface temperature in a heterogenous urban environment. Int. J. Appl. Earth Obs. Geoinf. 96, 102256. https://doi.org/10.1016/j.jag.2020.102256

Qiang, Y., Huang, Q., Xu, J., 2020. Observing community resilience from space : Using nighttime lights to model economic disturbance and recovery pattern in natural disaster. Sustain. Cities Soc. 57, 102115. https://doi.org/10.1016/j.scs.2020.102115

R Core Team, 2025. R: A Language and Environment for Statistical Computing.

Rao, F., Zhao, H., Han, S.S., Kong, Y., Lai, D., Lu, T., 2024. Transformative resilience of Wuhan ' s city-center main streets in the post-COVID era. Nat. Cities 1, 378–389. https://doi.org/https://doi.org/10.1038/s44284-024-00063-3

Reid, A.J., Brooks, J.L., Dolgova, L., Laurich, B., Sullivan, B.G., Szekeres, P., Wood, S.L.R., Bennett, J.R., Cooke, S.J., 2017. Post-2015 Sustainable Development Goals still neglecting their environmental roots in the Anthropocene. Environ. Sci. Policy 77, 179–184. https://doi.org/10.1016/j.envsci.2017.07.006

Ribeiro, P.J.G., Pena Jardim Gonçalves, L.A., 2019. Urban resilience: A conceptual framework. Sustain. Cities Soc. 50. https://doi.org/10.1016/j.scs.2019.101625

Román, M.O., Stokes, E.C., 2015. Holidays in lights: Tracking cultural patterns in demand for energy services. Earth's Futur. 3, 182–205. https://doi.org/10.1002/2014EF000285

Román, M.O., Wang, Z., Sun, Q., Kalb, V., Miller, S.D., Molthan, A., Schultz, L., Bell, J., Stokes, E.C., Pandey, B., Seto, K.C., Hall, D., Oda, T., Wolfe, R.E., Lin, G., Golpayegani, N., Devadiga, S., Davidson, C., Sarkar, S., Praderas, C., Boller, R., Stevens, J., Ramos, O.M., Padilla, E., Alonso, J., Detrés, Y., Armstrong, R., Miranda, I., Conte, Y., Marrero, N., Macmanus, K., Esch, T., Masuoka, E.J., 2018. NASA ' s Black Marble nighttime lights product suite. Remote Sens. Environ. 210, 113–143. https://doi.org/https://doi.org/10.1016/j.rse.2018.03.017

Roshan, G., Ghanghermeh, A., Sarli, R., Grab, S.W., 2024. Environmental impacts of shifts in surface urban heat island, emissions, and nighttime light during the Russia–Ukraine war in Ukrainian cities. Environ. Sci. Pollut. Res. 31, 45246–45263. https://doi.org/10.1007/s11356-024-34050-x

Rowe, F., Robinson, C., Patias, N., 2022. Sensing global changes in local patterns of energy consumption in cities during the early stages of the COVID-19 pandemic. Cities 129, 103808. https://doi.org/10.1016/j.cities.2022.103808

Rubinton, H., Isaacson, M., 2023. Income Segregation and Income Inequality, Economic Synopses. https://doi.org/10.20955/es.2023.5

Sajjad, M., Chan, J.C.L., Chopra, S.S., 2021. Rethinking disaster resilience in high-density cities: Towards an urban resilience knowledge system. Sustain. Cities Soc. 69, 102850. https://doi.org/10.1016/j.scs.2021.102850

Samsudin, S.H., Shafri, H.Z.M., Hamedianfar, A., 2016. Development of spectral indices for roofing material condition status detection using field spectroscopy and WorldView-3 data. J. Appl. Remote Sens. 10, 025021. https://doi.org/10.1117/1.jrs.10.025021

Sánchez, A.M., Cuadrado-Roura, J.R., 2024. Sectoral–regional resilience and productive specialization: a comparison among the last three crises. Ann. Reg. Sci. 73, 61–86. https://doi.org/10.1007/s00168-024-01261-6

Setyadi, A., Pawirosumarto, S., Damaris, A., 2025. Toward a Resilient and Sustainable Supply Chain: Operational Responses to Global Disruptions in the Post-COVID-19 Era. Sustain. 17, 1–39. https://doi.org/10.3390/su17136167

Sharifi, A., 2019. Urban form resilience: A meso-scale analysis. Cities 93, 238–252. https://doi.org/10.1016/j.cities.2019.05.010

Stathakis, D., Baltas, P., 2018. Seasonal population estimates based on night-time lights. Comput. Environ. Urban Syst. 68, 133–141. https://doi.org/10.1016/j.compenvurbsys.2017.12.001

Steele, J.E., Sundsøy, P.R., Pezzulo, C., Alegana, V.A., Bird, T.J., Blumenstock, J., Bjelland, J., Engø-Monsen, K., De Montjoye, Y.A., Iqbal, A.M., Hadiuzzaman, K.N., Lu, X., Wetter, E., Tatem, A.J., Bengtsson, L., 2017. Mapping poverty using mobile phone and satellite data. J. R. Soc. Interface 14. https://doi.org/10.1098/rsif.2016.0690

Stokes, E.C., Román, M.O., 2022. Tracking COVID-19 urban activity changes in the Middle East from nighttime lights. Sci. Rep. 12, 1–13. https://doi.org/10.1038/s41598-022-12211-7

Stokes, E.C., Román, M.O., Wang, Z., Kyba, C.C.M., Miller, S.D., Storch, T., Gurney, K.R., 2021. Retired satellites: A chance to shed light. Science (80-.). 373, 1451–1452. https://doi.org/10.1126/science.abl9965

Stokes, E.C., Seto, K.C., 2019. Characterizing urban infrastructural transitions for the Sustainable Development Goals using multi-temporal land, population, and nighttime light data. Remote Sens. Environ. 234, 111430. https://doi.org/10.1016/j.rse.2019.111430

Sun, M., Yan, S., Cao, T., Zhang, J., 2024. The impact of COVID-19 pandemic on the world's major economies: based on a multi-country and multi-sector CGE model. Front. Public Heal. 12. https://doi.org/10.3389/fpubh.2024.1338677

Takoutsing, B., Heuvelink, G.B.M., 2022. Comparing the prediction performance, uncertainty quantification and extrapolation potential of regression kriging and random forest while accounting for soil measurement errors. Geoderma 428, 116192. https://doi.org/10.1016/j.geoderma.2022.116192

Tang, K., Zhu, H., Ni, P., 2021. Spatial downscaling of land surface temperature over heterogeneous regions using random forest regression considering spatial features. Remote Sens. 13. https://doi.org/10.3390/rs13183645

Tatem, A.J., 2017. WorldPop, open data for spatial demography. Sci. Data 4, 2–5. https://doi.org/10.1038/sdata.2017.4

Ten, G.K., Tafere, H.K., Newhouse, D., Pape, U., 2024. How well can real-time indicators track the economic impacts of a crisis like COVID-19? Dev. Policy Rev. 1–25. https://doi.org/10.1111/dpr.12797

Tiedmann, H.R., Spearing, L.A., Castellanos, S., Stephens, K.K., Sela, L., Faust, K.M., 2023. Tracking the post-disaster evolution of water infrastructure resilience: A study of the 2021 Texas winter storm. Sustain. Cities Soc. 91, 104417. https://doi.org/10.1016/j.scs.2023.104417

Tziokas, N., Zhang, C., Drolias, G.C., Atkinson, P.M., 2023. Downscaling satellite night-time lights imagery to support within-city applications using a spatially non-stationary model. Int. J. Appl. Earth Obs. Geoinf. 122, 103395. https://doi.org/10.1016/j.jag.2023.103395

Tziokas, N., Zhang, C., Tziokas, A., Wang, Q., Atkinson, P.M., 2024. Downscaling Satellite Night-Time Light Imagery While Addressing the Blooming Effect. IEEE J. Sel. Top. Appl. Earth Obs. Remote Sens. 17, 13678–13693. https://doi.org/10.1109/JSTARS.2024.3429244

Vinayak, B., Lee, H.S., Gedem, S., 2021. Prediction of land use and land cover changes in Mumbai city, India, using remote sensing data and a multilayer perceptron neural network-based markov chain model. Sustainability 13, 471. https://doi.org/10.3390/su13020471

Wang, C., Chen, Z., Yu, B., Wu, B., Wei, Y., Yuan, Y., Liu, S., Tu, Y., Li, Y., Wu, J., 2024. Impacts of COVID-19 on urban networks: Evidence from a novel approach of flow measurement based on nighttime light data. Comput. Environ. Urban Syst. 107, 102056. https://doi.org/10.1016/j.compenvurbsys.2023.102056

Wang, L., Tan, W., Xu, H., He, H., Chen, N., Li, D., Chapman, M.A., Li, J., 2022. Deep Learning-Based Method To Extend the Time Series of Global Annual Viirs-Like Nighttime Light Data. Int. Arch. Photogramm. Remote Sens. Spat. Inf. Sci. - ISPRS Arch. 43, 73–78. https://doi.org/10.5194/isprs-archives-XLIII-B1-2022-73-2022

Wang, Q., Shi, W., Atkinson, P.M., 2016a. Area-to-point regression kriging for pan-sharpening. ISPRS J. Photogramm. Remote Sens. 114, 151–165. https://doi.org/10.1016/j.isprsjprs.2016.02.006

Wang, Q., Shi, W., Atkinson, P.M., Pardo-Igúzquiza, E., 2016b. A new geostatistical solution to remote sensing image downscaling. IEEE Trans. Geosci. Remote Sens. 54, 386–396. https://doi.org/10.1109/TGRS.2015.2457672

Wang, Q., Shi, W., Atkinson, P.M., Zhao, Y., 2015. Downscaling MODIS images with area-to-point regression kriging. Remote Sens. Environ. 166, 191–204. https://doi.org/10.1016/j.rse.2015.06.003

Wang, Q., Shi, W., Li, Z., Atkinson, P.M., 2016c. Fusion of Sentinel-2 images. Remote Sens. Environ. 187, 241–252. https://doi.org/10.1016/j.rse.2016.10.030

Wang, Q., Tang, Y., Atkinson, P.M., 2020. The effect of the point spread function on downscaling continua. ISPRS J. Photogramm. Remote Sens. 168, 251–267. https://doi.org/10.1016/j.isprsjprs.2020.08.016

Wang, Q., Zhang, Y., Onojeghuo, A.O., Zhu, X., Atkinson, P.M., 2017. Enhancing spatio-temporal fusion of MODIS and Landsat data by incorporating 250 m MODIS data. IEEE J. Sel. Top. Appl. Earth Obs. Remote Sens. 10, 4116–4123. https://doi.org/10.1109/JSTARS.2017.2701643

Wang, W., Gurgone, A., Martínez, H., Barbieri Góes, M.C., Gallo, E., Kerényi, Á., Turco, E.M., Coburger, C., Andrade, P.D.S., 2022. COVID-19 Mortality and Economic Losses: The Role of Policies and Structural Conditions. J. Risk Financ. Manag. 15. https://doi.org/10.3390/jrfm15080354

Wang, Z., Bui, Q., Zhang, B., Nawarathna, C.L.K., Mombeuil, C., 2021. The nexus between renewable energy consumption and human development in BRICS countries: The moderating role of public debt. Renew. Energy 165, 381–390. https://doi.org/10.1016/j.renene.2020.10.144

Wang, Z., Hao, X., Du, X., Ding, H., Xie, Z., 2024. Measurement of economic resilience under the COVID-19 based on nighttime light remote sensing: Case of Hubei province. PLoS One 19, e0307613. https://doi.org/10.1371/journal.pone.0307613

Watmough, G.R., Atkinson, P.M., Hutton, C.W., 2013. Predicting socioeconomic conditions from satellite sensor data in rural developing countries: A case study using female literacy in Assam, India. Appl. Geogr. 44, 192–200. https://doi.org/10.1016/j.apgeog.2013.07.023

Watmough, G.R., Brockington, D., Marcinko, C.L.J., Hall, O., Pritchard, R., Berchoux, T., Gibson, L., Delamonica, E., Boyd, D., Mlambo, R., Ó Héir, S., Seth, S., 2025. A perspective on the interpretability of poverty maps derived from Earth Observation. Sci. Remote Sens. 12. https://doi.org/10.1016/j.srs.2025.100298

Watmough, G.R., Marcinko, C.L.J., 2024. EO for Poverty: Developing Metrics to Support Decision Making Using Earth Observation, in: Comprehensive Remote Sensing. Elsevier, pp. 1–22. https://doi.org/10.1016/B978-0-443-13220-9.00033-0

Watmough, G.R., Marcinko, C.L.J., 2021. Chapter 11 - Towards achieving the UNs data revolution: combining earth observation and socioeconomic data for geographic targeting of resources for the sustainable development goals, in: Dunn, J., Balaprakash, P. (Eds.), Data Science Applied to Sustainability Analysis. Elsevier, pp. 229–254. https://doi.org/https://doi.org/10.1016/B978-0-12-817976-5.00012-7

Watmough, G.R., Marcinko, C.L.J., Sullivan, C., Tschirhart, K., Mutuo, P.K., Palm, C.A., Svenning, J.C., 2019. Socioecologically informed use of remote sensing data to predict rural household poverty. Proc. Natl. Acad. Sci. U. S. A. 116, 1213–1218. https://doi.org/10.1073/pnas.1812969116

Weber, E., Moehl, J., Weston, S., Rose, A., Brelsford, C., Hauser, T., 2022. LandScan USA 2021. https://doi.org/10.48690/1527701

Williams, B.A., Venter, O., Allan, J.R., Atkinson, S.C., Rehbein, J.A., Ward, M., Di Marco, M., Grantham, H.S., Ervin, J., Goetz, S.J., Hansen, A.J., Jantz, P., Pillay, R., Rodríguez-Buriticá, S., Supples, C., Virnig, A.L.S., Watson, J.E.M., 2020. Change in Terrestrial Human Footprint Drives Continued Loss of Intact Ecosystems. One Earth 3, 371–382. https://doi.org/10.1016/j.oneear.2020.08.009

World Cities 2024 – GaWC [WWW Document], n.d. URL https://gawc.lboro.ac.uk/gawc-worlds/the-world-according-to-gawc/world-cities-2024/#site-header (accessed 3.24.25).

Wright, M.N., Ziegler, A., 2017. ranger : A Fast Implementation of Random Forests for High Dimensional Data in C++ and R. J. Stat. Softw. 77. https://doi.org/10.18637/jss.v077.i01

Wu, J., Tu, Y., Chen, Z., Yu, B., 2022. Analyzing the Spatially Heterogeneous Relationships between Nighttime Light Intensity and Human Activities across Chongqing, China. Remote Sens. 14. https://doi.org/10.3390/rs14225695

Wu, J., Zhang, Z., Yang, X., Li, X., 2021. Analyzing pixel-level relationships between luojia 1-01 nighttime light and urban surface features by separating the pixel blooming effect. Remote Sens. 13, 1–21. https://doi.org/10.3390/rs13234838

Wu, Y., Shi, K., Li, X., Ru, Y., 2025a. Recovery of economic activities in China uncovered by remotely sensed nighttime light data under the pandemic new normal. Appl. Geogr. 175. https://doi.org/10.1016/j.apgeog.2025.103506

Wu, Y., Shi, K., Li, X., Ru, Y., 2025b. Recovery of economic activities in China uncovered by remotely sensed nighttime light data under the pandemic new normal. Appl. Geogr. 175. https://doi.org/10.1016/j.apgeog.2025.103506

Xu, G., Xiu, T., Li, X., Liang, X., Jiao, L., 2021. Lockdown induced night-time light dynamics during the COVID-19 epidemic in global megacities. Int. J. Appl. Earth Obs. Geoinf. 102. https://doi.org/10.1016/j.jag.2021.102421

Xu, H., Chen, J., He, G., Lin, Z., Bai, Y., Ren, M., Zhang, H., Yin, H., Liu, F., 2024. Immediate assessment of forest fire using a novel vegetation index and machine learning based on multi-platform, high temporal resolution remote sensing images. Int. J. Appl. Earth Obs. Geoinf. 134, 104210. https://doi.org/10.1016/j.jag.2024.104210

Xu, J., Qiang, Y., 2021. Spatial Assessment of Community Resilience from 2012 Hurricane Sandy Using Nighttime Light. Remote Sens. 13, 4128. https://doi.org/10.3390/rs13204128

Xu, J., Zhang, F., Jiang, H., Hu, H., Zhong, K., Jing, W., Yang, J., Jia, B., 2020. Downscaling Aster Land Surface Temperature over Urban Areas with Machine Learning-Based Area-To-Point Regression Kriging. Remote Sens. 12, 1082. https://doi.org/10.3390/rs12071082

Xu, W., Wu, Z., Lin, W., Xu, G., 2024. Spatial Downscaling of NPP/VIIRS DNB Nighttime Light Data Based on Deep Learning. IEEE J. Sel. Top. Appl. Earth Obs. Remote Sens. 17, 1–12. https://doi.org/10.1109/jstars.2024.3454093

Yao, Y., Guo, Z., Huang, X., Ren, S., Hu, Y., Dong, A., Guan, Q., 2023. Gauging urban resilience in the United States during the COVID-19 pandemic via social network analysis. Cities 138, 104361. https://doi.org/10.1016/j.cities.2023.104361

Ye, Y., Huang, L., Zheng, Q., Liang, C., Dong, B., Deng, J., Han, X., 2021. A feasible framework to downscale NPP-VIIRS nighttime light imagery using multi-source spatial variables and geographically weighted regression. Int. J. Appl. Earth Obs. Geoinf. 104, 102513. https://doi.org/10.1016/j.jag.2021.102513

Yoneoka, D., Eguchi, A., Nomura, S., Kawashima, T., Tanoue, Y., Hashizume, M., Suzuki, M., 2024. Indirect and direct effects of nighttime light on COVID-19 mortality using satellite image mapping approach. Sci. Rep. 14, 1–11. https://doi.org/10.1038/s41598-024-75484-0

Yonzan, N., Mahler, D.G., Lakner, C., 2022. The Impact of COVID-19 on Global Inequality and Poverty, Policy Research Working Papers. World Bank. https://doi.org/10.1596/1813-9450-10198

Yoo, E.H., Kyriakidis, P.C., 2006. Area-to-point Kriging with inequality-type data. J. Geogr. Syst. 8, 357–390. https://doi.org/10.1007/s10109-006-0036-7

Yoruk, D.E., Yoruk, E., Figueiredo, P.N., Johnston, A., 2023. Sectoral resilience through learning in networks and GVCs: A historical perspective on the food-processing and clothing industries in Poland. Technol. Forecast. Soc. Change 192, 122535. https://doi.org/10.1016/j.techfore.2023.122535

Yuan, Z., Hu, W., 2023. Urban resilience to socioeconomic disruptions during the COVID-19 pandemic: Evidence from China. Int. J. Disaster Risk Reduct. 91, 103670. https://doi.org/10.1016/j.ijdrr.2023.103670

Ženka, J., Chreneková, M., Kokešová, L., Svetlíková, V., 2021. Industrial structure and economic resilience of non-metropolitan regions: An empirical base for the smart specialization policies. Land 10. https://doi.org/10.3390/land10121335

Zhang, H., Liu, X., Xie, Y., Gou, Q., Li, R., Qiu, Y., Hu, Y., Huang, B., 2022. Assessment and Improvement of Urban Resilience to Flooding at a Subdistrict Level Using Multi-Source Geospatial Data: Jakarta as a Case Study. Remote Sens. 14. https://doi.org/10.3390/rs14092010

Zhang, L., Wu, S., Liang, M., Jing, H., Shi, S., Zhu, Y., Ye, Y., Huang, S., Meng, F., Du, Z., 2024. A Downscaling Framework for Urban Nighttime Light Based on Multifactor Geographically Neural Network Weighted Regression. IEEE Trans. Geosci. Remote Sens. 62, 1–16. https://doi.org/10.1109/TGRS.2024.3416211

Zhang, X., Gibson, J., 2022. Using Multi-Source Nighttime Lights Data to Proxy for County-Level Economic Activity in China from 2012 to 2019. Remote Sens. 14. https://doi.org/10.3390/rs14051282

Zhang, Yihang, Atkinson, P.M., Ling, F., Foody, G.M., Wang, Q., Ge, Y., Li, X., Du, Y., 2021. Object-Based Area-to-Point Regression Kriging for Pansharpening. IEEE Trans. Geosci. Remote Sens. 59, 8599–8614. https://doi.org/10.1109/TGRS.2020.3041724

Zhang, Yatao, Li, X., Wang, S., Yao, Y., Li, Q., Tu, W., Zhao, Hongfang, Zhao, Hui, Feng, K., Sun, L., Hubacek, K., 2021. A global North-South division line for portraying urban development. iScience 24, 102729. https://doi.org/10.1016/j.isci.2021.102729

Zhang, Y., Song, S., Li, X., Gao, S., Raubal, M., 2024a. Leveraging context-adjusted nighttime light data for socioeconomic explanations of global urban resilience. Sustain. Cities Soc.

114, 105739. https://doi.org/10.1016/j.scs.2024.105739

Zhang, Y., Song, S., Li, X., Gao, S., Raubal, M., 2024b. Leveraging context-adjusted nighttime light data for socioeconomic explanations of global urban resilience. Sustain. Cities Soc. 114, 105739. https://doi.org/10.1016/j.scs.2024.105739

Zhao, M., Zhou, Y., Li, Xuecao, Cao, W., He, C., Yu, B., Li, Xi, Elvidge, C.D., Cheng, W., Zhou, C., 2019. Applications of satellite remote sensing of nighttime light observations: Advances, challenges, and perspectives. Remote Sens. 11, 1–35. https://doi.org/10.3390/rs11171971

Zhao, N., Liu, Y., Hsu, F.C., Samson, E.L., Letu, H., Liang, D., Cao, G., 2020. Time series analysis of VIIRS-DNB nighttime lights imagery for change detection in urban areas: A case study of devastation in Puerto Rico from hurricanes Irma and Maria. Appl. Geogr. 120, 102222. https://doi.org/10.1016/j.apgeog.2020.102222

Zhao, Q., Yu, L., 2025. Advancing Sustainable Development Goals through Earth Observation Satellite Data: Current Insights and Future Directions. J. Remote Sens. (United States) 5, 1–16. https://doi.org/10.34133/remotesensing.0403

Zheng, Q., Seto, K.C., Zhou, Y., You, S., Weng, Q., 2023. Nighttime light remote sensing for urban applications: Progress, challenges, and prospects. ISPRS J. Photogramm. Remote Sens. 202, 125–141. https://doi.org/10.1016/j.isprsjprs.2023.05.028

Zheng, Q., Weng, Q., Wang, K., 2020. Correcting the Pixel Blooming Effect (PiBE) of DMSP-OLS nighttime light imagery. Remote Sens. Environ. 240, 111707. https://doi.org/10.1016/j.rse.2020.111707

Zhong, Y., Hong, S., Wei, Z., Walker, J.P., Wang, Y., Huang, C., 2024. Spatial downscaling of SMAP soil moisture estimation using multiscale geographically weighted regression during SMAPVEX16. J. Hydrol. 637, 131348. https://doi.org/10.1016/j.jhydrol.2024.131348

Zhou, J., Liu, S., Li, M., Zhan, W., Xu, Z., Xu, T., 2016. Quantification of the scale effect in downscaling remotely sensed land surface temperature. Remote Sens. 8. https://doi.org/10.3390/rs8120975

Appendix

Table A-1: Calculated spectral indices for the study areas.

Index	Formula
The Enhanced Built-up and Bareness Index (EBBI)	$(SWIR1 - NIR)/(10 * \sqrt{SWIR1 + Thermal})$
The Built-up Area Extraction Index (BAEI)	$(Red + 0.3)/(Green + SWIR1)$
The Built-up Index (BUI)	$\frac{(SWIR1 - NIR)}{(SWIR1 + NIR)} - \frac{(NIR - Red)}{(NIR + Red)}$
The New Built-up Index (NBI)	$(Red - SWIR1)/NIR$
The Normalized Built-up Area Index (NBAI)	$\frac{(\frac{SWIR2 - SWIR1}{Green})}{(\frac{SWIR2 + SWIR1}{Green})}$
The Band Ratio for Built-up Area (BRBA)	$Red/SWIR1$
The Normalized Difference Built-up Index (NDBI)	$(SWIR1 - NIR)/(SWIR1 + NIR)$
The Modified Built-up Area Index (MBAI)	$\frac{[NIR + (1.57 * Green) + (2.4 * SWIR1)]}{(1 + NIR)}$
The Dry Built-up Index (DBI)	$\frac{(Blue - Thermal)}{(Blue + Thermal)} - \frac{(NIR - Red)}{(NIR + Red)}$
The Green Normalized Difference Vegetation Index (GNDVI)	$(NIR - Green)/(NIR + Green)$
The Normalized Difference Vegetation Index (NDVI)	$(NIR - Red)/(NIR + Red)$
The Enhanced Vegetation Index (EVI)	$2.5 * ((NIR - Red)/(NIR + 6 * Red - 7.5 * Blue + 1))$
Modified Normalized Difference Water Index (MNDWI)	$(Green - SWIR1) / (Green + SWIR1)$

Table A-2: Model diagnostics for sectoral nighttime light trajectories across lockdown periods. This table reports sample size (*N*), goodness-of-fit (R^2), and associated *p*-values for piecewise linear regressions fitted to sector-level nighttime lights (NTL) representations in pre-lockdown, lockdown, and post-lockdown periods. Results are reported for transparency of model fitting and temporal segmentation only. Resilience archetypes are derived from the relative configuration of trajectory segments rather than from individual regression coefficients or statistical significance.

Sector	**City**	***N***			**R^2**			***p*-values**		
		Pre	**During**	**Post**	**Pre**	**During**	**Post**	**Pre**	**During**	**Post**
Commercial	Amsterdam	27	13	32	0.57	0.82	0.11	0.00	0.00	0.07
	Buenos Aires	27	18	27	0.93	0.10	0.45	0.00	0.21	0.00
	Beijing	26	35	11	0.96	0.33	0.87	0.00	0.00	0.00

Sector	City	N			R^2			p-values		
		Pre	During	Post	Pre	During	Post	Pre	During	Post
	Berlin	27	17	28	0.24	0.97	0.71	0.01	0.00	0.00
	Brisbane	27	17	28	0.60	0.43	0.13	0.00	0.00	0.06
	Cairo	27	3	42	0.29	0.62	0.02	0.00	0.42	0.42
	Caracas	27	19	26	0.90	0.66	0.95	0.00	0.00	0.00
	Dallas	27	8	37	0.15	0.98	0.86	0.05	0.00	0.00
	Delhi	27	22	23	0.88	0.93	0.99	0.00	0.00	0.00
	Dubai	27	2	43	0.37		0.48	0.00		0.00
	Frankfurt	27	17	28	0.90	0.94	0.57	0.00	0.00	0.00
	Guangzhou	25	35	12	0.69	0.66	1.00	0.00	0.00	0.00
	Istanbul	27	15	30	0.22	0.10	0.00	0.01	0.26	0.74
	Johannesburg	27	21	24	0.95	0.93	0.84	0.00	0.00	0.00
	Los Angeles	27	13	32	0.74	0.00	0.89	0.00	0.98	0.00
	Lima	27	22	23	0.57	0.76	0.05	0.00	0.00	0.32
	London	27	12	33	0.88	0.89	0.07	0.00	0.00	0.13
	Madrid	27	18	27	0.79	0.00	0.57	0.00	0.80	0.00
	Manchester	27	12	33	0.16	0.78	1.00	0.04	0.00	0.00
	Melbourne	27	19	26	0.90	0.76	0.86	0.00	0.00	0.00
	Milan	26	23	23	0.12	0.95	0.83	0.08	0.00	0.00
	Mumbai	27	22	23	0.25	0.72	0.77	0.01	0.00	0.00
	Munich	27	17	28	0.82	0.96	0.61	0.00	0.00	0.00
	Nairobi	27	19	26	0.40	0.35	0.61	0.00	0.01	0.00
	Paris	27	15	30	0.39	0.97	0.01	0.00	0.00	0.67
	Pune	27	22	23	0.99	0.13	0.92	0.00	0.10	0.00
	Rio de Janeiro	29	12	31	0.79	0.96	0.57	0.00	0.00	0.00
	Riyadh	27	3	42	0.75	0.97	0.76	0.00	0.11	0.00
	Rome	26	23	23	0.89	0.92	0.95	0.00	0.00	0.00

Sector	**City**	***N***			**R^2**			***p*-values**		
		Pre	**During**	**Post**	**Pre**	**During**	**Post**	**Pre**	**During**	**Post**
	Santiago	27	18	27	0.78	0.70	0.80	0.00	0.00	0.00
	Shanghai	27	26	19	0.01	0.01	0.44	0.63	0.60	0.00
	Shenzhen	25	35	12	0.83	0.69	0.99	0.00	0.00	0.00
	Sao Paulo	38	5	29	0.28	1.00	0.82	0.00	0.00	0.00
	Sydney	27	19	26	0.50	0.94	0.89	0.00	0.00	0.00
	Vienna	27	21	24	0.39	0.07	0.94	0.00	0.26	0.00
	Mean (Sector-Period)	**27**	**18**	**27**	**0.60**	**0.66**	**0.64**	**0.02**	**0.11**	**0.07**
	Mean (Sector Overall)		**24**			**0.63**			**0.07**	
Industrial	Abu Dhabi	27	2	43	0.75		0.60	0.00		0.00
	Almaty	27	22	23	0.32	0.86	0.92	0.00	0.00	0.00
	Amsterdam	27	13	32	0.64	0.87	0.13	0.00	0.00	0.04
	Athens	27	25	20	0.22	0.89	0.98	0.01	0.00	0.00
	Buenos Aires	27	18	27	0.28	0.34	0.58	0.00	0.01	0.00
	Baku	27	10	35	0.43	0.98	0.08	0.00	0.00	0.09
	Beijing	26	35	11	0.08	0.84	0.98	0.17	0.00	0.00
	Berlin	27	17	28	0.16	0.97	0.00	0.04	0.00	0.78
	Brisbane	27	17	28	0.77	0.25	0.84	0.00	0.04	0.00
	Cairo	27	3	42	0.49	0.85	0.04	0.00	0.26	0.23
	Cape Town	27	21	24	0.10	0.89	0.77	0.12	0.00	0.00
	Caracas	27	19	26	0.25	0.57	0.90	0.01	0.00	0.00
	Chicago	27	3	42	0.57	0.98	0.39	0.00	0.10	0.00
	Dallas	27	8	37	0.08	0.98	0.64	0.16	0.00	0.00
	Delhi	27	22	23	0.94	0.30	0.79	0.00	0.01	0.00
	Dubai	27	2	43	0.53		0.75	0.00		0.00
	Frankfurt	27	17	28	0.95	0.88	0.43	0.00	0.00	0.00

Sector	**City**	***N***			***R^2***			***p*-values**		
		Pre	**During**	**Post**	**Pre**	**During**	**Post**	**Pre**	**During**	**Post**
	Guangzhou	25	35	12	0.03	0.23	1.00	0.40	0.00	0.00
	Hong Kong	25	35	12	0.55	0.43	0.96	0.00	0.00	0.00
	Istanbul	27	15	30	0.23	0.94	0.27	0.01	0.00	0.00
	Jeddah	27	3	42	0.96	0.79	0.02	0.00	0.30	0.40
	Johannesburg	27	21	24	0.81	0.96	0.01	0.00	0.00	0.72
	Los Angeles	27	13	32	0.46	0.44	0.85	0.00	0.01	0.00
	Lahore	27	15	30	0.82	0.18	0.12	0.00	0.11	0.07
	Lima	27	22	23	0.39	0.09	0.76	0.00	0.16	0.00
	London	27	12	33	0.82	0.92	0.04	0.00	0.00	0.24
	Madrid	27	18	27	0.80	0.01	0.45	0.00	0.68	0.00
	Manchester	27	12	33	0.72	0.59	0.66	0.00	0.00	0.00
	Melbourne	27	19	26	0.86	0.63	0.75	0.00	0.00	0.00
	Mexico City	27	23	22	0.32	0.52	0.00	0.00	0.00	0.99
	Milan	26	23	23	0.25	0.98	0.15	0.01	0.00	0.07
	Mumbai	27	22	23	0.21	0.01	0.86	0.02	0.61	0.00
	Munich	27	17	28	0.97	0.93	0.47	0.00	0.00	0.00
	Nairobi	27	19	26	0.20	0.66	0.01	0.02	0.00	0.71
	New York	27	15	30	0.89	0.02	0.33	0.00	0.60	0.00
	Paris	27	15	30	0.02	0.97	0.02	0.53	0.00	0.48
	Pune	27	22	23	0.97	0.36	0.87	0.00	0.00	0.00
	Rio de Janeiro	29	12	31	0.85	0.99	0.15	0.00	0.00	0.03
	Riyadh	27	3	42	0.75	0.89	0.62	0.00	0.21	0.00
	Rome	26	23	23	0.57	0.64	0.02	0.00	0.00	0.57
	Santiago	27	18	27	0.96	0.96	0.86	0.00	0.00	0.00
	Shanghai	27	26	19	0.57	0.35	0.94	0.00	0.00	0.00
	Shenzhen	25	35	12	0.87	0.52	0.99	0.00	0.00	0.00

Sector	**City**	***N***			**R^2**			***p*-values**		
		Pre	**During**	**Post**	**Pre**	**During**	**Post**	**Pre**	**During**	**Post**
	Sao Paulo	38	5	29	0.00	0.96	0.73	0.86	0.00	0.00
	Sydney	27	19	26	0.35	0.89	0.77	0.00	0.00	0.00
	Vienna	27	21	24	0.80	0.81	0.95	0.00	0.00	0.00
	Washington DC	27	14	31	0.00	0.66	0.85	0.81	0.00	0.00
	Wuhan	26	34	12	0.23	0.40	0.95	0.01	0.00	0.00
	Mean (Sector-Period)	**27**	**18**	**27**	**0.52**	**0.67**	**0.55**	**0.07**	**0.07**	**0.11**
	Mean (Sector Overall)		**24**			**0.58**			**0.08**	
Retail	Almaty	27	22	23	0.16	0.59	0.29	0.04	0.00	0.01
	Amsterdam	27	13	32	0.20	0.89	0.18	0.02	0.00	0.02
	Buenos Aires	27	18	27	0.17	0.94	0.45	0.03	0.00	0.00
	Baku	27	10	35	0.01	0.98	0.73	0.61	0.00	0.00
	Brisbane	27	17	28	0.96	0.75	0.49	0.00	0.00	0.00
	Caracas	27	19	26	0.73	0.73	0.97	0.00	0.00	0.00
	Chicago	27	3	42	0.48	0.90	0.29	0.00	0.20	0.00
	Dallas	27	8	37	0.92	0.87	0.12	0.00	0.00	0.04
	Johannesburg	27	21	24	0.90	0.95	0.57	0.00	0.00	0.00
	Los Angeles	27	13	32	0.43	0.86	0.98	0.00	0.00	0.00
	Lima	27	22	23	0.26	0.11	0.51	0.01	0.13	0.00
	Madrid	27	18	27	0.56	0.00	0.68	0.00	0.81	0.00
	Manchester	27	12	33	0.86	0.93	0.82	0.00	0.00	0.00
	Melbourne	27	19	26	0.95	0.59	0.88	0.00	0.00	0.00
	Mexico City	27	23	22	0.33	0.52	0.02	0.00	0.00	0.54
	Milan	26	23	23	0.91	0.02	0.85	0.00	0.49	0.00
	New York	27	15	30	0.91	0.54	0.79	0.00	0.00	0.00
	Paris	27	15	30	0.46	0.83	0.10	0.00	0.00	0.09

Sector	City	*N*			R^2			*p*-values		
		Pre	**During**	**Post**	**Pre**	**During**	**Post**	**Pre**	**During**	**Post**
	Riyadh	27	3	42	0.88	0.86	0.68	0.00	0.24	0.00
	Rome	26	23	23	0.87	0.73	0.66	0.00	0.00	0.00
	Sao Paulo	38	5	29	0.88	0.96	0.68	0.00	0.00	0.00
	Sydney	27	19	26	0.12	0.88	0.72	0.08	0.00	0.00
	Wuhan	26	34	12	0.12	0.62	0.99	0.08	0.00	0.00
	Mean (Sector-Period)	**27**	**16**	**28**	**0.57**	**0.70**	**0.59**	**0.04**	**0.08**	**0.03**
	Mean (Sector Overall)		**24**			**0.62**			**0.05**	

Table A-3: City–sector impacts underlying resilience archetype classification. Gross Impact (Lockdown minus Pre-lockdown), Recovery (Post-lockdown minus Lockdown), and Net Impact (Post-lockdown minus Pre-lockdown) in nighttime light (NTL) brightness for each city–sector combination used in the archetype classification. Values are reported for transparency and traceability of the trajectory summaries. Essentiality is categorized as Essential, Non-essential, or Mixed. Summary rows (sector and archetype means) are provided for reference; empty cells indicate that no city–sector combinations were observed for that pairing.

Archetype	Sectoral	Continent	City	Essentiality	Gross Impact	Recovery	Net Impact
Chronic decline	Commercial	Africa	Johannesburg	Mix	-0.36	-0.43	-0.80
		Asia	Istanbul	Non-Essential	-2.68	-0.26	-2.94
		Asia	Shanghai	Non-Essential	-13.10	-2.67	-15.77
		Europe	Amsterdam	Non-Essential	-0.16	-48.99	-49.15
		Europe	Berlin	Non-Essential	-6.14	-7.30	-13.43
		Europe	Frankfurt	Non-Essential	-11.11	-10.72	-21.83
		Europe	London	Non-Essential	-0.01	-2.98	-2.99

Archetype	Sectoral	Continent	City	Essentiality	Gross Impact	Recovery	Net Impact
		Europe	Manchester	Non-Essential	-4.58	-16.12	-20.71
		Europe	Milan	Non-Essential	-0.39	-0.59	-0.97
		Europe	Munich	Non-Essential	-11.89	-9.29	-21.18
		Europe	Paris	Non-Essential	-0.85	-0.23	-1.08
		Europe	Rome	Non-Essential	-3.36	-1.00	-4.36
		Europe	Vienna	Non-Essential	-1.09	-8.32	-9.41
			Sectoral Mean		**-4.29**	**-8.38**	**-12.66**
	Industrial	Africa	Cape Town	Non-Essential	-2.47	-10.28	-12.74
		Africa	Johannesburg	Non-Essential	-0.35	-0.48	-0.83
		Asia	Abu Dhabi	Mix	-1.82	-1.82	-3.64
		Asia	Istanbul	Non-Essential	-2.13	-0.50	-2.63
		Asia	Jeddah	Non-Essential	-6.78	-5.66	-12.44
		Asia	Shanghai	Non-Essential	-5.40	-2.15	-7.54
		Europe	Amsterdam	Non-Essential	-7.90	-82.29	-90.20
		Europe	Berlin	Non-Essential	-10.72	-5.49	-16.21
		Europe	Frankfurt	Non-Essential	-16.47	-0.97	-17.44
		Europe	London	Non-Essential	-0.35	-4.43	-4.78

Archetype	Sectoral	Continent	City	Essentiality	Gross Impact	Recovery	Net Impact
		Europe	Manchester	Non-Essential	-0.48	-11.61	-12.10
		Europe	Milan	Non-Essential	-0.55	-0.74	-1.29
		Europe	Munich	Non-Essential	-9.30	-8.30	-17.60
		Europe	Paris	Mix	-0.53	-0.49	-1.01
		Europe	Vienna	Non-Essential	-3.68	-6.83	-10.51
			Sectoral Mean		**-4.60**	**-9.47**	**-14.06**
	Retail	Africa	Johannesburg	Non-Essential	-1.28	-0.35	-1.62
		Europe	Amsterdam	Non-Essential	-8.55	-61.24	-69.79
		Europe	Manchester	Non-Essential	-3.49	-4.25	-7.74
		Europe	Milan	Non-Essential	-0.10	-0.62	-0.72
		Europe	Paris	Non-Essential	-1.15	0.00	-1.16
		Oceania	Brisbane		-2.97	-2.91	-5.88
			Sectoral Mean		**-2.92**	**-11.56**	**-14.49**
			Archetype Mean		**-4.18**	**-9.42**	**-13.60**
Partial recovery	Commercial	Asia	Guangzhou	Non-Essential	-4.19	2.77	-1.42
		Oceania	Melbourne	Mix	-0.56	0.48	-0.08
		Oceania	Sydney	Mix	-1.96	0.19	-1.78
			Sectoral Mean		**-2.24**	**1.15**	**-1.09**

Archetype	Sectoral	Continent	City	Essentiality	Gross Impact	Recovery	Net Impact
	Industrial	Africa	Cairo	Non-Essential	-1.37	0.70	-0.67
		Africa	Nairobi	Non-Essential	-1.73	1.20	-0.53
		Asia	Almaty	Mix	-4.54	0.16	-4.37
		Asia	Guangzhou	Non-Essential	-7.78	2.32	-5.45
		Asia	Lahore	Mix	-0.92	0.13	-0.79
		North America	Chicago	Mix	-6.58	5.03	-1.55
		North America	Los Angeles	Mix	-1.05	0.53	-0.51
		North America	Washington DC	Non-Essential	-3.18	0.09	-3.09
		Oceania	Sydney	Non-Essential	-1.36	0.65	-0.71
			Sectoral Mean		**-3.17**	**1.20**	**-1.96**
	Retail	Europe	Rome		-4.95	2.27	-2.68
		Oceania	Melbourne	Mix	-0.93	0.17	-0.75
			Sectoral Mean		**-2.94**	**1.22**	**-1.72**
			Archetype Mean		**-2.94**	**1.19**	**-1.74**
Full recovery	Commercial	Africa	Cairo	Mix	-0.70	1.49	0.79
		Africa	Nairobi	Mix	-1.93	9.05	7.12
		Asia	Delhi	Mix	-0.58	0.76	0.19
		Asia	Dubai	Non-Essential	-6.94	21.67	14.74
		Asia	Mumbai	Non-Essential	-0.32	1.97	1.65
		Asia	Riyadh		-2.33	6.24	3.91

Appendix

Archetype	Sectoral	Continent	City	Essentiality	Gross Impact	Recovery	Net Impact
		Europe	Madrid	Mix	-0.03	3.26	3.23
		North America	Los Angeles	Mix	-0.48	1.36	0.87
		South America	Rio De Janeiro	Mix	-0.34	3.67	3.33
			Sectoral Mean		**-1.52**	**5.50**	**3.98**
	Industrial	Asia	Delhi	Mix	-0.28	0.64	0.36
		Asia	Dubai	Non-Essential	-2.39	7.13	4.74
		Asia	Hong Kong	Mix	-7.39	8.62	1.23
		Asia	Riyadh	Non-Essential	-2.33	3.37	1.04
		Central America	Mexico	Mix	-0.94	7.05	6.11
		Europe	Athens	Mix	-1.62	2.21	0.60
		Europe	Madrid	Mix	-0.37	3.63	3.26
		Europe	Rome	Mix	-1.18	3.79	2.61
		South America	Rio De Janeiro	Mix	-2.06	6.30	4.24
		Oceania	Melbourne	Mix	-0.30	0.65	0.35
			Sectoral Mean		**-1.89**	**4.34**	**2.45**
	Retail	Asia	Riyadh		-15.13	30.56	15.43
		Central America	Mexico	Non-Essential	-1.36	7.86	6.50
		Europe	Madrid	Mix	-0.45	3.85	3.40
		North America	Chicago	Mix	-2.76	10.40	7.64
		South America	Sao Paulo		-0.27	1.76	1.50

Archetype	Sectoral	Continent	City	Essentiality	Gross Impact	Recovery	Net Impact
			Sectoral Mean		**-3.99**	**10.89**	**6.89**
			Archetype Mean		**-2.19**	**6.14**	**3.95**
Resilient	Commercial	Asia	Beijing		0.64	-0.17	0.48
		Asia	Pune	Non-Essential	0.14	0.76	0.89
		Asia	Shenzhen	Non-Essential	10.61	3.15	13.76
		North America	Dallas	Mix	6.59	6.46	13.04
		South America	Buenos Aires	Mix	0.24	0.58	0.82
		South America	Caracas	Mix	17.31	24.99	42.30
		South America	Lima	Non-Essential	12.38	8.81	21.19
		South America	Santiago	Mix	0.77	11.77	12.54
		South America	Sao Paulo		0.61	1.47	2.08
		Oceania	Brisbane	Mix	3.89	1.94	5.82
			Sectoral Mean		**5.32**	**5.98**	**11.29**
	Industrial	Asia	Baku	Mix	2.97	10.58	13.55
		Asia	Beijing	Essential	0.77	0.29	1.06
		Asia	Mumbai	Mix	10.47	-9.87	0.61
		Asia	Pune	Mix	0.17	0.52	0.70
		Asia	Shenzhen	Non-Essential	9.85	3.49	13.34
		Asia	Wuhan	Mix	0.86	-0.76	0.09

Archetype	Sectoral	Continent	City	Essentiality	Gross Impact	Recovery	Net Impact
		North America	Dallas	Mix	6.15	8.79	14.95
		North America	New York	Non-Essential	0.74	0.22	0.96
		South America	Buenos Aires	Mix	0.29	0.20	0.49
		South America	Caracas	Essential	3.22	10.97	14.19
		South America	Lima	Mix	6.73	-0.38	6.35
		South America	Santiago	Essential	8.66	8.73	17.38
		South America	Sao Paulo	Mix	0.20	1.74	1.94
		Oceania	Brisbane	Mix	0.51	1.50	2.00
			Sectoral Mean		**3.68**	**2.57**	**6.26**
	Retail	Asia	Almaty	Essential	0.59	6.00	6.59
		Asia	Baku	Essential	2.09	5.49	7.58
		Asia	Wuhan		1.64	-1.15	0.49
		North America	Dallas	Mix	9.44	11.18	20.62
		North America	Los Angeles	Mix	0.34	1.74	2.09
		North America	New York	Mix	0.90	-0.60	0.30
		South America	Buenos Aires	Mix	0.20	0.59	0.79
		South America	Caracas	Mix	16.32	30.07	46.39
		South America	Lima	Essential	12.71	2.86	15.57

Archetype	Sectoral	Continent	City	Essentiality	Gross Impact	Recovery	Net Impact
			Sectoral Mean		**4.91**	**6.24**	**11.16**
			Archetype Mean		**4.51**	**4.60**	**9.12**

Figures A1–A4 illustrate representative nighttime light trajectories for city–sector combinations assigned to each resilience archetype. Archetypes are defined by relative differences in segment midpoints derived from fitted linear models across the pre-lockdown, lockdown, and post-lockdown periods, rather than by the visual “shape” of individual time-series (Chapter 5 Methods, Resilience archetype classification). As a result, individual trajectories may display heterogeneous temporal patterns while still satisfying the formal criteria for archetype assignment. These figures therefore emphasize within-archetype variability rather than implying uniform recovery dynamics across cities.

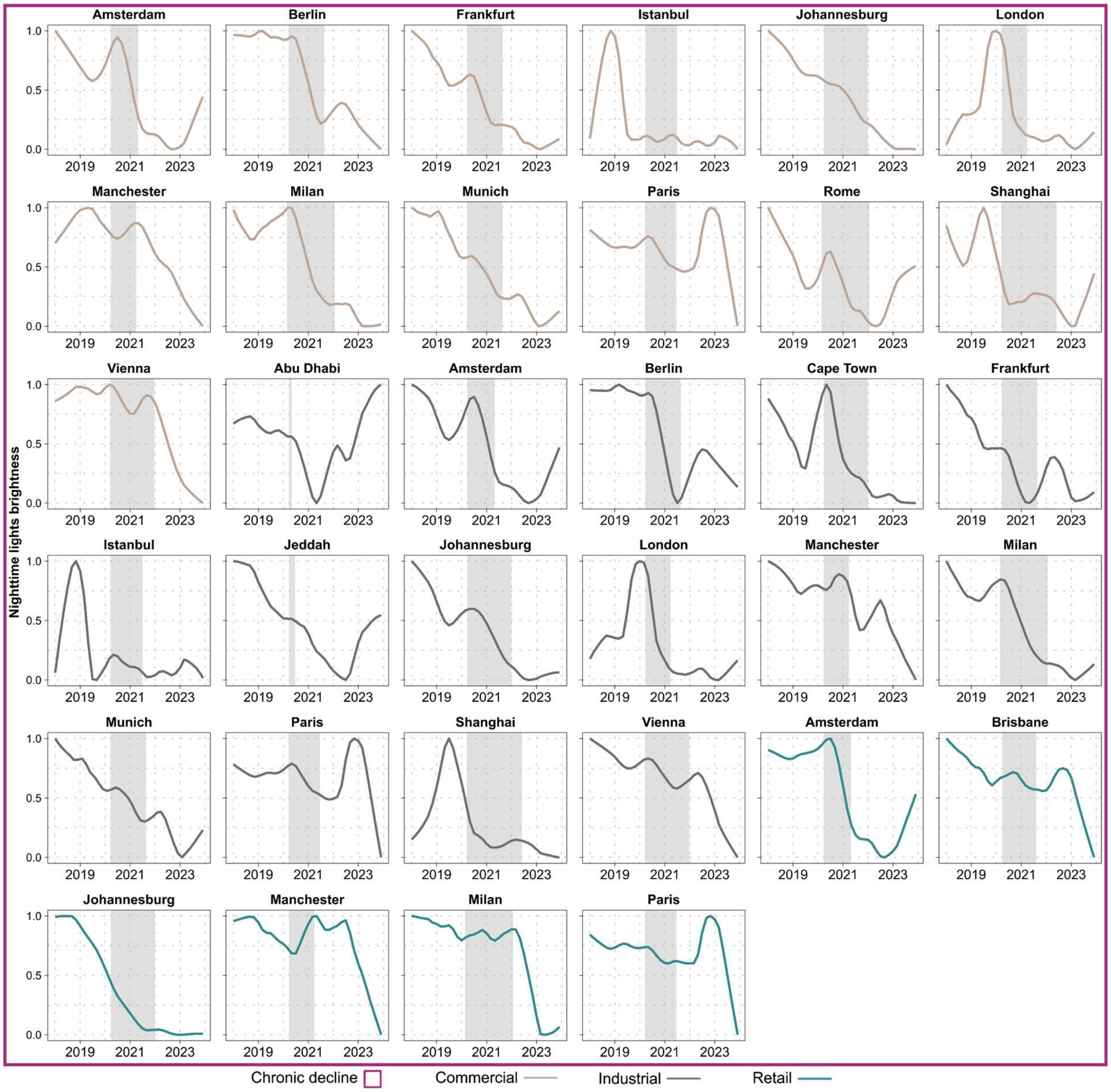

Figure A-1: Nighttime light trajectories for cities classified under the chronic decline archetype. Scaled nighttime light (NTL) intensity (0–1) from 2018 to 2023 is shown for city-sector combinations classified as Chronic decline, plotted separately for commercial (brown), industrial (grey), and retail (blue) sectors. Grey shaded areas indicate city-specific COVID-19 lockdown periods. Cities in this archetype experienced sustained declines in nighttime brightness that began during the lockdown and persisted throughout the study period, with minimal evidence of recovery. The purple border delineates all cities within this archetype. Trajectories are normalized within each city–sector combination to facilitate comparison of temporal patterns rather than absolute brightness levels.

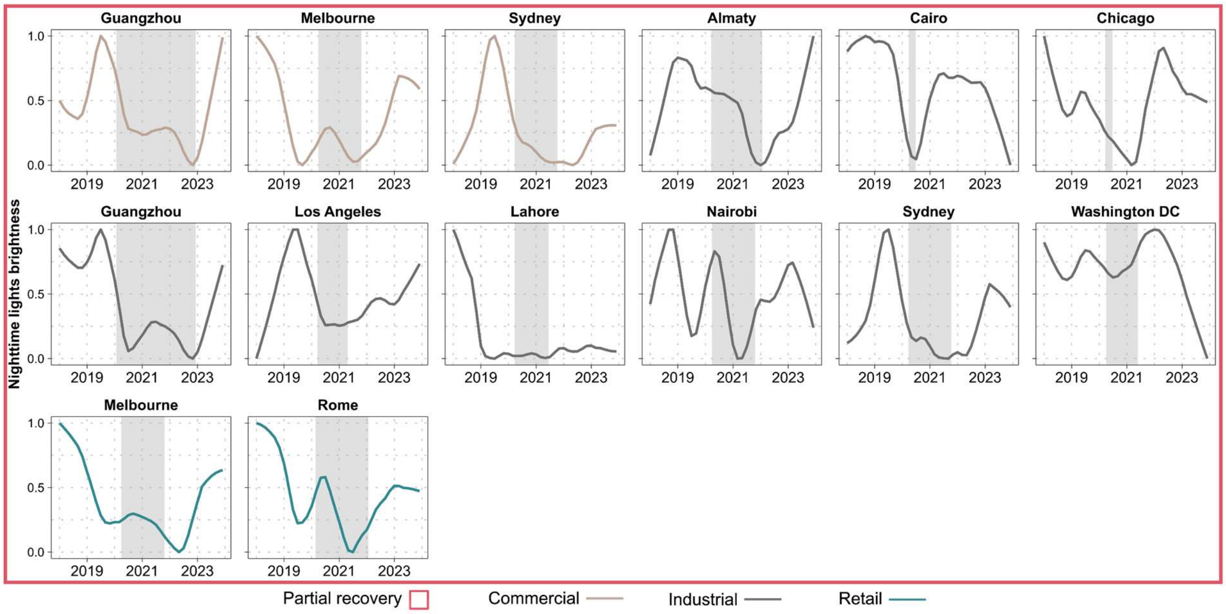

Figure A-2: Nighttime light trajectories for cities classified under the partial recovery archetype. Scaled nighttime light (NTL) intensity (0–1) from 2018 to 2023 is shown for city-sector combinations classified as Partial recovery, plotted separately for commercial (brown), industrial (grey), and retail (blue) sectors. Grey shaded areas indicate city-specific COVID-19 lockdown periods. Cities in this archetype experienced declines in nighttime economic activity during lockdown periods, followed by partial recovery that remained below pre-pandemic baselines. The red border delineates all cities within this archetype. Trajectories are normalized within each city–sector combination to facilitate comparison of temporal patterns rather than absolute brightness levels.

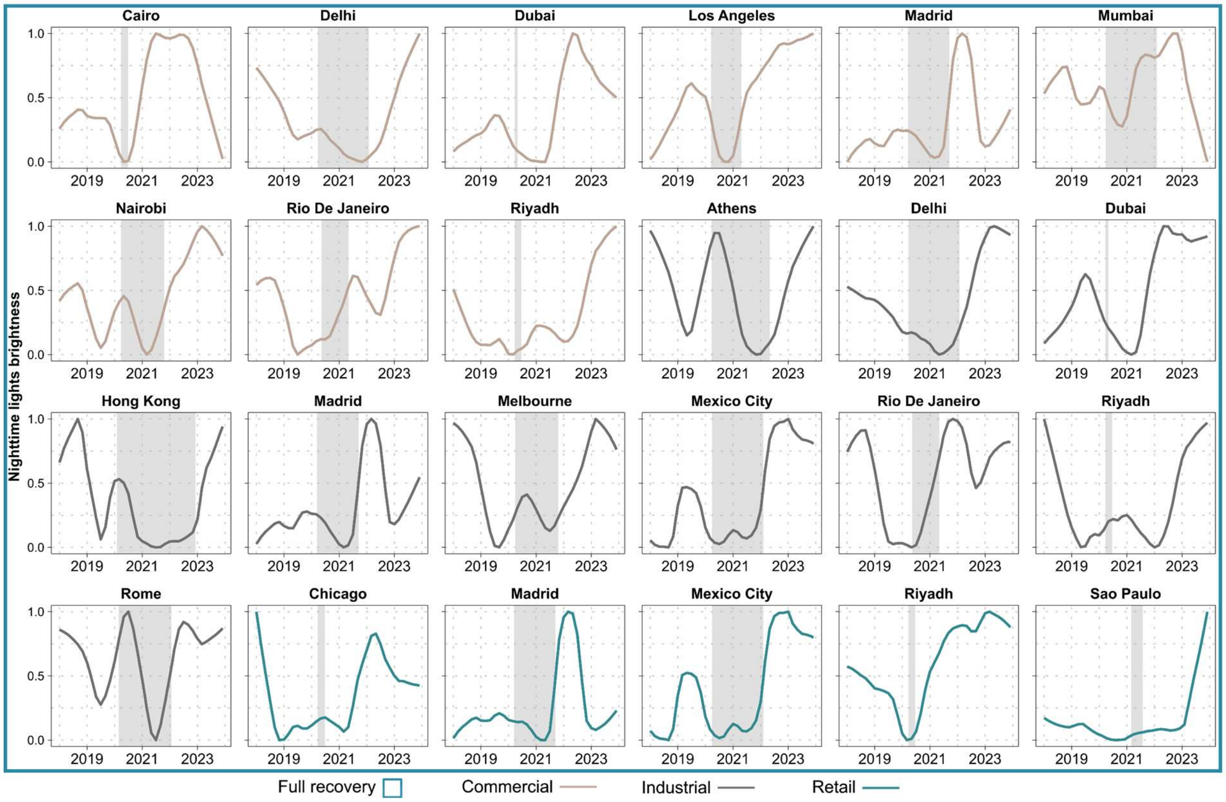

Figure A-3: Nighttime light trajectories for cities classified under the full recovery archetype. Scaled nighttime light (NTL) intensity (0–1) from 2018 to 2023 is shown for city-sector combinations classified as Full recovery, plotted separately for commercial (brown), industrial (grey), and retail (blue) sectors. Grey shaded areas indicate city-specific COVID-19 lockdown periods. Cities in this archetype experienced declines in nighttime economic activity during lockdown periods, followed by full recovery to pre-pandemic baselines. The cyan border delineates all cities within this archetype. Trajectories are normalized within each city–sector combination to facilitate comparison of temporal patterns rather than absolute brightness levels.

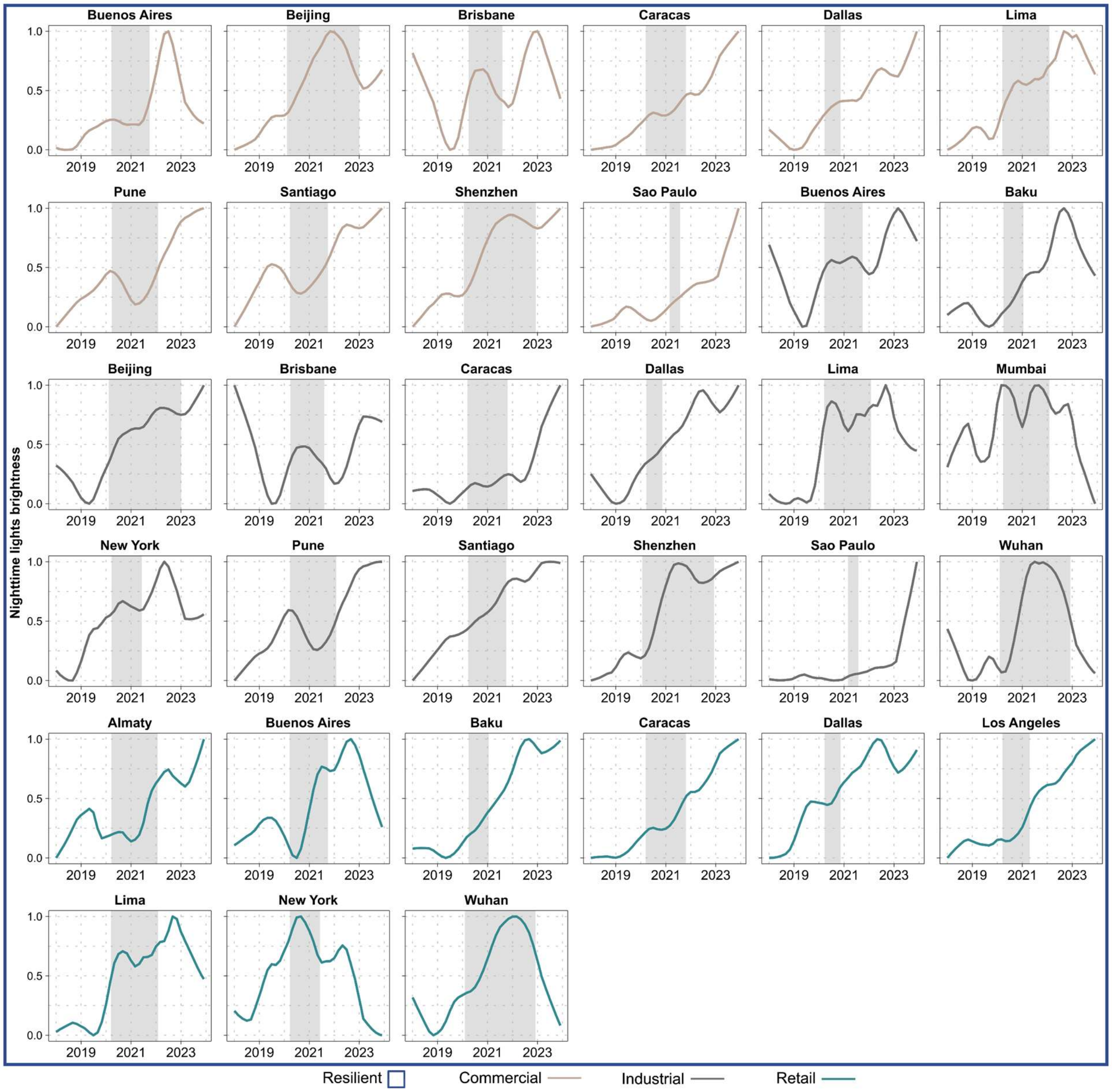

Figure A-4: Nighttime light trajectories for cities classified under the resilient archetype. Scaled nighttime light (NTL) intensity (0–1) from 2018 to 2023 is shown for city-sector combinations classified as Resilient, plotted separately for commercial (brown), industrial (grey), and retail (blue) sectors. Grey shaded areas indicate city-specific COVID-19 lockdown periods. Cities in this archetype experienced maintained or increased their nighttime brightness throughout the study period. The blue border delineates all cities within this archetype. Trajectories are normalized within each city–sector combination to facilitate comparison of temporal patterns rather than absolute brightness levels.

Random forest area-to-point Kriging (RFATPK)

Random Forest area-to-point Kriging (RFATPK) was used to downscale monthly nighttime light (NTL) data from coarse to fine spatial resolution (Figure A-5). The method combines nonlinear regression with geostatistical residual downscaling to account for both the point spread function (PSF) (i.e., the blooming effect in NTL imagery) and spatial non-stationarity.

Predictor variables were first convolved with a Gaussian filter to account for the PSF and resampled using the mean to match the original coarse resolution NTL data. A Random Forest (RF) model was trained at this scale, to capture nonlinear relationships between NTL brightness and auxiliary covariates, thereby estimating the spatial trend component. Under the assumption of scale invariance, the trained RF model was then applied to the fine resolution to predict the trend component in NTL.

Model residuals computed at the coarse resolution were subsequently downscaled using area-to-point kriging (ATPK) and added to the RF-based trend prediction to obtain the fine-resolution NTL estimates (Tziokas et al., 2024). This formulation decomposes NTL into a trend component and a regression residual component, allowing RFATPK to jointly capture nonlinear covariate effects and spatial autocorrelation while satisfying the second-order stationarity assumption required for Kriging.

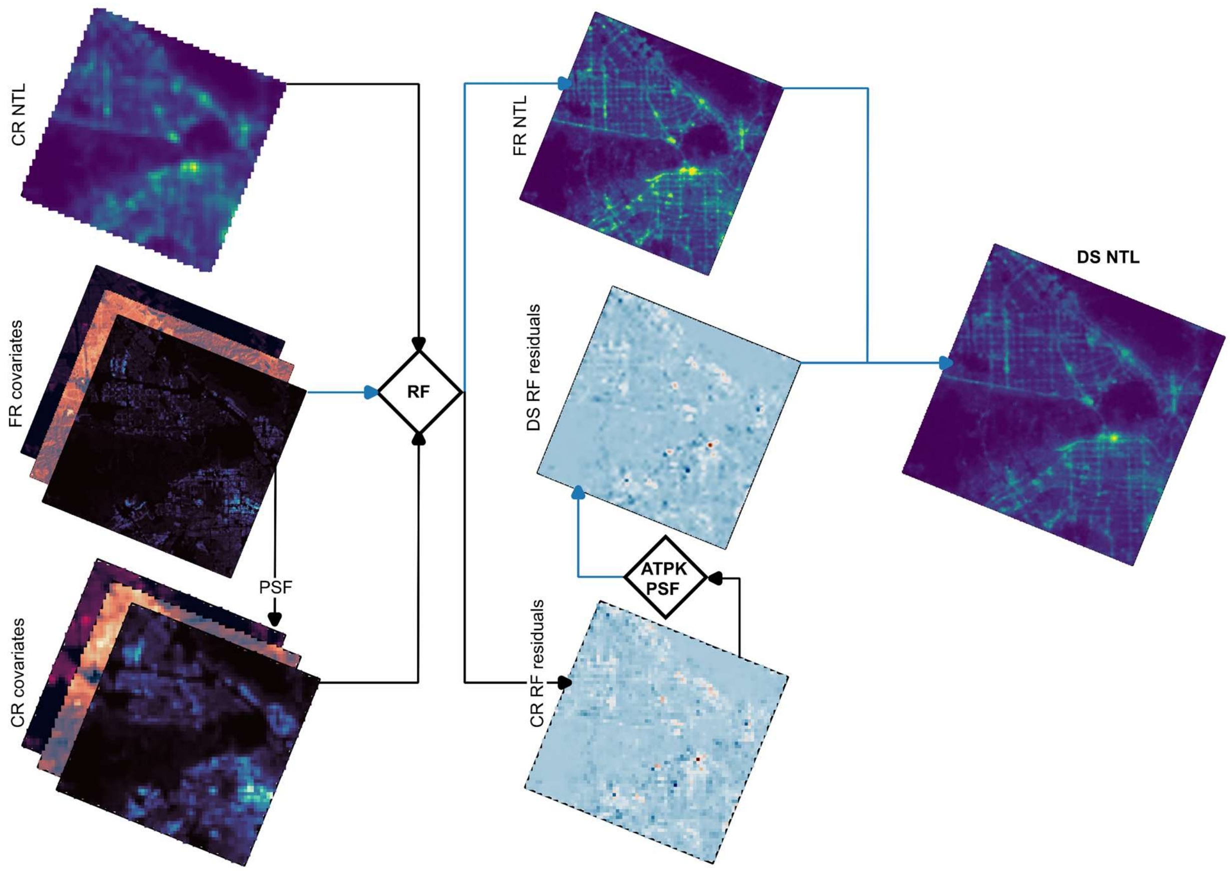

Figure A-5: Conceptual workflow of Random Forest area-to-point Kriging (RFATPK) for nighttime light downscaling. Schematic overview of the RFATPK approach used to predict fine-resolution nighttime light (NTL) intensity from coarse-resolution NTL and auxiliary covariates. This workflow was applied for every monthly NTL image. Black and blue lines indicate data processed at coarse and fine spatial resolutions, respectively. Acronyms: NTL, nighttime lights; CR, coarse resolution; FR, fine resolution; PSF, point spread function; RF, Random Forest; ATPK, area-to-point kriging; DS, downscaled.

Spatial trend prediction using RF

The spatial trend component of nighttime light (NTL) brightness was estimated using a Random Forest (RF) regression model. RF is an ensemble learning approach that captures nonlinear relationships between dependent and independent variables through aggregation of decision trees (Breiman, 2001), and has been applied in NTL downscaling due to its robustness to multicollinearity, missing data, and spatial heterogeneity in predictor relevance (Tziokas et al., 2024).

RF was selected for its strong generalization performance across heterogeneous urban environments, which reduces the risk of overfitting when modeling complex and spatially variable brightness patterns. Consistent with prior evidence that NTL intensity is most associated with socioeconomic activities and the built environment (Xu et al., 2024), these covariates were excluded in the regression. The incorporation of fine-resolution land cover information further mitigated overglow effects by increasing discrimination between built-up and non-built-up areas, as well as between illuminated and non-illuminated surfaces.

The RF regression approach was used to increase the spatial resolution of NTL from its native ~ 500 m resolution to 130 m. Following our previous research (Tziokas et al., 2024), predictor variables were first smoothed and aggregated to the coarse NTL resolution to account for spatial spillover effects, after which the trained RF model was applied to generate fine-resolution estimates of the NTL spatial trend. The RF method was implemented using the R (R Core Team, 2025) package, *ranger* (Wright and Ziegler, 2017).

Downscaling the RF residuals using ATPK

In the second stage of the RFATPK framework, residuals obtained from the coarse resolution RF regression were downscaled to fine spatial resolution using area-to-point kriging (ATPK). Regression-based approaches alone are insufficient for downscaling because they do not fully exploit the spatial and spectral information contained in the observed coarse-resolution data. ATPK is therefore employed to complement the RF regression, explicitly preserving the spatial structure and spectral consistency of the original nighttime light observations.

ATPK is a geostatistical downscaling method designed to estimate values at a spatial resolution finer than the support of the original observations (i.e., pixel) (Zhang et al., 2021). Unlike conventional point-based Kriging, which treats each observation as a centroid value and neglects its spatial support, ATPK accounts explicitly for the size of the support, spatial autocorrelation, and the sensor's point spread function through spatial covariance modeling. This allows residual variability unresolved by the regression model to be redistributed in a spatially coherent manner. A key property of ATPK is its coherence constraint(Kyriakidis, 2004; Kyriakidis and Yoo, 2005), which guarantees that the aggregation of fine-resolution predictions reproduces exactly the original coarse-resolution observations. This ensures that the spectral characteristics of the nighttime light data are preserved during downscaling, preventing artificial inflation or attenuation of brightness values. ATPK was applied to the RF residuals using the R(R Core Team, 2025) package *atakrig* (Hu and Huang, 2020), and the resulting fine-resolution residuals were added back to the RF-predicted spatial trend to obtain the final downscaled NTL estimates.

Table A-4: Dataset/Covariates used for the downscaling process. LST (Land Surface Temperature), NDCCI (Normalized Difference Concrete Condition Index), BLFEI (Built-up Land Features Extraction Index), WSF (World Settlement Footprint), GAIA (Global Artificial Impervious Area), GISA (Global Impervious Surface Area), GEE (Google Earth Engine), Pop (Population Count), Pop dens (Population Density), LC (Land Cover), CLMS (Copernicus Land Monitoring Service), GHS (Global Human Settlement) and GDP (Gross Domestic Product).

Name	**Format**	**Temporal coverage**
NTL (Marty and Stefanini Vicente, 2025)	Raster	2018 – 2023 (monthly)
LST (Gorelick et al., 2017)	Raster	2018 – 2023 (monthly)
BLFEI (Gorelick et al., 2017)	Raster	2018 – 2023 (monthly)

NDCCI (Gorelick et al., 2017)	Raster	2018 – 2023 (monthly)
WSF (“EOC Download - WSF2019,” n.d.)	Raster	2019 (yearly)
GAIA (Gong et al., 2020)	Raster	2018 – 2023 (yearly)
GISA (Huang et al., 2022)	Raster	2019 (yearly)
CLMS (“Imperviousness Density 2018 (raster 10 m and 100 m), Europe, 3-yearly — Copernicus Land Monitoring Service,” n.d.)	Raster	2018 (yearly)
GHS (Pesaresi and Politis, 2022)	Raster	2018, 2020, 2023 (yearly)
GDP (Paprotny and Mengel, 2023)	Raster	2018 – 2020 (yearly)
Pop (Weber et al., 2022)	Raster	2018 – 2021 (yearly)
Pop dens (Gorelick et al., 2017)	Raster	2018 or 2019 or 2020 or 2021 (yearly)
LC (Gorelick et al., 2017)	Raster	2018 – 2023 (yearly)
Road (“OpenStreetMap,” n.d.)	Vector	2018 – 2023 (yearly)

Table A-5: Spectral indices derived from Landsat 8 imagery. Definitions of spectral indices used as covariates in the nighttime light downscaling framework. BLFEI and NDCCI denote the Built-up Land Features Extraction Index and the Normalized Difference Concrete Condition Index, respectively. Band names follow standard Landsat 8 Operational Land Imager (OLI) conventions.

Spectral index	**Formula**
BLFEI (Bouhennache et al., 2019)	$(\frac{\text{Green} + \text{Red} + \text{SWIR2}}{3} - \text{SWIR1})\Big/(\frac{\text{Green} + \text{Red} + \text{SWIR2})}{3} + \text{SWIR1})$
NDCCI (Samsudin et al., 2016)	$(\text{NIR} - \text{Green})/(\text{NIR} + \text{Green})$